

HIGH FIELD PHYSICS AND QED EXPERIMENTS AT ELI-NP

I.C.E. TURCU^{1,2,*}, F. NEGOITA¹, D.A. JAROSZYNSKI³, P. MCKENNA³,
S. BALASCUTA¹, D. URSESCU¹, I. DANCUS¹, M.O. CERNAIANU¹, M.V. TATARU¹,
P. GHENUCHE¹, D. STUTMAN^{1,4}, A. BOIANU¹, M. RISCA¹, M. TOMA¹, C. PETCU¹,
G. ACBAS¹, S.R. YOFFE³, A. NOBLE³, B. ERSFELD³, E. BRUNETTI³, R. CAPDESSUS³,
C. MURPHY⁵, C.P. RIDGERS⁵, D. NEELY², S.P.D. MANGLES⁶, R. J. GRAY³, A.G.R. THOMAS⁷,
J.G. KIRK⁸, A. ILBERTON⁹, M. MARKLUND⁹, D.F. GORDON¹⁰, B. HAFIZI¹⁰,
D. KAGANOVICH¹⁰, J.P. PALASTRO¹⁰, E. D'HUMIERES¹¹, M. ZEPF^{12,13,14}, G. SARRI¹⁴,
H. GIES^{12,13}, F. KARBSTEIN¹², J. SCHREIBER^{15,16}, G.G. PAULUS^{12,13}, B. DROMEY¹⁴,
C. HARVEY^{9,14}, A. DI PIAZZA⁸, C.H. KEITEL⁸, M.C. KALUZA^{12,13}, S. GALES¹, N.V. ZAMFIR¹

¹ELI-NP, "Horia Hulubei" National Institute for Physics and Nuclear Engineering, 30 Reactorului Street, RO-077125, Bucharest-Magurele, Romania

²Central Laser Facility, STFC Rutherford Appleton Laboratory, Oxfordshire OX11 0QX, United Kingdom

³University of Strathclyde, SUPA, Department of Physics, Glasgow G4 0NG, United Kingdom

⁴Department of Physics and Astronomy, Johns Hopkins University, Baltimore, Maryland 21218, USA

⁵Department of Physics, University of York, York YO10 5D, United Kingdom

⁶Blackett Laboratory, Imperial College, London, SW7 2BZ, United Kingdom

⁷Center for Ultrafast Optical Science, University of Michigan, Ann Arbor, Michigan 48109-2099, USA

⁸Max-Planck-Institut für Kernphysik, Saupfercheckweg 1, 69117 Heidelberg, Germany

⁹Department of Physics, Chalmers University of Technology, SE-41296 Gothenburg, Sweden

¹⁰Naval Research Laboratory, Washington DC 20375-5346, USA

¹¹CELI, University of Bordeaux - CNRS - CEA, 33405 Talence, France

¹²Helmholtz-Institut Jena, Fröbelstieg 3, 07743 Jena, Germany

¹³Friedrich-Schiller-Universität Jena, Max-Wien-Platz 1, 07743 Jena, Germany

¹⁴School of Mathematics and Physics, Queen's University Belfast, BT7 1NN, United Kingdom

¹⁵Fakultät für Physik, Ludwig-Maximilians-Universität München, D-85748 Garching, Germany

¹⁶Max-Planck-Institut für Quantenoptik, Hans-Kopfermann-Str. 1, D-85748 Garching, Germany

* Corresponding author *Email*: edmond.turcu@eli-np.ro

Abstract. ELI-NP facility will enable for the first time the use of two 10 PW laser beams for quantum electrodynamics (QED) experiments. The first beam will accelerate electrons to relativistic energies. The second beam will subject relativistic electrons to the strong electromagnetic field generating QED processes: intense gamma ray radiation and electron-positron pair formation. The laser beams will be focused to intensities above 10^{21} Wcm⁻² and reaching 10^{22} - 10^{23} Wcm⁻² for the first time. We propose to use this capability to investigate new physical phenomena at the interfaces of plasma, nuclear and particle physics at ELI-NP. This High Power Laser System - Technical Design Report (HPLS-TDR2) presents the experimental area E6 at ELI-NP for investigating high field physics and quantum electrodynamics and the production of electron-positron-pairs and of energetic gamma-rays. The scientific community submitted 12 commissioning runs for E6 interaction chamber with two 10 PW laser beams and one proposal for the CETAL interaction chamber with 1 PW laser. The proposals are representative of the international high field physics community being written by 48 authors from 14 European and US organizations. The proposals are classified according to the science area investigated into: Radiation Reaction Physics: Classical and Quantum; Compton and Thomson Scattering Physics: Linear and Non-Linear Regimes; QED in Vacuum; Atoms in Extreme Fields. Two pump-probe colliding 10 PW laser beams are proposed for the E6 interaction chamber. The focused pump laser beam accelerates the electrons to relativistic energies. The accelerated electron bunches interact with the very high electro-magnetic field of the focused probe laser beam. We propose two main types of experiments with: (a) gas targets in which the pump laser-beam is focused by a long focal length mirror and drives a wakefield in which the electron bunch is accelerated to multi-GeV energies and then exposed to the EM field of the probe laser which is tightly focused; (b) solid targets in which both the pump and probe laser beams are focused on the solid target, one accelerating the electrons in the solid and the other, delayed, providing the high electric field to which the relativistic electrons are subjected. We propose four main focusing configurations for the pump and probe laser beams, two for each type of target: counter-propagating 10 PW focused laser beams and the two 10 PW laser beams focused in the same direction. For solid targets we propose an additional configuration with plasma-mirror on the pump laser beam: the plasma mirror placed between the focusing mirror and target. It is proposed that the 10 PW laser beams will have polarization control and focus control by means of adaptive optics. Initially only one 10 PW may have polarization control and adaptive optics. In order to accommodate the two laser beams and diagnostics the proposed interaction chamber is quasi-octagonal with a diameter of 4.5 m. A large electron-spectrometer is proposed for multi-GeV electrons. Other diagnostics are requested for: gamma-rays, electrons and positrons, protons and ions, plasma characterization, transmitted and reflected laser beam. Targets will be provided by the ELI-NP Target Laboratory or purchased. The E6 experiments and diagnostics will benefit from the ELI-NP Electronics Laboratory, the Workshop and the Optics Laboratory. In order to ensure radiation-protection, a large beam-dump is planned for both multi-GeV electrons and multi-100 MeV protons.

Key words: Extreme Light, Ultra-intense Laser Pulses, High Field Physics, Quantum Electrodynamics.

1. INTRODUCTION

The Extreme Light Infrastructure-Nuclear Physics (ELI-NP) facility will enable focused laser intensities above 10^{21} Wcm⁻² and reaching 10^{22} - 10^{23} Wcm⁻² to be achieved for the first time (Fig. 1) and to scale up the very large electric and magnetic fields provided by focused laser beams. This will enable the investigation of new physical phenomena at the interfaces of plasma, nuclear and particle physics. Exciting prospects are the study of radiation reaction, high-field quantum electrodynamics (QED) and the resulting production of electron-positron-pairs and of energetic gamma-rays. Although the Schwinger field $E_S = 1.3 \times 10^{18}$ Vm⁻¹ required for spontaneous electron-positron pair creation out of the vacuum requires a laser intensity of 2.3×10^{29} Wcm⁻², which is still far beyond reach, several high-field QED processes will be accessible at ELI-NP [1-18]. The types of experiments described here aims to investigate this in the context of dense plasma interactions (solid targets) and beam-beam interactions (gas targets).

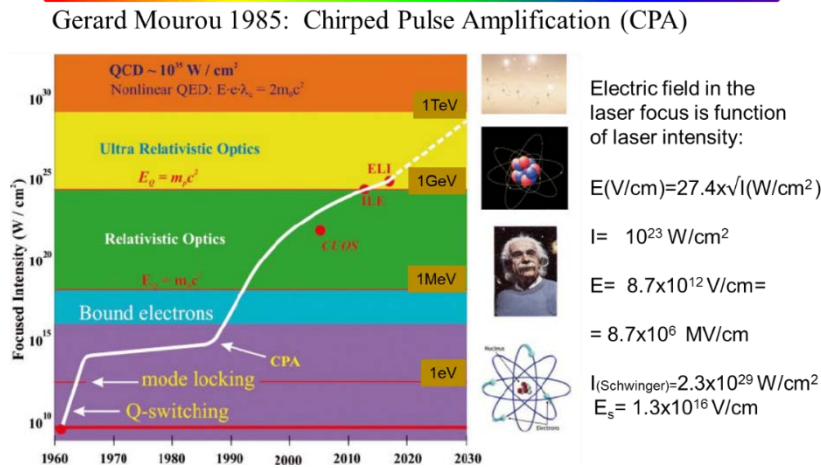


Fig. 1 – The large increase of laser focused intensity will access new science where relativistic electrons interact with the very strong electromagnetic field in the laser focus. ELI-NP will provide laser intensities above 10^{22} Wcm⁻² in two synchronized laser beams for pump-probe experiments. Figure presented with permission from Gerard Mourou.

The two main QED processes predicted to be important in high laser fields are: (a) nonlinear Thomson scattering in which a significant fraction (up to 40%) of the energy of electrons accelerated by the laser is damped in the laser field via the emission of synchrotron γ -ray photons (γ_R):



where γ_L is a laser photon, and (b) pair production by the multiphoton Breit-Wheeler process:

$$\gamma_R + m\gamma_L \rightarrow e^- + e^+ \quad (2)$$

The reaction rates for these processes become significant when the parameter:

$$\eta = \frac{\gamma}{E_s} |\mathbf{E}_\perp + \beta \times c\mathbf{B}| \rightarrow 1 \quad (3)$$

where γ is the electron Lorentz factor and \mathbf{E}_\perp is the perpendicular component of the laser electric field to the electron momentum [1–3]. Using high power lasers, $\eta \rightarrow 1$ can be achieved by increasing the electron Lorentz factor γ either by:

(1) interacting a pump-laser pulse wakefield-accelerated electron bunch with a high intensity counter-propagating Probe-laser pulse, or (2) by focusing two laser pulse to ultra-high intensities (10^{22} - 10^{23} Wcm⁻² and $\gamma \sim 300$) onto a solid target such that: (a) the pump laser beam generates the relativistic electrons of lower energy than in (1) but very high electron-density and (b) the second, probe-laser pulse provides the high electromagnetic field interaction with the relativistic electrons. The two methods are shown schematically in Fig. 2.

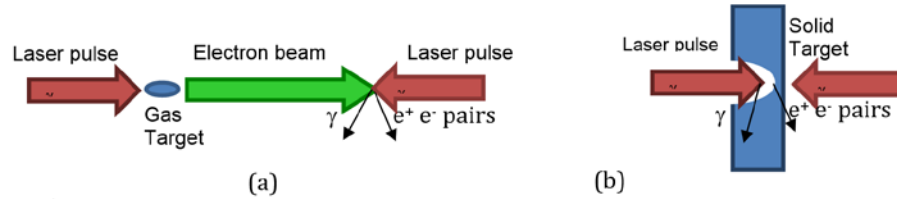


Fig. 2. High Field Physics and QED schematic experiments with two 10 PW pump-probe laser beams.

HPLS TDR 2 starts with proposed commissioning runs in High Field Physics and QED: 12 for E6 interaction chamber with two 10 PW laser beams and 1 for the CETAL interaction chamber with 1 PW laser beam. The CETAL run is in preparation for the ELI-NP runs: CETAL runs will start in 2015 and ELI-NP in 2018. CETAL is situated very close (1 km) from ELI-NP. The proposed experimental runs are representative of the international High Field Physics community being written by 44 authors from 14 European and US organizations. The proposals are classified according to the science area investigated into: Radiation Reaction Physics: Classical and Quantum (2 proposals for solid targets and 4 gas targets at ELI-NP and one at CETAL); Compton and Thomson Scattering Physics: Linear and Non-Linear Regimes (2 proposals with solid targets); QED in Vacuum (2 proposals); Atoms in Extreme Fields (1 proposal with gas target).

Two pump-probe colliding 10 PW laser beams are proposed for the E6 interaction chamber. One 10 PW laser beam is the pump-beam and the other 10 PW laser beam is the probe-beam. The focused pump laser beam accelerates the electrons

to relativistic energies. The accelerated electron bunches interact with the very high electro-magnetic field of the focused probe laser beam. We propose two main types of experiments with: (a) gas targets in which the pump laser-beam is focused by a long focal length ($f/20$ or $f/80$) mirror and drives a wakefield in which the electron bunch is accelerated to multi-GeV energies and then exposed to the electromagnetic (EM) field of the probe laser which is tightly focused ($f/3$); (b) solid targets in which both the pump and probe laser beams are focused on the solid target, one accelerating the electrons in the solid and the other, delayed, providing the high electric field to which the relativistic electrons are subjected.

Section 3 is dedicated to the technical proposal. First the user community requirements are outlined: laser focusing, laser intensity on target, laser beam control and characterization; target characterization; diagnostic for the laser, particle detectors for the laser-interaction products, data acquisition from detectors and diagnostics; interaction chamber and experimental area and radiation.

The proposed interaction chamber E6, focusing configurations and experimental area E6 are presented next. We propose four main focusing configurations for the pump and probe laser beams, two for each type of target: (a) counter-propagating 10 PW focused laser beams and (b) the two 10 PW laser beams focused in the same direction. For solid targets we propose an additional configuration with plasma-mirror on the pump laser beam: the plasma mirror placed between the focusing mirror and target. It is proposed that the 10 PW laser beams will have polarization control and focus control by means of adaptive optics. Initially only one 10 PW may have polarization control and adaptive optics. In order to accommodate the two laser beams and diagnostics the proposed interaction chamber is quasi-octagonal with a diameter of 4.5 m.

The targets section describes a planned robotic target insertion, with load-lock, which will allow long time operation of the interaction chamber without breaking the vacuum and down-time. The main features of the proposed ELI-NP Targets Laboratory are presented.

The section on Diagnostics and Detectors presents proposed active and passive detectors. A large electron spectrometer up to 4 m long is proposed to measure the energy spectrum of multi-GeV electrons including the variation of electron energy when immersed in the high EM field of the probe laser. Other diagnostics will be provided for: gamma-rays, electrons and positrons pairs, protons and ions, plasma characterization, transmitted and reflected laser beam. Section on Control System summarized the TDR on Control and Data Acquisition.

The section on radiation terms and beam-dump presents the: (a) source terms provided by the user community based on simulations of the 10 PW laser-matter interaction - there are no measurements in this regime and ELI-NP will be the first to reach this regime; (b) Nuclear Technologies radiation calculations based on these source terms; (c) radioprotection measures proposed including the 4 m long beam-dump for both electrons with multi-GeV energies and protons with multi-100 MeV

energies. E6 and E1 interaction area is placed in the bunker with 2 m thick concrete walls. The bunker is 20 m wide and 50 m long.

2. PHYSICS CASES: COMMISSIONING RUNS PROPOSED FOR E6 INTERACTION AREA

A programme of High Field Physics and QED commissioning runs is proposed to explore both the onset of radiation damping, via the detection of intense synchrotron emission, and the production of intense electron-positron pairs in ultra-intense laser pulse interactions with solid and near-solid density targets. These runs involve measurement and characterisation of the energy and angular distributions of γ -rays, electron and ions emitted from the laser-plasma interaction. Nuclear activation will be used to diagnose the laser-plasma conditions.

This Section presents the 12 commissioning runs proposed by top world research groups to be performed in ELI-NP, Laser Interaction Area E6 with two 10 PW laser beams and one for the CETAL interaction chamber with 1 PW laser beam. The CETAL proposal is a preparation run for the ELI-NP runs: CETAL run will start in 2015 two years before ELI-NP. The commissioning runs are representative of the international High Field Physics community being written by 44 authors from 14 European and US organizations. The proposals are classified according to the science area investigated into: Radiation Reaction Physics: Classical and Quantum (2 proposals for solid targets and 4 gas targets at ELI-NP and one at CETAL); Compton and Thomson Scattering Physics: Linear and Non-Linear Regimes (2 proposals with solid targets); QED in Vacuum (2 proposals and potentially proposals submitted to E7 interaction area); Atoms in Extreme Fields (1 proposal with gas target).

In order to carry out the proposed runs, HPLS TDR 2 presents a Technical Proposal in the next section. A key element of the technical proposal are the two pump-probe colliding 10 PW laser beams focused in the E6 interaction chamber. One 10 PW laser beam is the pump-beam and the other 10 PW laser beam is the probe-beam. The focused pump laser beam accelerates the electrons to relativistic energies. The accelerated electron bunches interact with the very high electromagnetic field of the focused probe laser beam. Regarding the main types of target: (a) gas targets in which the pump laser-beam is focused by a long focal length ($f/20$ or $f/80$) mirror and drives a wakefield in which the electron bunch is accelerated to multi-GeV energies and then exposed to the electromagnetic field of the probe laser which is tightly focused ($f/3$); (b) solid targets in which both the pump and probe laser beams are focused tightly ($f/3$) on the solid target, one accelerating the electrons in the solid and the other, delayed, providing the high electric field to which the relativistic electrons are subjected.

2.1. Commissioning runs with Pump-Laser, Solid Target and Probe-Laser

2.1.1 Radiation Reaction Physics: Classical and Quantum

2.1.1.1 First investigations of the QED-plasma regime

One of the most exciting prospects for the field of high power laser-plasma interactions is the use of ultra-intense laser radiation to investigate high field-QED physics. At the peak laser intensities achievable using the ELI-NP 10 PW beams (larger than 10^{22} Wcm^{-2}) a new plasma regime is reached in which QED emission processes come into play. The plasma electrons are accelerated so violently in the laser field that they radiate a significant fraction of their energy as gamma-ray photons (synchrotron-like radiation) by strongly non-linear inverse Compton scattering. In this regime, the radiation reaction force, usually neglected, must be included in the electron equations of motion, and a quantum treatment of the radiation reaction force is required. In addition, the emitted gamma-ray photons generate electron-positron pairs in the laser field by the multiphoton Breit-Wheeler process, $\gamma_R + n\gamma_L \rightarrow e^- + e^+$, which generate further photons and pairs, resulting in a cascade of pair production. The reaction rates for these processes become significant when $\eta = \gamma |\mathbf{E}_\perp + \beta \times c\mathbf{B}| / E_S \rightarrow 1$, where γ is the electron Lorentz factor, \mathbf{E}_\perp is the laser electric field perpendicular to the electron motion and E_S is the Schwinger electric field for vacuum breakdown [19].

The prospect of inducing highly nonlinear QED processes in plasma which is either overdense (solid) or relativistically transparent (*i.e.* near critical density), is particularly interesting. Simulations (for example by Ridgers *et al.* [20] and Brady *et al.* [21]) predict that the onset of strong-field QED processes in laser-solid interactions will strongly modify plasma physics processes such as hole-boring and relativistic-induced transparency. The large-scale electromagnetic fields are determined by the plasma physics and set the rates of the QED processes; conversely radiation reaction alters the electron motion and so the large-scale current in the plasma and pair production gives rise to additional charged particles, both altering the plasma processes. The predicted strong feedback between QED processes and plasma physics has given rise to this new regime being referred to as the QED-plasma regime. The ELI-NP 10 PW beams, focused to intensities exceeding 10^{22} Wcm^{-2} , will enable the feedback between QED and plasma processes to be explored experimentally for the first time.

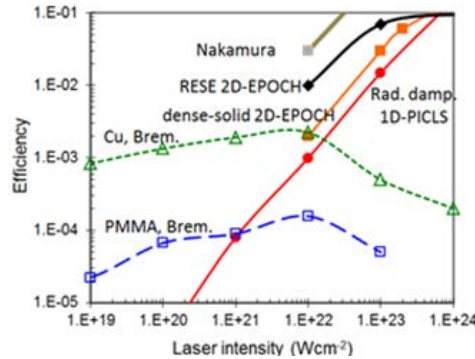


Fig. 3 – Efficiency of laser energy to γ -ray production as a function of laser intensity. The radiation damping calculations (filled symbols) are from PICLS simulations, calculations by Nakamura *et al.* [23] and 2D-EPOCH simulations for solid density and RESE mechanisms. Open symbols are bremsstrahlung calculations for Cu and PMMA plastic.

It will enable the first experimental demonstration of the QED-plasma regime. These experiments are required to test theoretical predictions of the interplay of plasma and QED effects at the heart of the behavior of QED-plasmas, which in turn is fundamental to a wide range of experiments in this new regime of ultra-high laser-matter interactions.

The overall aims of the proposed commissioning run are to: (1) test for the onset of the radiation reaction force, and (2) investigate the feedback on the hole-boring and relativistic-induced transparency plasma processes, in solids and other dense targets irradiated by ultra-intense (above 10^{22} Wcm^{-2}) laser pulses.

To unambiguously observe the creation of a QED plasma we must observe the feedback between QED and plasma processes. Theoretical and simulation studies indicate that we can begin to probe this feedback in laser-solid target interactions at intensities larger than 10^{22} Wcm^{-2} , as shown in Fig. 3. At intensities below 10^{21} Wcm^{-2} the dominant mechanism for the production of hard X-rays and gamma rays is bremsstrahlung radiation, produced by the interaction of electrons with target nuclei. In comparison to direct synchrotron radiation, this process is much less efficient at high intensities and scales with material composition - the cross section for bremsstrahlung scales approximately as Z^2 whereas that for radiation damping is independent of Z (the atomic number).

We plan to measure the following three signatures of the onset of radiation damping due to the synchrotron radiation:

1. The scaling of energetic photon emission with peak laser intensity: As shown in Fig. 3, the integrated γ -ray emission from thin low- Z targets (plastic) should increase massively at 10^{21} - 10^{22} Wcm^{-2} due to the additional synchrotron component, giving a very clear signature of the onset of radiation reaction. An order of magnitude

increase is predicted using the particle-in-cell (PIC) PICLS code and an even larger increase is predicted using the EPOCH code, at 10^{22} Wcm⁻². Synchrotron generation is connected with relativistic transparency and peaks at some fraction of the relativistically corrected critical density for all laser intensities [22]. In high density plasmas the accelerated electrons are confined within a thin skin layer at the laser front. In low-density transparent plasmas, electrons propagating backwards during the laser pulse interaction give rise to more efficient synchrotron production due to the reinjected electron synchrotron emission (RESE) mechanism [21]. A low-density preplasma formed at the front surface of a solid can also lead to efficient photon emission, as demonstrated by Nakamura *et al.* [23]. The enhancements compared to the interaction with a solid are shown in Fig. 3. We plan to quantify the flux of energetic photons produced from solid and near-critical density targets over an intensity range 10^{21} to 10^{22} Wcm⁻². This data will provide an important benchmark for simulations of radiation reaction in this intensity range.

2. The angular profile of energetic photon emission: The synchrotron-like gamma-rays are emitted in differing annular profiles depending upon the main production mechanism, as shown in Fig. 4. These emission patterns are different from bremsstrahlung emission profiles and furthermore change with the polarization of the laser. This provides a signature to distinguish the emission from bremsstrahlung, and should enable the underlying reaction damping effect to be identified. Angular measurements of high energy photon emission will be made with linear (s and p) and circularly polarized light and for solid and near-critical density targets.

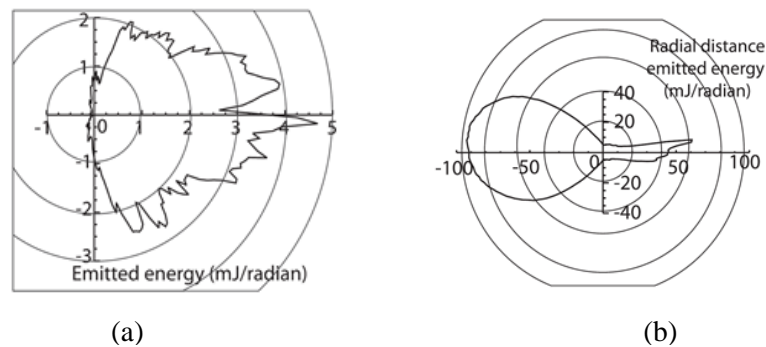


Fig. 4 – Simulation results (using the EPOCH PIC code) of the angular distribution of energetic photons produced by (a) skin depth emission in a solid targets, and (b) the RESE mechanism in which electrons propagate backwards into the incoming laser light. Reprinted figures with permission from [22]

3. Charged particle spectra: Radiation reaction results in a significant reduction in the high energy part of the fast electron spectrum. We will measure changes to the spectrum of electrons emitted from the target and correlate that with

changes to the gamma-ray yield. To test for the expected feedback on classical plasma processes we will characterize changes to the spectrum and spatial distributions of ions accelerated via the hole-boring mode of the laser radiation pressure. In the event that significant energy is lost to synchrotron production due to the radiation reaction force, the hole-boring velocity will decrease, resulting in a corresponding decrease in the maximum ion energy.

The expected feedback on the onset of relativistic induced transparency (RIT) will also be investigated. RIT occurs at relativistic intensities (*i.e.* above 10^{18} Wcm⁻²) due to a reduction in the plasma frequency arising from the relativistic increase in the mass of the oscillating electrons. If the Lorentz factor, γ , of the electrons is sufficiently high an opaque plasma can become transparent, enabling laser light propagation. At intensities sufficiently high enough for radiation reaction to occur, the electron motion is damped, reducing γ and hence the onset of RIT. Correlated measurements will be made of transmitted laser light and the spatial and spectral properties of high energy photons, electrons and ions, in order to elucidate changes to the degree of transmission occurring.

Required Laser pulse parameters and characterization: For the first experiment a single 10 PW beam, focused to a peak intensity of 10^{22} Wcm⁻² is sufficient. As the physics described above scales non-linearly with intensity the highest intensity achievable will be used and in later experiment we would hope to extend the measurements to above mid- 10^{22} to 10^{23} Wcm⁻². The ability to switch between linear and circular polarization is not essential for the first experiment, but would provide an important test of the QED-plasma feedback. It will be an important aim of a follow-on experiment. High intensity contrast is needed (*e.g.* larger than 10^{13} at ns level and exceeding 10^{12} at ps level) to ensure interaction without significant preformed plasma. A plasma mirror may be required to achieve this.

Laser diagnostics required: Measurement of the laser focal spot energy distribution, total energy delivered to target and the pulse duration. This are required to calculate the peak intensity. Intensity-temporal contrast measurement, especially on the rising edge of the laser pulse. A synchronized optical probe, derived from a pick-off from the main 10 PW beam, to characterize the density gradients at the target front surface. This is not essential, but would help to determine whether any degree of preplasma expansion has occurred – the high energy photon production mechanism is sensitive to the extent of the low density plasma that the laser pulse interacts with.

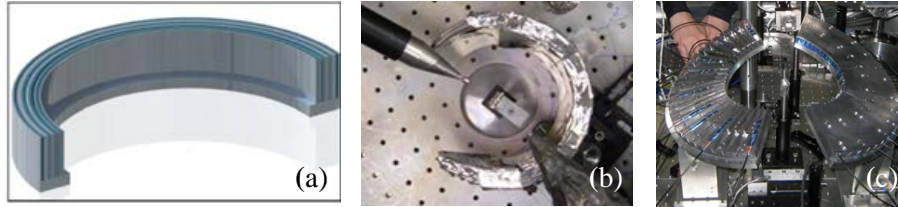


Fig. 5 – Example diagnostics of angular emission of the energetic photons. (a-b) a wrap-around imaging plate detector pack and (c) angular array of scintillators [39].

Required Target fabrication and manipulation: Thin foils varying thickness and Z (e.g. CH, Al, Cu), and foam targets with varying density (5 mg/cc to 100 mg/cc). Manipulation drive systems are required in-chamber for alignment. Accuracy positioning of $0.25\ \mu\text{m}$ in x , y and z -axes and 1 mrad in angular rotation is needed. High resolution microscope optics are required in-situ for accurate positioning of targets.

Diagnostics, detectors and data acquisition:

γ -ray emission: A continuous wrap-around imaging plate detector pack, with a magnetic field to remove electrons, will be employed to measure detailed changes to the angular distribution of the γ -ray emission. We are also developing an angular array of scintillators to make these measurements, as shown in Fig. 5. Noise from bremsstrahlung emission from the target will be minimized by using low- Z targets.

Electron spectrum: The spectrum of accelerated electrons will be measured to diagnose the onset of radiation reaction. This will involve using either the large external electron spectrometer designed for use in E6, or smaller magnetic spectrometers positioned inside the interaction vacuum chamber.

Ion energy spectrum and spatial distribution: Two Thomson parabola ion spectrometers with high proton energy dispersion, coupled to micro-channel plate detectors and phosphor screens or imaging plates will be used to measure changes to the ion energy spectra, resulting from changes to the ion hole-boring velocity.

Reflected and transmitted laser light: The laser light reflected from the target and transmitted through it will be spectrally and spatially sampled. The spatial-intensity profile of the fundamental and 2ω and 3ω harmonics will be imaged onto CCDs to diagnose changes to the curvature and uniformity of the critical density surface induced by hole-boring. The spectrum of the reflected light will be measured on- and off-axis using two spectrometers to quantify shifts in the fundamental and harmonics due to recession of the plasma surface. The energy of the reflected light will be measured using a calorimeter behind a hole in the screen to determine relative

changes to the total energy absorbed. These measurements will be correlated to measurements of the particle and radiation emission.

2.1.1.2 Enhancement of synchrotron radiation production by collective effects in the classical radiation dominated regime

Recent theoretical studies of high intensity laser pulse interactions with matter advocate new schemes for the acceleration of charged particles, electrons and ions, to relativistic energies [24] and the generation of intense fluxes of γ -rays [25]. These theoretical studies provide a solid background for experiments planned with new multi-10 PW laser installations such as the ELI project [26]. This will enable investigations of new physical regimes in which charge separation field plays an important role and which have not yet been explored in experiment. This is very promising for many applications, such as cancer therapy, radiography and the fast ignition approach to inertial fusion [27]. Besides, it has been shown in several publications that the radiation reaction force acting on ultra-relativistic electrons accelerated in the strong laser field intensities above 10^{22} Wcm⁻² will strongly impact their dynamics [25, 28–35]. It has been demonstrated that the radiation reaction force leads to a contraction of the electron phase space volume with time, localized in the ambient laser field, in the case of non-interacting electrons [20, 32]. The possibility to detect radiation reaction effects has been explored in references [21, 25, 36–37]. However, to date, studies of synchrotron radiation have not considered the role of the collective field related to self-consistent electric fields in plasma.

The goal of this commissioning run is to demonstrate the numerically strong feedback of the collective plasma effects on the production of synchrotron radiation via radiation reaction. The collective effects increase with the target plasma ion mass and thickness and are crucial for converting a significant fraction of the laser energy into an intense radiation. Our objective is to measure the effect that the ion mass has on radiation reaction physics.

Brief theory and expected results: At peak laser intensities higher than mid- 10^{22} Wcm⁻² collective plasma effects play an important role on synchrotron radiation generation, as shown numerically in references [35] and [38]. The importance of the collective effects depends strongly on the target thickness and on the ion mass [38]. We can expect to generate intense photons with energies up to 100 MeV in the case of a thick target (100 microns), with of the order of 30% of the laser energy converted into synchrotron radiation in the case of thick proton plasma. These features are relevant in the classical radiation dominated regime when the interaction conditions satisfy $n_e/n_c \ll a_L$, where n_e is the plasma density, n_c is the critical density and a_L is the normalized vector potential. In this regime, the conversion of laser energy into high energy photons increases with increasing ion mass, with a corresponding decreasing in the energy conversion into ions.

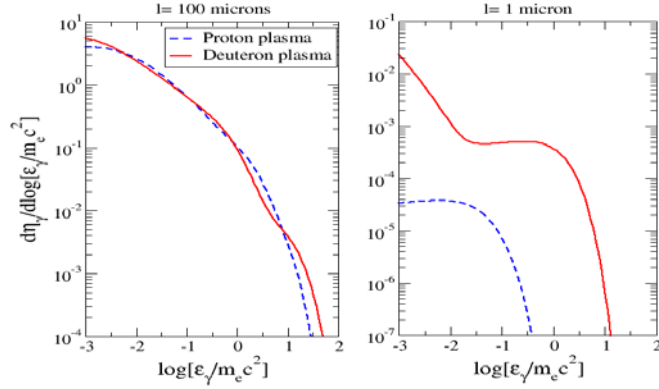


Fig. 6 – Simulated photon energy spectrum at $t = 115$ fs in the case of a (a) thick target and a (b) thin target, for circularly polarized light focused to a peak laser intensity equal to 4×10^{22} Wcm $^{-2}$. The target density is $n_e = 10 n_c$. The effect of target mass is more clearly observable when comparing the thin target case for protons and deuterons

The spectrum of the photons produced via this process can provide a clear signature of the electrostatic field effect on the synchrotron radiation. Fig. 6 shows the photon energy spectrum in the case of (a) a thick target and (b) a thin target. On the one hand, the electrostatic field (growing with the target thickness) increases the synchrotron radiation production and on the other it tends to broaden the frequency interval of the photons.

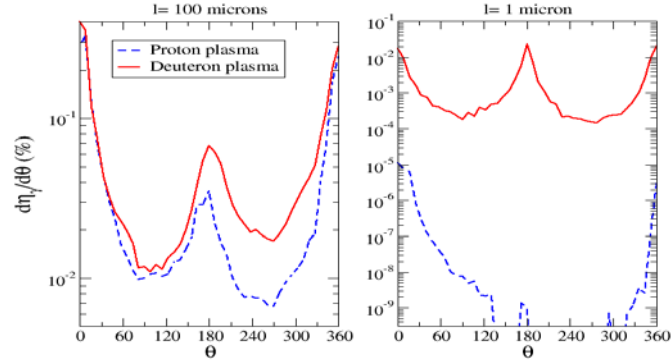


Fig.7 – Angular distribution of the synchrotron radiation as a function of the polar angle, again for circularly polarized light focused to a peak laser intensity equal to 4×10^{22} Wcm $^{-2}$ and target density equal to $10 n_c$.

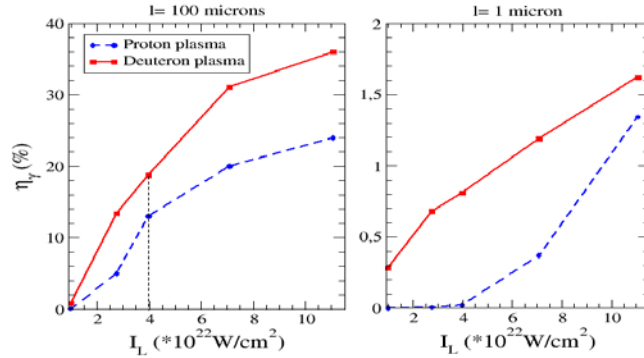


Fig.8 – Laser energy conversion into synchrotron radiation as a function of the laser intensity, for proton and deuteron plasmas and for (a) a thick target and (b) a thin target. Here, the laser light is circularly polarized and target density equal to $10 n_c$.

To demonstrate the effect of ion mass on synchrotron radiation production, the exploration of the angular distribution of the radiation over the polar angle θ can be very useful. Here, the angle θ represents the angle between the photon momentum and the laser field propagation axis. As shown in Fig. 7, the higher the ion mass, the more synchrotron radiation is emitted to the opposite direction to that of the laser field.

When analyzing the variation in the laser energy conversion into photons (shown in Fig. 8), it is found that at high peak laser intensity the difference between a proton plasma and a deuteron plasma is larger for a thick target (the conversion efficiency changes from 10% to 15%). At a peak intensity of 4×10^{22} Wcm $^{-2}$ the ratio of the laser energy conversion into photons for a deuteron plasma over an equivalent thickness proton plasma is very high for a thin target (more than an order of magnitude). For all laser intensities between 10^{22} and 10^{23} Wcm $^{-2}$, the difference between the laser energy conversion into photons for thin targets and for thick targets is high (from a few percent to several tens of percent).

Commissioning run: We propose to use the ELI-NP laser facility to perform the first run to verify the predicted ion mass effect on radiation reaction physics and the corresponding changes to the collective plasma dynamics. In the proposed run, pure hydrogen and deuteron targets will be produced using cryogenic target technology, which is being developed to produce targets with thickness down to 10 μm or less. In the collisionless regime obtained with ultra-high intensity and ultra-high energy lasers interacting with low Z targets, the dynamics of the ions is dominated by the ion charge-to-mass (Z/m) ratio. As a first step, C-D plastic target foils can be used to produce a fully ionized C-D plasma with $Z/m=0.5$, the same as a deuteron plasma.

Required Laser pulse parameters and characterization: For the first run a single 10 PW beam, focused to a peak intensity of mid- 10^{22} Wcm⁻² is sufficient. In later stages we would hope to extend the measurements to 10^{23} Wcm⁻² to investigate the predicted intensity scaling effects shown in Fig. 8. Circular polarization is required in order to optimize the collective effects, whilst avoiding strong electron heating. High intensity contrast is needed (*e.g.* larger than 10^{13} at ns and exceeding 10^{12} at ps level) to ensure interaction without significant preformed plasma. A plasma mirror may be required to achieve this.

Laser diagnostics required: Measurement of the laser focal spot energy distribution, total energy delivered to target and the pulse duration are required to calculate the peak intensity. Intensity-temporal contrast measurement are needed, especially on the rising edge of the laser pulse. A synchronized optical probe, derived from a pick-off from the main 10 PW beam, to characterize the density gradients at the target front surface. This is not essential, but would help to determine whether any degree of preplasma expansion has occurred – the high energy photon production mechanism is sensitive to the extent of the low density plasma that the laser pulse interacts with.

Required Target fabrication and manipulation: The basic targets consist of plastic (C-H and C-D) films with thickness in the range 0.1-100 μ m. In addition to solid density, the target will be decompressed to lower density using a separate drive laser pulse to initialize ionization and plasma expansion. Cryogenic technology will be used to produce pure hydrogen and deuterium targets with thickness down to 10 μ m or less. We are developing this technology at the Rutherford Appleton Laboratory. Manipulation drive systems are required in-chamber for alignment.

Diagnostics, detectors and data acquisition:

Synchrotron emission: Several options exist to measure the angular emission of the synchrotron photons produced, including a continuous wrap-around imaging plate detector pack, with a magnetic field to remove electrons, and an angular array of scintillators, as shown in Fig. 5 (c) (developed at the University of Strathclyde). Additional techniques are being explored for the detection of higher energy radiation (because of the decreasing sensitivity of the scintillating crystals to increasing energy), and we are presently testing a new spectroscopic technique enabling spectral measurements beyond 400 keV. The precise solution adopted depends on the space available surrounding the target mount.

Electron spectrum: The spectrum of accelerated electrons will be measured to diagnose the onset of radiation reaction. This will involve using either the large external electron spectrometer designed for use in E6, or smaller magnetic spectrometers positioned inside the interaction vacuum chamber.

Ion energy spectrum and spatial distribution: In addition to measuring the

energy spectrum and angular distribution of the radiated photons, it is important to measure these properties of the proton and deuterium ions produced as the target thickness, density and composition are varied and the laser drive parameter including intensity are changed. Two Thomson parabola ion spectrometers with high proton energy dispersion, coupled to micro-channel plate detectors and phosphor screens or imaging plates will be used to measure changes to the ion energy spectra, resulting from changes to the ion hole-boring velocity. Stacked dosimeter film and activation foils will be used to measure the spatial-intensity distribution of the accelerated ions. The measurements will be correlated to changes in the photon and electron beam properties.

Reflected and transmitted laser light: The laser light reflected from the target and transmitted through it will be spectrally and spatially sampled. The spectrum of the reflected light provides a diagnostic of the recession velocity of the plasma surface (due to the Doppler shift). The energy of the reflected light will be measured using a calorimeter behind a hole in the screen to determine relative changes to the total energy absorbed. These measurements will be correlated to measurements of the particle and radiation emission and are important to benchmark the simulation results. Our simulation results (Figs. 6–8), particularly for thin targets, show clear differences in the total energy conversion, the spectrum and the angular distribution of the emitted synchrotron radiation between the $Z/m=1$ (proton) and $Z/m=0.5$ (deuteron) plasma. This level of difference should be measurable experimentally, particularly in thin, low- Z targets for which the electron energy conversion to bremsstrahlung is minimized.

2.1.2 Compton and Thomson Scattering: Linear and Non-Linear Regimes

2.1.2.1 Ultra-intense XUV pulses

High Harmonic generation from solid density plasmas acting as relativistically oscillating mirrors (ROM) [40-43] is predicted to allow the generation of extremely bright coherent radiation extending into the keV range. The aim would be the demonstration of the world's brightest attosecond pulse train using ELI-NP, which will be of interest not only from a proof of principle perspective, but also as a probe of vacuum QED interactions, ultra-fast plasma probe. Demonstration of this capability will enable many classes of experiments at ELI-NP that require ultra-bright, ultra-intense XUV and X-ray probes. The highest harmonic scaling to keV photon energies have so far only been produced with PW lasers capable of $I \lambda^2 > 10^{20} \text{ Wcm}^{-2}$ – this regime has so far not been accessible to femtosecond lasers

with sufficient pulse contrast. ELI-NP's 10 PW beamline provides an excellent opportunity to reach the high conversion efficiencies predicted by theory [44, 45].

To achieve this, intensities in the regime of 10^{21} Wcm⁻² are necessary – easily accessible with multi-PW laser systems. In this regime a conversion efficiency scaling of $\eta \sim n^{-8/3}$ is predicted in the ultra-relativistic limit – corresponding to mJ pulses with femtosecond duration. If these predictions can be realized in practice, the XUV source and ELI-NP would be the most powerful XUV source ever created and capable of ultra-fast XUV probing of most experimental interactions at ELI-NP – adding significant science capability.

An intriguing property of ROM harmonics is that the harmonic generation process results in a spatial as well as temporal compression of the electromagnetic energy of the laser. The work by Gordienko *et al.* (figure below) shows that that enhanced focusability of keV photons and the compression from femtosecond to attosecond pulse structure results in a rapid increase of the intensity in the coherent harmonic focus (CHF) [45]. Curved targets can act as focusing mirrors to achieve the intensity enhancement. Note that the predicted intensities are beyond what is considered possible with optical lasers. Amongst the ELI pillars, ELI-NP is uniquely equipped to exploit this regime, since it is the only femtosecond 10 PW laser planned.

The combination of two 10 PW beams allows colliding pulse commissioning runs with CHF beams to be considered in the future – opening up a wide range of scientific possibilities in high field interactions.

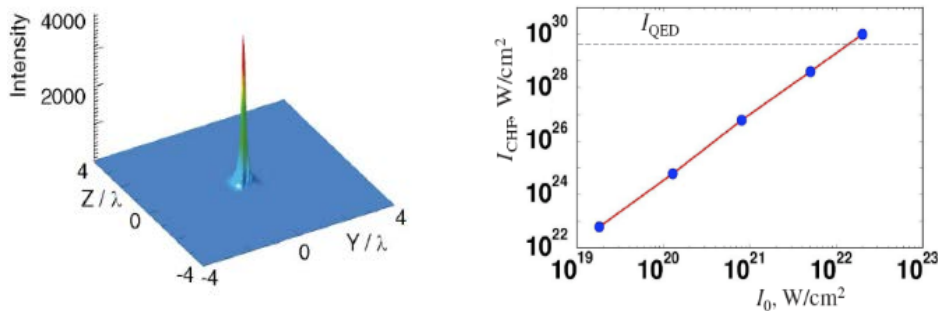


Fig. 9 – Enhancement of peak intensity by ROM harmonics up to the Schwinger limit is theoretically possible. Reprinted figures with permission from [45].

Observable: Easily detected strong harmonic spectra significantly above background with signal to noise ratio of 10-100.

Required Laser pulse parameters and characterization: A single $f/3$ focusing mirror is needed for intensity reaching 10^{21} - 10^{22} Wcm^{-2} . In addition, tools to characterize the repulse are necessary and can be easily implemented in the vacuum chamber.

Laser diagnostics requirements: Characterization of laser focal spot at low power, energy distribution and chromatic aberrations are needed to calculate peak intensity. Shot-to-shot pulse diagnostics in laser bay are essential (at least far-field, near-field, pulse duration). Focal spot diagnostics and wavefront sensor in the interaction chamber; plasma mirror; spectrometer to characterize transmitted laser light.

Diagnostics: Flat-field and X-ray spectrometers.

Target Requirements: x - y - z target manipulators and rotating target holding flat substrate.

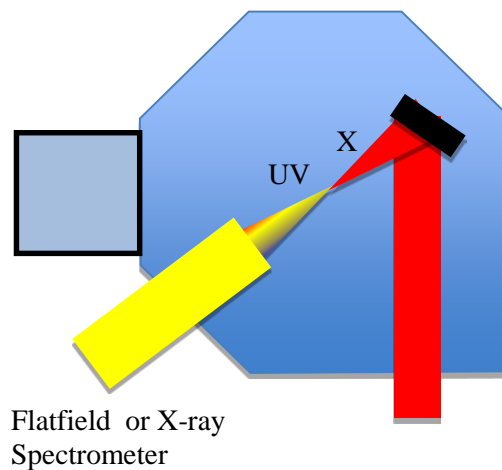


Fig. 10 – Schematic of XUV generation set-up. One 10 PW beam is focused using an $f/3$ mirror.

2.1.2.2 Deceleration of Very Dense Electron and Ion Beams

In nuclear physics the Bethe-Bloch formula [47] is used to calculate the atomic stopping of energetic individual electrons [46] by ionization and atomic excitation:

$$-\left[\frac{dE}{dx}\right]_I = K \cdot z^2 \frac{Z}{A} \frac{1}{\beta^2} \left[\frac{1}{2} \ln \frac{2m_e c^2 \beta^2 \gamma^2 T_{max}}{I^2} - \beta^2 - \frac{\delta}{2} \right] \quad (4)$$

and ions:

$$-\left[\frac{dE}{dx}\right] = 4\pi n_e \frac{Z_{eff}^2 e^4}{m_e v^2 (4\pi\epsilon_0)^2} \left[\ln \left(\frac{2m_e v^2}{I(1-\beta^2)} \right) - \beta^2 \right] \quad (5)$$

where I is the ionization potential, n_e the density of the electrons, m_e the mass of the electron, v is the ion velocity, $\beta = v/c$, T_{max} is the maximum kinetic energy which can be imparted to a single electron in a single collision, and Z_{eff} is the effective charge of the ions. For relativistic electrons the other important energy loss is bremsstrahlung with:

$$-\left[\frac{dE}{dx}\right]_R = \left(\frac{4\pi n_e}{m_e c^2} \right) \frac{Z}{137\pi} (\gamma - 1) \ln \left(183 b Z^{-\frac{1}{3}} \right) \quad (6)$$

The approximate ratio of the two loss processes [2] is:

$$\left[\frac{dE}{dx}\right]_I / \left[\frac{dE}{dx}\right]_R = E Z / 1600 m c^2 \quad (7)$$

Thus radiation loss is dominant for high energy electrons *e.g.* $E \geq 100$ MeV and $Z = 10$. If, however, the atomic stopping becomes orders of magnitude larger by collective effects, the radiation loss can be neglected. For laser acceleration the electron and ion bunch densities reach solid state densities, which are about 15 orders of magnitude larger compared to beams from classical accelerators. Here collective effects become important. One can decompose the Bethe-Bloch equation according to Ref. [48] into a first contribution describing binary collisions and a second term describing long range collective contributions:

$$-\left[\frac{dE}{dx}\right] = 4\pi n_e \frac{Z_{eff}^2 e^4}{m_e v^2 (4\pi\epsilon_0)^2} \left[\ln \left(\frac{2m_e v^2}{e^2 k_D} \right) + \ln \left(\frac{k_D v}{\omega_p} \right) \right] \quad (8)$$

Here k_D is the Debye wave number and ω_p is the plasma frequency of the electrons. Similar to bubble acceleration [49] but now with opposite phase for deceleration a strong collective field is built up by the blown-out electrons that decelerates them much faster than the processes that take effect for individual charged particles. Typical electric fields E are:

$$E = m_e \omega_p v \frac{n_b}{n_b e}, \quad (9)$$

where n_b is the charge density of the bunch. In Ref. [20] we discuss this mechanism of collective deceleration of a dense particle bunch in a thin plasma, where the particle bunch fits into part of the plasma oscillation and is decelerated 10^5 - 10^6 stronger than predicted by the classical Bethe-Bloch equation [47] due to the strong collective wakefield. For ion deceleration we want to use targets with suitable low density. These new laws of deceleration and stopping of charged particles have to be established to use them later in experiments in an optimum way. We may also discuss the opposite effect with a strongly reduced atomic stopping power that occurs when sending an energetic, solid state density ion bunch into a solid target. For this target the plasma wavelength ($\lambda_p \approx 1$ nm) is much smaller than the ion bunch length (about 100 nm) and collective acceleration and deceleration effects cancel each other. Only the binary collisions are important. Hence, we may consider the dense ion bunch as consisting of 300 layers with Å distances. Here the first layers of the bunch will attract the electrons from the target and - like a snow plough - will take up the decelerating electron momenta. The predominant part of the ion bunch is screened from electrons and we expect an approximately 10^2 fold reduction in stopping power. The electron density n_e is strongly reduced in the channel because many electrons are driven out by the ion bunch and the laser. Again all these effects have to be studied in detail.

It is expected that the resulted very dense electron and ion bunches should have a time evolution (decay in time) and the decay products are emitted at different times and angles. Therefore, for characterization of the dense bunches and their time evolution, the detection system need to capture the decay products, emitted at different times (analogous to time of flight measurements), and measure their angular distributions. Of course, the temporal evolution which can be followed vary greatly depending on the temporal resolution of the diagnosis system. In a preliminary phase, it is expected that electrons and ions are emitted due to the Coulomb explosion of a part of the initially formed bunch (pre-bunch emission). Then, the remained bunch will have a slower temporal evolution, which can be followed in dependence of its time of flight in free space. The experimental study of deceleration of dense, high speed bunches of electrons and ions will require:

Bunch's characterization in free space: its components, their energies and the ion charge states, their angular distribution and temporal evolution; due to the large number of particles, the detection solid angles must be small (of the order of 10^{-7} sr or less).

Tracking the changes introduced by bunch's passing through different materials (solid or gas) and their deceleration study. Studies will be carried out

depending on laser power and target type and thickness and for deceleration - depending on material type and its thickness.

The same detection system could be used for both diagnosis in free space and diagnosis after passing through a material. A rapid characterization may be done with a Thomson parabola ion spectrometer, and an electron magnetic spectrometer, implying measurements of the emissions at different times and possibly their angular distribution, in the case they are relevant. A more complete analysis will require a diagnosis system working in real-time, using magnetic spectrometers and detection systems with high granularity or with position sensitive reading in the focal plane (*e.g.* stacks of $\Delta E-E$ detectors, with ionization chambers and Si or scintillation detectors). Even if the laser pulse frequency is small, the nuclear electronics can be triggered in the usual way.

Observable: Energy loss in media such as gas jets or foil targets. Prerequisite: Successful demonstration of dense Radiation Pressure Acceleration (RPA) bunches of ions or high charge electron bunches.

Required Laser pulse parameters and characterization: Single $f/3$ optics with intensity reaching 10^{21} - 10^{22} Wcm^{-2} ; $f/20$ or $f/3$ probe beam to provide particle/X-ray backlighter with intensity exceeding 5×10^{19} Wcm^{-2} .

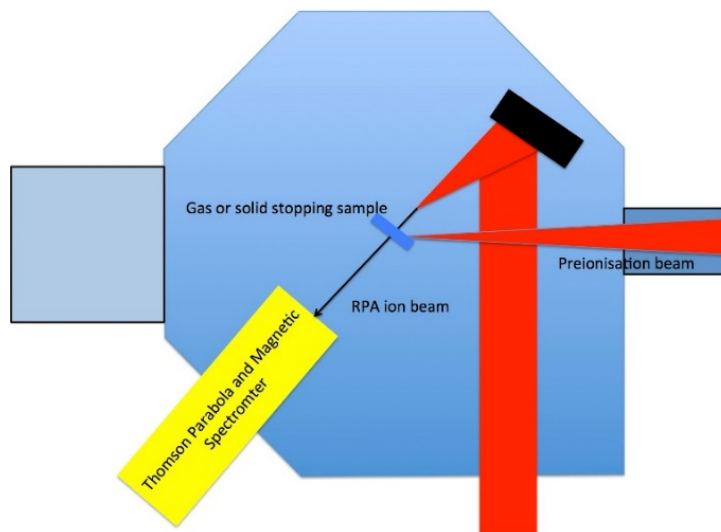


Fig.11 – Experimental Schematic for stopping experiments. Second beam can be $f/20$ or $f/3$.

Laser diagnostics requirements: Characterization of laser focal spot at low power, energy distribution and chromatic aberrations needed to calculate peak intensity. The femtosecond synchronization system on target using frequency domain interferometer requires optical tables in the area and optical windows on

chambers. Shot-to-shot pulse diagnostics in laser bay are essential (at least far-field, near-field and pulse duration); Focal spot diagnostics and wavefront sensor in the interaction chamber; Plasma Mirror and spectrometer to characterize transmitted laser light.

Diagnostics: Magnetic spectrometer, Thomson parabola and scintillation screens.

Target Requirements: Two x - y - z target manipulators; thin foil targets (nm to micron scale); Plasma Mirror to enable normal incidence interaction; gas and solid targets (foils and jets) – either pre-ionized with the second beam or not.

2.2 Commissioning runs with Pump-Laser and Gas Target, Electron-beam and Probe-Laser

2.2.1 Radiation Reaction Physics: Classical and Quantum

2.2.1.1 Exploring Strong-Field QED with Ultra-Intense Lasers

Current high-power laser facilities can focus light to extremely high intensities (10^{21} - 10^{22} Wcm⁻²). At such extreme intensities we are on the verge of a regime where the electromagnetic fields in the laser focus will be so strong that very nonlinear quantum electrodynamics (QED) effects, not yet seen in the laboratory, will play a critical role in determining the plasma dynamics [20]. A QED plasma similar to that present in the magnetospheres of pulsars is created [51]. These nonlinear QED processes become important when the electric field in the electron's rest frame (E_{RF}) approaches the critical field for QED (the Schwinger field $E_S = 1.3 \times 10^{18}$ Vm⁻¹) [52]. Here we propose studying these effects in the collision of an electron bunch (energy $\gamma m_e c^2$) with an intense laser pulse (peak intensity I). In this case the quantum parameter is given by

$$\eta = E_{RF}/E_S \sim (\gamma m_e c^2 / 1 \text{ GeV}) (I / 10^{22} \text{ Wcm}^{-2})^{1/2} \quad (10)$$

Experiments of this type using high energy electron beams produced by particle accelerators have probed the weakly non-linear strong field QED regime (SLAC [53]). Recently, all-optical equivalents been performed where the electron beam was produced by laser wakefield acceleration [54–56]. These have the potential to probe the extremely non-linear $\eta \sim 1$ strong field QED regime but the necessary parameters for reaching this regime, namely $\gamma m_e c^2 > 1$ GeV, $I \sim 10^{22}$ Wcm⁻² cannot be achieved simultaneously and reliably on current PW laser facilities.

ELI-NP will be able to reach these parameters and thus will enable the first exploration of several fundamental strong-field QED processes: (i) very non-linear inverse Compton scattering and the resulting radiation reaction; (ii) very nonlinear Breit-Wheeler pair production. The transition to quantum radiation reaction is important as it resolves long standing difficulties with classical radiation reaction. Recently, Ilderton and Torgrimmon showed that a description of radiation reaction within the framework of strong-field QED is only compatible with a subset of classical theories [57]. Furthermore, quantum effects are much larger than the relatively small differences between classical models for η larger than 0.1. The first observation of Breit-Wheeler pair production in the very nonlinear regime will be very important as the cross-section for this process underpins pair cascades in extreme astrophysical environments such as pulsar magnetospheres. As well as being of interest for fundamental physics, the prolific and collimated generation of gamma-rays (and pairs) in the interaction could lead to a gamma-ray light (antimatter) source of unprecedented brightness [58]. Furthermore, the processes (i) and (ii) are also the critical QED processes in laser-generated QED-plasmas, which will dominate all laser matter interactions at 10 PW and above. Models for these processes now form a foundational element of simulation codes for the interaction of 10 PW lasers with matter. Benchmarking the QED model used in these codes is essential if theories of laser generated QED-plasmas are to be built up and future laser-plasma experiments moving beyond today's intensity frontier are to be understood.

Objectives. We propose using the unique capabilities of ELI-NP to, for the first time:

1. Observe the transition to the very nonlinear Compton scattering regime, radiation reaction in this regime and the transition of radiation reaction from a classical (deterministic) to a quantum (stochastic) force.
2. Measure the cross-section for strongly nonlinear Breit-Wheeler pair production.

Laser, target and diagnostic requirements: The experimental configuration is shown in Fig. 12. We require: (i) a long focal length optic (*e.g.* $f/20$), (ii) a gas-jet target. The long focal length will be used to focus one 10 PW laser pulse into the gas-jet, generating an electron beam above 1 GeV by laser wakefield acceleration. (iii) An $f/3$ optic to focus the second 10 PW onto the counter-propagating electron beam reaching intensity of 10^{22} Wcm^{-2} . The resulting collision of electron beam and

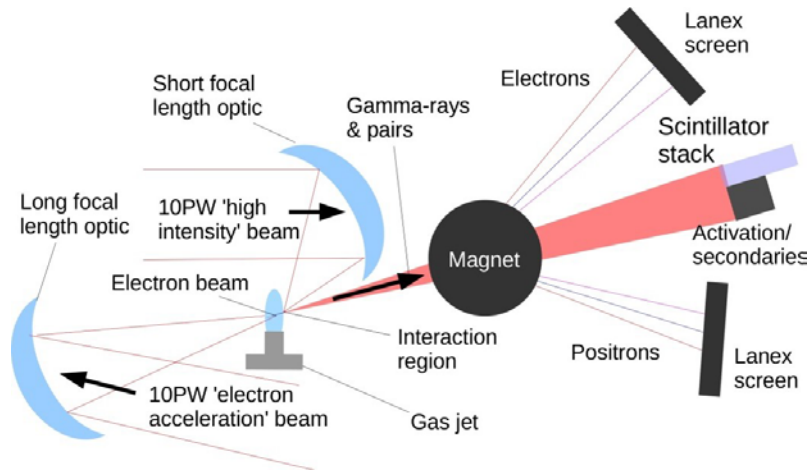


Fig.12 – The experimental setup.

laser pulse will produce γ -rays and pairs whose spectrum will be measured using (iv) a stack of CsI scintillators (as used in [56]); (v) high Z -materials for nuclear activation measurements and secondary positron production. This will allow us to detect gamma-rays over the wide range of energies (100 MeV - GeV) expected. (vi) magnetic electron/positron spectrometer: the electron and positron spectra will be measured with a magnetic spectrometer consisting of a magnet and lanex screens as shown in Fig. 12. (vii) An adjustable aperture will be required. This will allow us to enlarge the focal spot of the high-intensity colliding laser pulse, overcoming the key challenge of this experiment: alignment of the high-intensity laser pulse with the electron bunch. The aperture will lower η but simulations show that η will be sufficient to measure the transition to the non-linear regime and quantum effects on radiation reaction. Once initial results have been obtained the aperture size will be increased up to the full beam diameter, thereby increasing η .

Expected outcomes

1. Inverse Compton scattering and radiation reaction. The very nonlinear Compton scattering regime requires that the high intensity pulse have an intensity considerably above 10^{18} Wcm^{-2} and radiation reaction becomes important at η larger than 0.1, *i.e.* 10^{21} Wcm^{-2} for a GeV electron beam. The SLAC and recent Gemini experiments have reached the weakly non-linear regime, where radiation reaction did not play a role. Conservative estimates predict that ELI-NP will be able to reach electron energies of several GeV and intensities larger than 10^{21} Wcm^{-2} in the high-intensity pulse, even with some aperturing of the beam – assuming a focal spot area of the high intensity pulse of approximately 40 microns (similar to that successfully used in [56]). In this case the very nonlinear and $\eta \sim 0.1-1$ quantum regime is accessible. Signatures of the transition to this regime will be clear: the emitted

gamma-ray spectrum transitions from $4\gamma^2$ times the laser photon energy to a very broad synchrotron-like spectrum centered on 0.5η times the electron energy $\alpha\gamma$ as one moves to the nonlinear regime.

As shown in Fig. 14, the electrons lose a substantial fraction of their energy due to radiation reaction (more than 40%) and their energy spectrum is broadened by quantum effects, developing a characteristic two peaked structure (the classical prediction has a single peak centered on the red line in Fig. 14) [59]. Quantum effects also lead to an order of magnitude reduction in radiation reaction below the classical prediction [60]. These effects are dramatic and will be measurable against control shots, where the counter-propagating high-intensity pulse is absent (or mistimed/misaligned), even for a large spread in initial electron energies.

2. Breit-Wheeler Pair production. The cross-section for multiphoton Breit-Wheeler pair production in the very non-linear regime, including any additional effects such as photon polarization, is critically important to current models describing the generation of dense pair plasmas by pair cascades in both next-generation laser-plasma interactions [20] and pulsar magnetospheres [51]. 3D calculations, the results of which are shown in Fig. 14, show that for an intensity $3 \times 10^{22} \text{ Wcm}^{-2}$ we can expect on the order of 10^6 - 10^7 pairs produced in each interaction between laser beam and colliding laser pulse (assuming an electron beam charge of 10-100 pC). Numbers of this order can be detected in current laser-plasma

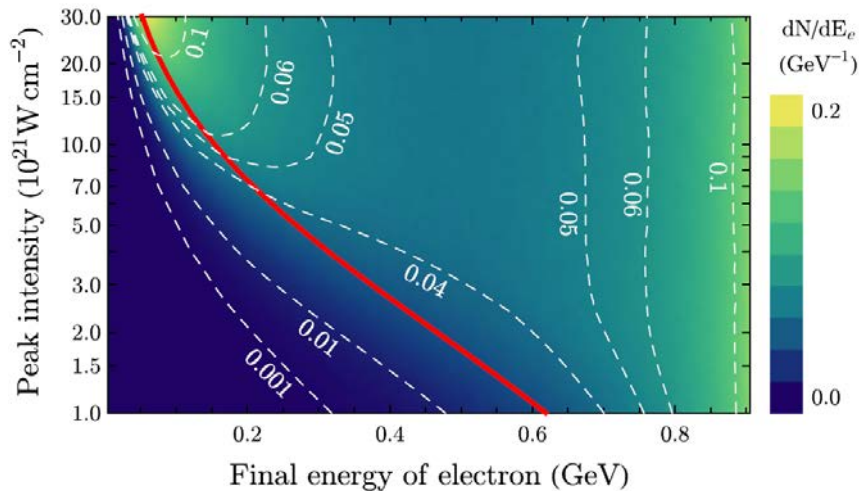


Fig. 13 – Electron energy spread after the interaction of a 1 GeV monoenergetic beam with a diffraction-limited laser pulse (from 3D simulations) and the classical prediction (red line). Reprinted figure with permission from [59].

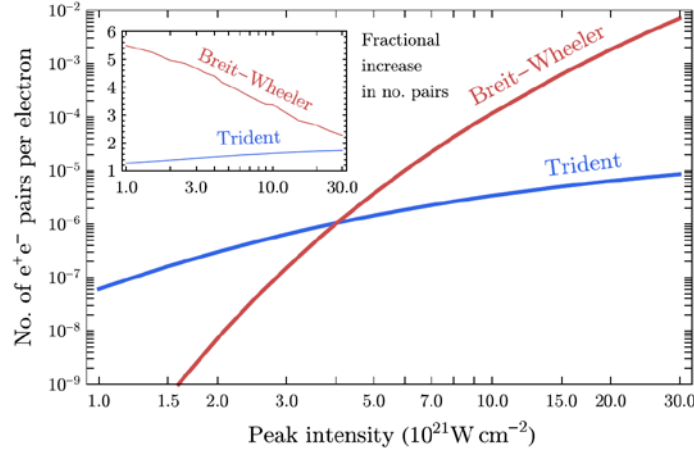


Fig. 14 – Pair production by the Breit-Wheeler and Trident mechanisms (from 3D simulations). At the highest intensity Breit-Wheeler dominates. Inset - enhancement due to quantum stochastic effects. Reprinted figure with permission from [59].

experiments [61]. This is compared to the SLAC experiment where 106 ± 14 pairs were generated over many shots. Furthermore, stochastic effects on the radiation reaction force lead to an enhancement above 2 in the number of pairs, providing an additional measure for testing the QED radiation reaction model.

2.2.1.2 High Field Studies and Electron Beam Cooling by Radiation Reaction in Intense Laser Pulses

The ELI-NP facility will allow focused laser intensities of approximately $5 \times 10^{22} \text{ W cm}^{-2}$ or higher to be achieved for the first time, enabling investigation of new physical phenomena at the interfaces of plasma, nuclear and particle physics. At these intensities, the electric field has a maximum value of 10^{15} V m^{-1} , approaching the Schwinger critical field [19, 52] typical of QED processes, $E_S = 1.3 \times 10^{18} \text{ V m}^{-1}$. We propose the study of Radiation Reaction and Electron Beam Cooling; Strong Field Quantum Electrodynamics (QED) effects; and the resulting production of ultra-bright sources of gamma-rays that could be used for nuclear activation. Two powerful, synchronized 10 PW laser beams will be focused in the E6 Interaction Chamber on either gas or solid targets. One 10 PW beam is considered as the pump beam while the other is the probe beam. A fraction of the focused pump beam is used to accelerate plasma electrons to relativistic energies in a laser-plasma Wakefield accelerator and the focused probe beam provides an extremely high counter-propagating electromagnetic field.

Advances in laser technology are resulting in new science and new applications using laser-driven particle and photon beams. Focused terawatt and petawatt laser pulses at state-of-the-art laser facilities can have intensities as high as 10^{21} Wcm⁻². These are now routinely used to accelerate femtosecond-duration electron bunches to several GeV energies. The collision of these GeV electron beams with intense laser pulses, such as from the ELI-NP 10 PW lasers, will result in copious radiation from the electrons. Radiation will be emitted at extremely high rates, which will essentially change the radiation process and lead to new phenomena such as radiation reaction dominated beam dynamics.

Charged particles in an oscillating electromagnetic field accelerate and emit electromagnetic radiation. To compensate for the energy and momentum carried away by this radiation, the particle must experience a recoil force. The nature of radiation reaction is one of the most profound open questions in physics, and remains controversial even after more than a century of investigation. The fundamental theory describing radiation reaction, the Lorentz-Abraham-Dirac (LAD) equation [1,62–63], which is based on nothing more than Maxwell's equations and the assumption that the electron is a point charge, yields unphysical predictions such as violation of causality. A number of alternatives have been proposed, but none has gained universal acceptance [64].

One obstacle to our understanding of radiation reaction is the lack of experimental data. Even for electrons, the particles most susceptible to radiation reaction effects, this force is negligibly small in fields possible at existing laser facilities. In contrast, the nonlinear behavior that depends on the field strength at intensities at ELI-NP, not only should result in measurable effects, but radiation reaction is expected to dominate the electron dynamics. Radiation reaction is also enhanced in high frequency fields, such as those produced by nonlinear Compton scattering.

In an intense laser field, electrons gain a transverse momentum proportional to the normalized vector potential $a_0 = eA/m_e c$. Electrons additionally gain a longitudinal drift momentum proportional to a_0^2 . Scattering of the laser beam off a counter-propagating relativistic electron beam with $\gamma \gg 1$ gives rise to a back-scattered laser pulse with a frequency upshifted by a factor $4\gamma^2$. When $a_0 \leq 1$, single photons are backscattered with $\hbar\omega' \approx 4\gamma^2 \hbar\omega_0$ and a peak brilliance that depends on beam emittance and peak current. When the scattered photon energy approaches the electron energy, Compton recoil limits the scattered photon energy, causing “photon pileup” close to the maximum energy. In the ELI-NP E6 high-field setup, it is envisaged that a brilliant gamma-ray source based on resonant betatron emission will give a photon energy of up to 20 MeV. Scattering this off a relatively low energy electron beam from a LWFA will lead directly to the Compton regime. However, for $a_0 \gg 1$, electrons oscillate nonlinearly in the laser field, leading to many

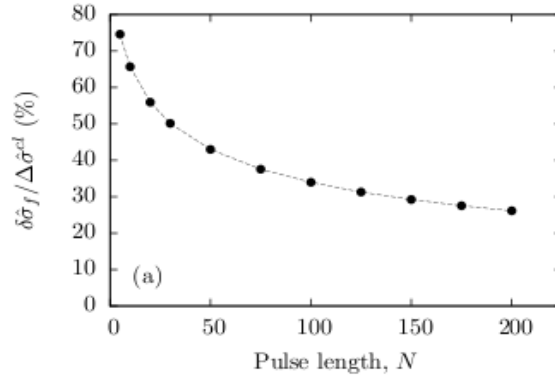


Fig. 15 – Classical and quantum predictions converge as the laser pulse is stretched and the peak intensity reduced. Figure reproduced with permission from [65].

harmonics in a spectrum which peaks at the harmonic number $h_c \approx a_0^3$, with approximately αa_0 photons per cycle (where α is the fine structure constant) emitted into an angle of a_0/γ . In the nonlinear Compton regime, multiple (fundamental) laser photons are scattered into single gamma ray photons. This implies that a strong signature of nonlinear Compton scattering will be evident in the scattered spectrum.

Objectives

1. Beam dynamics due to radiation reaction. We propose to use the ELI-NP facility to observe, for the first time, the effects of radiation reaction on a laser Wakefield generated electron beam interacting with a counter-propagating intense laser pulse. Current tenable (classical) theories of radiation reaction predict that, in the ultra-relativistic regime, more energetic particles lose more energy. A beam with an initial spread of momenta will therefore cool (the relative momentum spread will decrease) as it interacts with the pulse, in addition to losing energy (Fig. 16, top). In regimes where radiation reaction is significant, it is in general not possible to ignore quantum effects on the particle dynamics. These typically act to suppress radiation reaction, reducing the overall cooling relative to the classical predictions. Semi-classical (Fig. 16, bottom) and stochastic models of radiation reaction in the weakly quantum regime instead show less beam cooling [65] or even an increase in the relative momentum spread [66], providing a signature of the transition from a continuous (classical) emission process to a strongly stochastic (quantum) regime. By stretching or compressing the laser pulse, the total effect can be made more or less like the classical prediction (Fig. 15), and this transition will be studied [65].

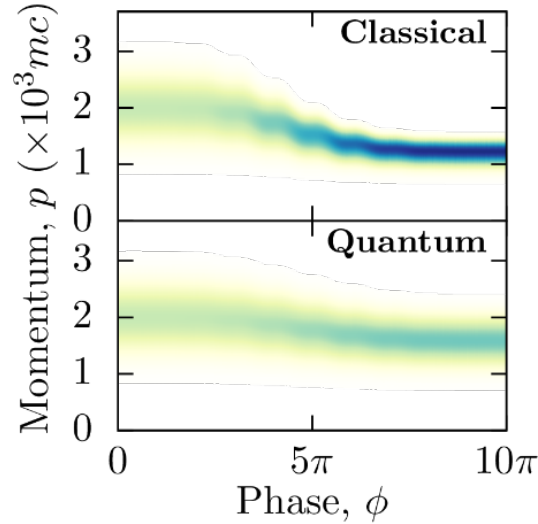


Fig. 16 – Relative momentum spread of a 1 GeV electron beam interacting with an $I = 8 \times 10^{21} \text{ Wcm}^{-2}$ laser pulse of FWHM duration 7 fs cools from 20% to (top) 12.5% in the classical Landau-Lifshitz theory, or (bottom) 18% according to a semi-classical treatment. Figure reproduced with permission [65].

We will use a first laser to generate a high energy electron beam via laser wakefield acceleration. This beam will be collided with a second counter-propagating laser pulse, and the total energy and momentum spread will then be measured. For a 1 GeV electron beam with 20% initial momentum spread, collision with a 27 fs pulse of intensity $2 \times 10^{21} \text{ Wcm}^{-2}$ would reduce the spread to 12.5% (in the classical theory) or 16.6% (in the semi-classical theory). This provides a direct way of comparing experimental results with predictions of the classical, semi-classical and stochastic theories of radiation reaction.

2. Observation and signature of nonlinear Compton scattering. This may be observed using a relatively low intensity laser pulse, with a_0 in the range of 1-10. The advantage offered by ELI-NP is that such pulses may be produced without tightly focusing the beam, which both allows the laser to be treated as a plane wave and extends the interaction time. The radiation emitted from an electron bunch of energy of approximately 10 MeV colliding almost head-on with such a laser should yield a clear signature of the intensity dependent mass shift of the electrons in the presence of the laser field [67].

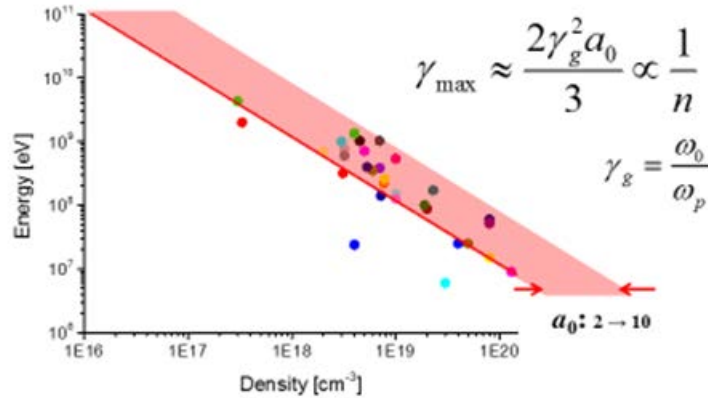


Fig. 17 – Maximum electron energy as a function of plasma density for initial a_0 between 2 and 10. Dots represent maximum energies from current experiments.

3. Development of a (resonant) betatron gamma-ray source. The LWFA can also be used directly as an intense betatron gamma ray source with a peak brilliance exceeding that of 3rd generation synchrotron sources but in a photon energy range up to 20 MeV and photon numbers in excess of 10^9 - 10^{10} per shot, with high transverse coherence [68, 69]. It is envisaged that this source will be used for RR studies, nonlinear Compton scattering, nuclear physics and QED studies. Pulse durations of several attoseconds or shorter should be feasible with development, and in-situ experiments where laser beams collide inside the accelerating structure should be possible, thus simplifying alignment for complex experiments.

Laser, target and diagnostic requirements

Two nearly counter-propagating 10 PW laser beams will be required. In the initial stages, a small fraction of one of the 10 PW laser beams will be focused into a gas cell or pre-formed plasma waveguide to accelerate electrons in a LWFA to energies of around 1 GeV. Plasma densities of around $1 \times 10^{18} \text{ cm}^{-3}$ will be utilized in the next stage. As seen from Fig. 17, the maximum energy can be increased simply by decreasing the plasma density. Recent experiments have demonstrated more than 4 GeV electron beams [70]. The second stage of the experiment will utilize a larger fraction of the 10 PW pump beam to increase the electron beam energy to 5 GeV. The f-number of the pump focusing optics and the pump pulse duration will be adjusted to optimize the coupling to the plasma bubble when the electron beam energy is varied. The overall length of the LWFA will be between 5 mm and around 10 cm.

The collision point between the electron beam and the counter-propagating focused laser beam will be chosen to be as close to the LWFA accelerator as possible to ensure that the electron beam cross-section matches the focused laser beam.

2.2.1.3 Precision measurements of the interaction of intense lasers with relativistic electrons and signatures of the quantum regime of radiation reaction

Precision measurements of the interaction of intense lasers with relativistic electrons and signatures of the quantum regime of radiation reaction.

In the quantum regime of radiation reaction, even the trajectory of a free electron can no longer be described by classical physics. Measurements of the trajectories and energy loss due to radiation reaction in the quantum regime will provide the first observations of non-classical trajectories under these extreme conditions.

The field radiated by an accelerated particle results in a force acting back on that particle and therefore affects the trajectory of the particle itself. In classical electrodynamics, this effect is described by the Lorentz-Abraham-Dirac equation (LAD). Solving this equation fully is challenging and can lead to unphysical ‘runaway’ solutions, whereby the electron is continuously accelerated by its self-radiated field. In the limit where the energy of the radiated photons remains small compared to the energy of the electron, iterative solutions based on a perturbative approach such as the Landau-Lifshitz (LL) approximation are possible. However, when the field strength in the rest frame of the electron approaches the Schwinger field ($\chi \sim 1$), the emitted photon energy becomes large and necessitates a full quantum treatment to accurately describe the electron’s dynamics. Recent work highlight that for ($\chi \sim 1$) the quantum prediction deviates significantly from the classical prediction in terms of particle trajectories, emitted photon spectrum and ultimately, final energy. Fig. 18 compares the angular scattering predicted when χ approaches unity for the polarization plane for a linearly-polarized beam interacting with a relativistic electron. The LL approximation predicts that the deflection is essentially the same in both planes and dominated by the ponderomotive force of the laser. In contrast, the full quantum treatment shows a substantially broadened angular distribution in the polarization plane while the perpendicular plane shows little deviation from the classical LL prediction.

This asymmetry provides an unambiguous experimental signature for the onset of quantum regime of radiation reaction and is easily within the angular resolution limits of the planned detection system (0.1 mrad). Distinct differences are also predicted in the energy loss of the electron and the Compton photon spectrum during such processes.

The fundamental change in the behavior of the electron’s trajectory from the classical description to the quantum description derives from the stochastic nature of photon emission in the quantum picture. In the classical description, the emission of

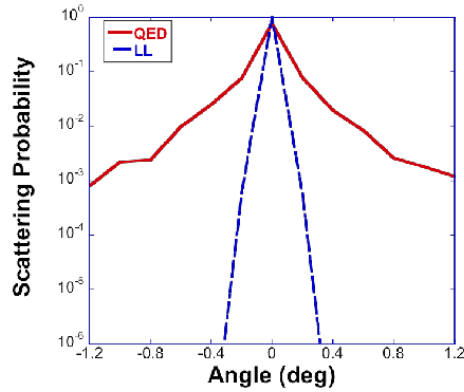


Fig. 18 – Predicted scattering signature of electrons scattering in the polarization plane of the laser in quantum regime (denoted QED) and the classical limit (denoted LL) for $\chi = 0.2$ and $\gamma = 2500$ [74].

photons is described as a continuous process, resulting in a continuous, deterministic force deflecting the electrons away from regions of high laser field strengths. By contrast, the full quantum description predicts that a significant fraction of electrons do not undergo significant deflection in the rising edge of the laser field and can propagate into the regions of highest field, where they have a high probability of emitting high energy γ -rays and undergoing significant deflection.

Experimental Signature and Count Rates: The experimental signature will be the production of wide angle scattered electrons. For an 100 pC electron bunch, the laser will be interacting with approximately 10^7 electrons, resulting in 10^6 scattered electrons at large angles. Combining energy resolution in a spectrometer with excellent spatial resolution in the detector will provide a strong signal with excellent signal to noise ratio on a single shot basis. Additionally, fine measurements of the spectrum of the scattered electrons, and of the generated gamma-rays will provide further experimental data of radiation reaction in a fully quantum regime [55, 59, 71–73].

Required Laser pulse parameters and characterization: Initial experiments require the demonstration of a stable electron beam with energy of 1-2 GeV. This is a common requirement of many experiments and requires power above 1 PW, intensity exceeding 10^{19} Wcm⁻², f-number = f/40-f/60 (apodized beam). The focus position of the 10 m parabola should be movable between chamber center and the chamber entrance wall for best scientific exploitation. In addition, the short focal length experiments require beam intensities of 10^{21} - 10^{22} Wcm⁻² and circular polarization will be useful to test theory, but not required for initial experiments.

Laser diagnostics requirements: Characterization of the laser focal spot at low power, energy distribution and chromatic aberrations are needed to calculate the

peak intensity. Femtosecond synchronization system on target using frequency domain interferometer requires optical tables in the area, optical windows on chambers. A synchronized probe beam would be of great assistance in optimizing electron acceleration. Shot-to-shot pulse diagnostics in laser bay are essential (at least far field, near-field, pulse duration) together with focal spot diagnostics and wavefront sensor in the interaction chamber and spectrometer to characterize the transmitted laser light.

Diagnostics: Target alignment microscopes in chamber; Movable electron spectrometer optimized for 1-3 GeV; Shielded reaction product spectrometer for electrons/positrons with vacuum propagation pipe (25-50 mm diameter if external to chamber); Gamma-ray calorimeter; Magnet spectrometers; Spectrometer shielding (ideally integrated into beam dump).

Target Requirements: Gas cell for electron acceleration with x - y - z manipulator.

2.2.1.4 Controlled Electron beams for fundamental science ELI-NP

Electron Acceleration using high energy femtosecond laser pulses in laser driven plasma wakefields is a well understood phenomenon and these electron beams in the few GeV limit optimize for $f/20$ focusing for powers of only a few 100 TW. For stable acceleration as to a few GeV electron source for QED studies the community will be ideally served by apodizing the 10 PW beam with capability as far down as 30% of nominal beam diameter with $f/60$ and 1 PW peak power. The added advantage of such a beam is that it will have excellent focusing properties if properly done. This requires the incorporation of a vacuum spatial filter with serrated apertures in the laser system. This is a standard procedure (*e.g.* Omega, Vulcan, Gemini, Taranis, etc.) and will greatly enhance the science output of the facility.

Required Laser pulse parameters and characterization: For electron energy approaching 1-2 GeV we require power larger than 1 PW, intensity above 10^{19} Wcm⁻² and f-number between $f/40$ - $f/60$ (apodized beam).

Laser diagnostics requirements: Characterization of laser focal spot at low power, energy distribution and chromatic aberrations needed to calculate the peak intensity. Synchronized probe beam would be of great assistance in optimizing electron acceleration. Shot-to-shot pulse diagnostics in laser bay are essential (far-field, near-field and pulse duration) together with focal spot diagnostics, wavefront sensor in chamber and spectrometer to characterize transmitted laser light.

Diagnostics: Target alignment microscopes in chamber and movable electron spectrometer optimized for 1-3 GeV.

Target Requirements: Gas cell for electron acceleration with x - y - z manipulator.

2.3 QED in Vacuum with two 10 PW Pump-Probe Laser Beams

2.3.1 Probing the Pair Creation from the Vacuum in the Focus of Strong Electrical Fields with a High Energy γ -Beam

The equivalence of mass and energy $E = mc^2$ is one of the central tenets of modern physics. To date, extensive experimental proves of conversion of matter into energy has been provided, but no clear experimental evidence of the reverse process, namely the conversion of pure energy into matter, has been obtained. In this respect, one of the most iconic phenomena predicted by Quantum Electrodynamics (QED) is the creation of particle-antiparticle pairs during the interaction of photons in a pure vacuum. This phenomenon is made possible by the photo-induced direct polarization of the Dirac Sea, which effectively acts as a catalyzer for the photon-photon scattering process. The state-of-the-art characteristics of the ELI-NP lasers allow, for the first time, triggering this process in the laboratory. The generation of matter from pure energy would not only represent a fascinating success of experimental physics, likely to excite the interest of the layman as well as the more-academically minded, but will also provide ground-breaking experimental data in the realm of non-linear QED.

The conversion of pure field energy to mass is fundamental to our understanding of the interaction of fields, matter and vacuum.

We propose here to exploit the collision between an ultra-high energy gamma-ray beam (energy per photon exceeding the GeV) and a high-intensity laser beam (a_0

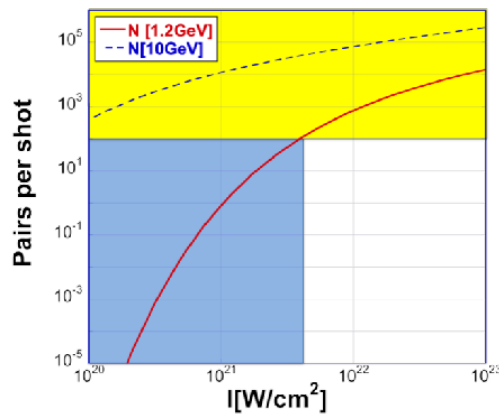


Fig. 19 – Theoretically predicted number of electron-positron pairs generated during the interaction of a high-energy gamma-ray beam with a high-intensity focus of a laser beam, in a parameter range of direct applicability to ELI-NP. Even for conservative laser intensity of $5 \times 10^{21} \text{ Wcm}^{-2}$ and gamma-ray energy of 1.2 GeV, approximately 100 pairs per shot can be generated (based on [76]).

larger than 20), both beams well within the capability of ELI-NP. In this configuration, electron-positron pairs are produced via the multi-photon Breit-Wheeler process in the tunneling regime, resulting in a test of the exponential suppression predicted by non-perturbative QED. The necessary γ -ray beam will be produced by bremsstrahlung from laser-accelerated electrons, following propagation through a thin, high-Z solid, with an endpoint energy of 1-4 GeV. GeV beams have been widely demonstrated with powers in the range of few 100 TW and beam energies of 10s of GeV anticipated for the PW at ELI-NP. At 3 GeV, the number N of optical photons with $\lambda = 800$ nm required to for the multi-photon Breit-Wheeler interaction can be estimated from $(h\nu_\gamma N h\nu_{opt}) > 2m_e c$ as $N = 200$, whereby ν_γ (ν_{opt}) is the gamma-ray (laser) photon frequency. Since the probability of coupling N photons scales as the laser strength parameter a_0 , the probability for a 1 GeV photon to create a pair becomes unity at values above 10^{22} Wcm $^{-2}$. This suggests that this regime is well within reach for ELI-NP, leading to copious pair production. While the signal level is easily detected in principle, care is required to prevent unwanted background from the gamma-ray beam - a challenge that has been met with the recent detector development at HI Jena, which will be fielded during the experiment. Accurate measurements are thus also possible in the theoretically relevant regime of exponential suppression for $a < N$ with high-repetition rate systems such as JETI at the HI Jena. Calculations show that for realistic gamma-ray beams (10^8 bremsstrahlung photons) and a focused intensities exceeding 10^{21} Wcm $^{-2}$, 10 up to 10^4 pairs can be created per shot allowing for precision measurements in the non-perturbative pair production regime over the period of a full experiment. While the signal level is in principle easily measured, the challenge is the discriminating against the γ -ray background. The Helmholtz Institute Jena has validated a detector design with sufficient angular (mrad) and temporal (picosecond) discrimination to make the experiment feasible on this critical point.

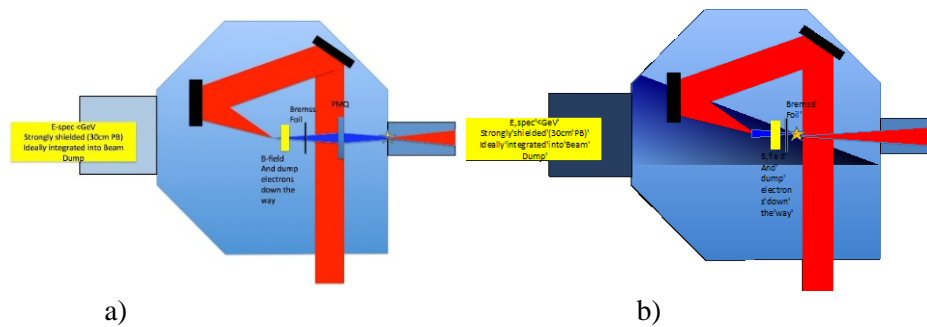


Fig. 20 – Setup with and without PMQ. While the PMQ arrangement is advantageous in terms of the experiment it requires more flexibility of the 10 m parabola positioning.

Experimental Signature and Count Rates. The experimental signature will be the production of correlated pairs of electrons and positrons from the laser interaction with a gamma ray. Single electrons and positrons can be detected with our detector system and scatter will be suppressed. Count rates are predicted in the range of 10^2 to 10^6 per hour. Coincidence detection and signal level discrimination will allow essentially background free detection of pairs.

Feasibility and Experimental Design. A sketch of two possible experimental configurations in the E6 chamber are shown in Fig. 20. In both cases, the long focal length parabola will be focused at the edge of a gas-cell target to produce a high-energy electron beam (expected energies per electron exceeding the GeV). Sketch b) shows the experiment in the traditional configuration of E6, *i.e.* with the focus of the long-focal length parabola in the center of the chamber. An alternative is shown in sketch a) whereby the focus is moved to the edge of the chamber in order to allow for the insertion of a permanent quadrupole magnet (PMQ) in the electron beam path. Refocusing the electrons will allow for an increased number of gamma-ray photons interacting with the tight focus of the high intensity laser, thus effectively further increasing the number of generated electron-positron pairs. While this latter configuration is advisable in order to optimize the signal, it must be stressed here that the experiment will still provide an amply detectable signal in its original configuration. The electron beam will then interact with a high-Z thin solid target in order to generate a bright and high-energy beam of gamma-rays via bremsstrahlung. A strong magnet will then be placed just after the solid foil, in order to get rid of all the secondary particles generated in the solid target. The second laser beam will then be focused, using a fast-focusing parabola, on the gamma-ray beam, producing the conditions for photon-photon production of electron positron pairs. The gamma-ray beam will be spectrally resolved yielding a quantitative measurement of the yield of gamma-ray photons and their spectrum, using specific gamma-ray spectrometers developed by the group in the Queen's University of Belfast [72, 75]. Fine synchronization and overlap of the two laser beams will be obtained using optical techniques designed and successfully tested by the group at the Queen's University of Belfast [55, 73]. A strong permanent magnet will then separate the electrons and positrons allowing for coincidence detection of both particles, a strong indication of pairs produced in the interaction region. Specific single-particle detectors, developed by Queen's University Belfast and Jena, will be fielded, allowing for an ultra-high level of signal-to-noise ratio.

The experimental set-up can be fully validated by replacing the laser-gamma interaction with a thin foil to produce pairs in the field of the nucleus.

Required Laser pulse parameters and characterization: Initial experiments require the demonstration of a stable electron beam with energies in the range of 1-2 GeV. This is a common requirement of many experiments and requires power larger than 1 PW, intensity above 10^{19} Wcm⁻² and f-number = f/40-f/60 (apodized beam). The focal position of the 10 m parabola should be movable between chamber

center and the chamber entrance wall for best scientific exploitation. Short focal length is needed to reach intensities of 10^{21} - 10^{22} Wcm^{-2} . The circular polarization will be useful to test the theory, but not required for initial experiments.

Laser diagnostics requirements: The characterization of the laser focal spot at low power and energy distribution are needed to calculate the peak intensity. Femtosecond synchronization system on target using frequency domain interferometer requires optical tables in the area and optical windows on chambers. Synchronized probe beam would be of great assistance in optimizing electron acceleration. Shot-to-shot pulse diagnostics in laser bay are essential. Focal spot diagnostics and wavefront sensor in chamber are required together with a spectrometer to characterize transmitted laser light.

Diagnostics: Target alignment microscopes in chamber, movable electron spectrometer optimized for 1-3 GeV, shielded reaction product spectrometer for electrons/positrons with vacuum propagation pipe (25-50 mm diameter if external to chamber), gamma-ray calorimeter, magnet spectrometers, spectrometer shielding (ideally integrated into beam-dump as shown in Fig. 21) and single electron detector.

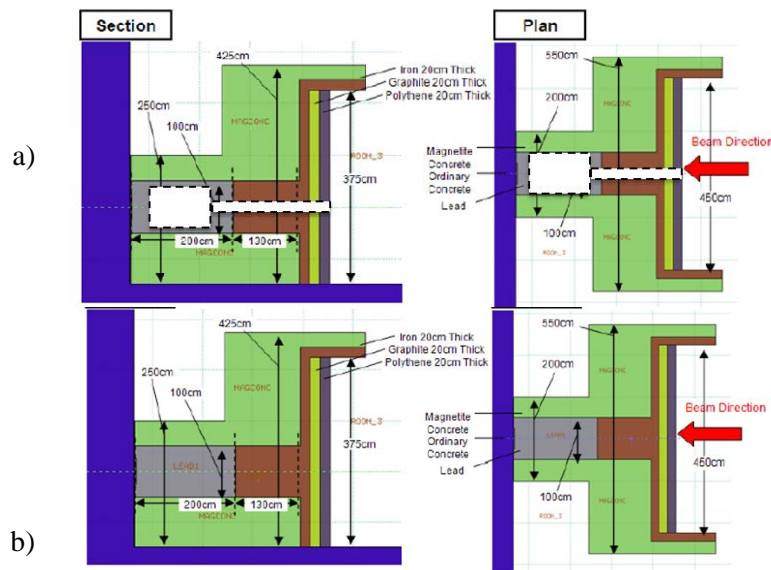


Fig. 21 – The E6 beam-dump dimension and composition assumed by NT in radioprotection calculations [101, 102]. The dual purpose beam-dump stops both multi-GeV electrons as well as multi-100 MeV protons. B) shows the modular design to allow a highly shielded cavity to be formed within the beam dump for precision measurements with e-beam energies below 3 GeV. The e-beam will be deflected by magnets into the lower part of the dump. Modular construction of the dump will allow the dump to be reconfigured depending on requirements.

Target Requirements: Gas cell for electron acceleration with x - y - z manipulator and Bremsstrahlung conversion target with x - y - z manipulator.

2.3.2 Quantum reflection (QR) at multi-Petawatt laser facilities – reflecting light from light

In contrast to classical electrodynamics, where the vacuum is entirely passive, the quantum vacuum is predicted to be an active medium with a non-linear response to ultra-intense lasers [77]. Quantum reflection [78] occurs when such lasers modify the quantum vacuum such that an effective potential is established. This results in measurable photon reflection for a probe laser and presents the first opportunity to investigate all-optical nonlinearities of the quantum vacuum.

In QED the quantum vacuum is permeated by particle/antiparticle fluctuations and virtual photons, which can couple to real electromagnetic fields or matter. This coupling allows the vacuum fluctuations to be probed directly. The interaction of vacuum fluctuations with external fields leads to phenomena such as vacuum birefringence, photon splitting and light-by-light scattering [79]. An intriguing recent prediction is that of quantum reflectivity [78], which emphasizes that the application of a strong field induces a nonlinear response in the vacuum. The induced potential results in a non-zero optical reflectivity resulting in a measureable signal in conjunction with the advanced detection techniques developed under objective B1. Recent theoretical work at the HI Jena [78] predicts that reflection coefficients as high as 3×10^{-18} for the parameters of ELI-Beamlines or ELI-NP (10 PW). Assuming a probe beam (either fundamental or second harmonic if required for background rejection), containing 10^{20} - 10^{21} photons (15-150 J, well within the design parameters of ELI- NP), between 300-3000 scattered photons are predicted per shot for peak intensities of 10^{22} - 10^{23} Wcm⁻². For ELI-NP conditions the parameter $\zeta = \tau_{pulse}/z_R \sim 1$, resulting in approximately 10^5 scattered photons per hour. The Reflectivity scales with I^2 , thus scattered 10^3 scattered photons are expected at 10^{22} Wcm⁻².

Experimental Signature and Count Rates. The experimental signature will be scattered photons from UHV vacuum in a laser-laser interaction. The detection system capable of measuring single photons will be fully tested at the JETI laser facility at Helmholtz Institute Jena to ensure background free detection of single photons. It is designed to have a noise floor of approximately 10^4 photons per shot

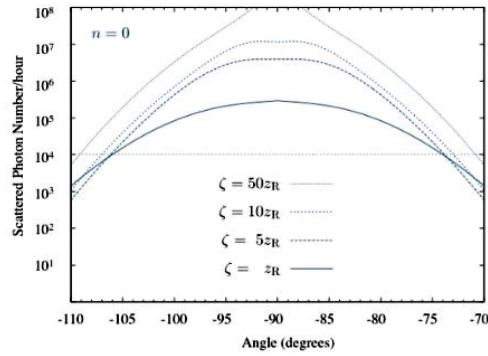


Fig. 22 – Number of quantum reflected photons for an $f/3$ parabola focused to 10^{23} Wcm^{-2} per hour.

ensuring a signal to noise ratio of $10^7 - 10^9$. Suppression of inevitable scattered light will be by a combination of polarization, diffraction limited angular selection and temporal resolution. A synchronized fs laser will be required to drive the gating system, which allows the integrated volume to which the scattering detector is sensitive to be reduced to approximately $10^4 \mu\text{m}^3$, thus suppressing unwanted scattered components by aggressive spatio-temporal filtering.

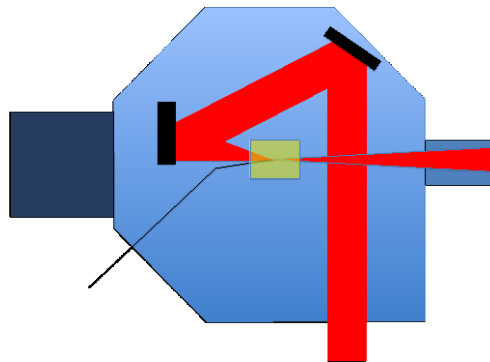


Fig. 23 – Schematic Layout of the proposed experiment. The black line indicates the direction of scattered light collection. The Shaded interaction region indicates the UHV differentially pumped sub-chamber.

Feasibility. The envisaged setup is thus relatively simple, if we consider that the only effective target to be used for the ELI-NP laser beams is vacuum itself. In

its basic configuration, the two beams will be focused by fast-focusing parabolas onto the same position in the center of the E6 chamber. Overlap and synchronization optical diagnostics, already successfully tested by our group [55, 73], will allow for micron-scale and femtosecond-scale precision. Depending on the capability of splitting beams in the E6 chamber, the possibility of using three beams can also be envisaged, following a recent theoretical work in the subject [79]. Even though this would likely enhance the signal-to-noise ratio, it must be stressed here that it is not strictly necessary for the success of the experiment.

Required Laser pulse parameters and characterization: $f/20$ and $f/3$ optics. Strehl ratios from 0.25 upwards are desired. The focal positions of the focusing mirrors will coincide. Circular polarization will be useful to test the theory, but not required for initial experiments.

Laser diagnostics requirements: Characterization of laser focal spot at low power, energy distribution and chromatic aberrations are needed to calculate the peak intensity. Femtosecond synchronization system on target using frequency domain interferometer requires optical tables in the area, optical windows on chambers. Synchronized probe beam to drive time gated photon detector. Shot-to-shot pulse diagnostics in laser bay are essential. Focal spot diagnostics and wavefront sensor in chamber. Optics tables for time gated set-up. Prepulse capability on $f/20$ line would be desirable ($1e^{-4}$ at larger than few ns).

Diagnostics: Single photon detector and laser diagnostics.

Target Requirements: Separate ultra-high-vacuum chamber must be integrated into chamber.

2.4 Atoms in Extreme Fields: Relativistic Tunneling Ionization and Particle Acceleration

The main objective of the commissioning run is to observe high energy (GeV) electrons produced during ultra-relativistic tunneling ionization from hydrogen-like heavy ions (like Ar^{17+}). These electrons have a correlated angular-spectral distribution that distinguishes them from, say electrons accelerated in a wake-field, and which carries with it information about the extreme tunneling ionization process and subsequent electron dynamics. In the extreme light regime, the photoelectron spectrum takes on new characteristics, resulting from the possibility particles staying in phase with the optical wave. Achieving this “phase resonance” condition requires exposing matter to the highest fields that can be achieved in the laboratory. The ELI-NP 10 PW laser, expected to come online in a few years, is an obvious candidate for producing such fields. Tunneling ionization of inner shell electrons occurs only in an extreme field. For example, using a simple barrier suppression model, it is estimated that argon can be fully stripped by an irradiance of approximately 10^{22} Wcm^{-2} . Although similar irradiance has been reported [80], difficulties with

maintaining the vacuum spot size on-target have prevented observation of, say, fully laser-stripped Argon. We will observe extreme field tunneling, for the first time, through the use of novel gas targets that provide inherent focusing and are insensitive to pre-pulses and pointing errors.

Computational support for this effort will include our recently developed general purpose computing on graphics processing units (GPGPU)-enabled suite of models [81, 82]. The first model [81] computes the full quantum mechanical, relativistic charge distribution of a tunnel-ionized electron. Due to computational limitations, this has to be supplemented by the second model [82], which tracks classical trajectories through the entire laser confocal region, accounting for radiation reaction. Hydrodynamics and particle-in-cell models are also available for modeling gas target formation and laser propagation through plasma.

Background: During the past two decades, advances in high power ultra-short pulse lasers have allowed for the investigation of phenomena that are highly nonlinear and relativistic. Advanced particle-in-cell (PIC) codes have proven to be accurate models for such diverse phenomena as nonlinear wake formation, laser acceleration of particles, and various forms of radiation generation [83]. Experimental successes include laser wakefield acceleration of electrons to GeV energies [84], and generation of 0.5 GeV ions from solid targets [85]. A paradigm shift may be imminent as a result of efforts to develop 10 petawatt, or even exawatt, scale systems (*e.g.* VULCAN at RAL in the UK, APOLLON at ILE in France, XCELS in Russia, or ELI-NP in Romania). These efforts raise the possibility of bringing to the laboratory irradiances where novel effects such as radiation reaction (RR) or vacuum polarization become observable.

It is likely that the regime of RR, and especially vacuum polarization, will not be accessible to experiments for several years. However, existing lasers can access a regime where unresolved issues still remain, particularly in connection with relativistic ionization physics. These issues include the nature of the relativistic photoelectron spectrum, the role of ion dynamics, the nature of high-harmonic generation (HHG), and the role of nonlinear Compton scattering. Most of the photoelectron spectra that have been observed over the years are connected with an interest in above threshold ionization (ATI), and are produced in the non-relativistic regime [86, 87]. In the weakly to moderately relativistic case, some of the most important studies were carried out at the Naval Research Laboratory [88, 89]. The correlation between the energy and angle of the photoelectrons was identified as a defining characteristic. However, it was found that while the correlation between polar angle and energy was consistent with theory, the azimuthal distribution was not as expected. Furthermore, in the ultra-relativistic case, the scaling of energy with irradiance has not been firmly established. In terms of HHG, it has been argued that in the relativistic case, re-collision is not possible, and therefore the conventional HHG mechanism is absent. However, this claim actually depends on knowing the relativistic quantum mechanical charge distribution during the ionization process,

which, to our knowledge, has never been rigorously calculated. Finally, when photoelectrons are released into an extreme field, nonlinear Compton scattering and RR may accompany the process. The observation of RR would contribute to the resolution of difficulties going back more than 100 years.

Description of Proposed Commissioning Run: The highest irradiance produced by a laser to date, $2 \times 10^{22} \text{ Wcm}^{-2}$ [80], occurs only in vacuum. The proposed program seeks to apply a similar irradiance to moderate or high Z atoms. The experimental observables include photoelectron distributions, ion charge states, and scattered radiation. Novel gas target configurations will be employed to overcome technical problems involving pre-pulse, plasma defocusing, and charged particle statistics.

The theoretical program will also be groundbreaking, delivering what will be, to our knowledge, the first ab initio relativistic tunneling ionization calculations at full scale. The theoretical program will also provide guidance on the dynamics of the laser pulse in the gas target via three dimensional (3D) particle-in-cell (PIC) simulations, and also on the formation of the gas target itself via 3D hydrodynamics and computational fluid dynamics.

A suitable candidate for an experimental observable is the unique electron distribution (angle and energy) resulting from Laser Ionization and Ponderomotive Acceleration (LIPA).

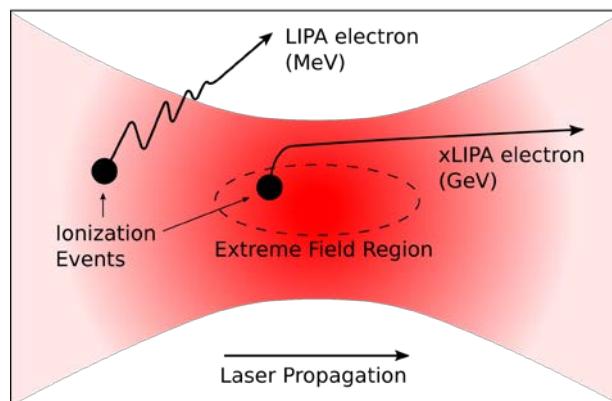


Fig. 24 – Schematic of LIPA and xLIPA processes. The density at best focus should be kept low enough so that plasma effects do not alter the electron dynamics.

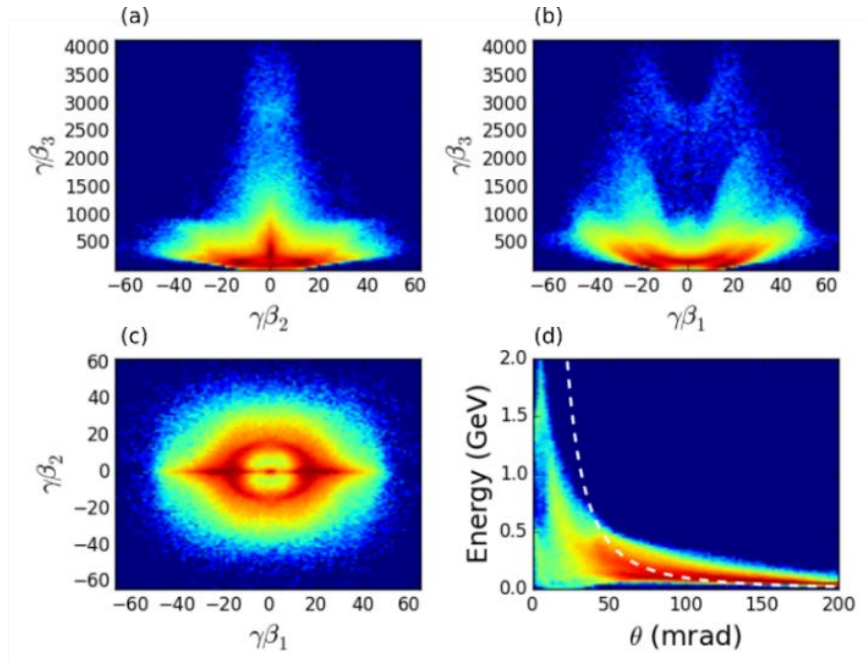


Fig. 25 – Momentum distribution due to the K-shell electrons in argon, in various 2D projections. The direction subscripts 1, 2, and 3 refer to the polarization, cross-polarization, and propagation directions, respectively.

The principle of LIPA is that vacuum acceleration is possible when a free electron is abruptly introduced into the high field region associated with a laser focus [82, 88]. Such is the case when inner shell atomic electrons are tunnel ionized by a laser. A simple minded estimate of the highest energy obtained from the LIPA mechanism is $\gamma^2 \approx 1 + a^2$, where a is the normalized vector potential in the region where the particle is ionized. The actual energy is in fact much higher at extreme irradiance, due to a mechanism we refer to as xLIPA. In the xLIPA scenario, ionized electrons are accelerated so abruptly, they are captured by the optical wave and stay in phase for a long time. The energy still scales with a , but with a large coefficient, such that the ELI-NP laser could achieve nearly 2 GeV acceleration in free space. The momentum distribution generated from a uniform background of helium or hydrogen-like argon ions is in Fig. 25.

Ab initio numerical models of relativistic tunneling are challenging due to the large scale separation (5-6 orders of magnitude) between the fundamental QED time-scale, \hbar/mc^2 , and the optical period of a petawatt-class laser system. We have developed a numerical solution of the Klein-Gordon and Dirac equations for a relativistic spin-zero particle exposed to an arbitrary binding potential and laser field

that takes advantage of both massively parallel processing (MPP) and general-purpose graphical processing units (GPGPU) [81].

An example of a calculation made using the pure MPP version of the code is shown in Fig. 26. The GPGPU enabled version is documented in [81]. By utilizing large-scale GPGPU clusters we are able to carry out a relativistic tunneling calculation at full scale for the first time. These quantum calculations will provide inputs for the classical particle tracking code that predicts the primary observable, the photoelectron angular-spectral distribution.

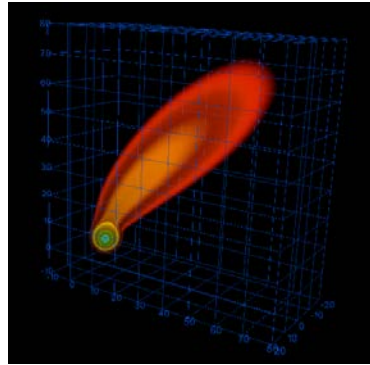


Fig. 26 – Fully relativistic 3D calculation of the quantum charge distribution during tunneling ionization of hydrogen-like argon ($Z=18$) by a few-cycle pulse of 50 eV photons with $eA/mc^2 = 0.3$. Horizontal is the propagation direction, and vertical is the polarization direction. The quantum analog of the ponderomotive force is visible as the displacement of the charge in the horizontal direction. The axis units are in Compton wavelengths

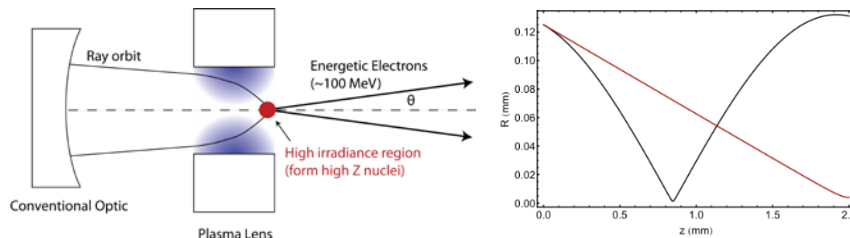


Fig. 27 – Plasma lens as a target. Left: Schematic. The scale of the plasma lens is highly exaggerated. The electron distribution in angle and energy is closely related to the ionization physics. Right: Spot size radius vs. position in the plasma lens. The black curve is the spot size in the presence of the plasma lens, and the red curve is the spot size in vacuum. Note that in a uniform gas, the waist radius would be larger than in the vacuum case, due to ionization defocusing.

The experimental run will focus on measuring photoelectron distributions, although ion charge states and radiation spectra could also be interesting to measure. In order to overcome experimental difficulties associated with pre-pulse and plasma

de-focusing, we propose to use a plasma lens [90–92] as a target. A plasma lens is a short plasma channel [93] with an on-axis density minimum that tends to focus radiation. It is stripped of its weakly bound electrons before the petawatt pulse (or pre-pulse) arrives, thereby reducing the effects of ionization defocusing, and even providing additional focusing beyond that of the final conventional optic. The lens can be produced, *e.g.* by focusing a heater beam into a gas jet. A schematic of the proposed configuration is shown in Fig. 27. Using a conventional optic, a high power laser pulse is focused into a plasma lens. The geometric focus is positioned somewhere beyond the plasma lens, such that the actual focus occurs in the rarified region near the back of the lens. Focusing into a rarified region minimizes plasma effects. As part of the program, we will evaluate the impact of nonlinear effects that develop on the way to the best focus [94]. For the present, we plot the results of a linear calculation [95] in Fig. 27. The plasma lens reduces the 4 micron vacuum waist radius to 1.3 microns. Furthermore, ionization defocusing is suppressed because the plasma lens is already composed of high charge state ions. More complete nonlinear calculations have indicated that the irradiance with the plasma lens can actually be larger than without it, due to nonlinear short pulse effects. However, the lens may still be useful for producing a target favorable for xLIPA, which benefits from a high density of off-axis ions, and for suppressing deleterious pre-pulse effects

Finally, we suggest an electron diagnostic configuration, and provide some estimates of the expected signal. We are attempting to count electrons that fall within an angular and spectral band. In the proposed experiment, angle and energy are correlated (see Fig. 25 d). The proposed setup would situate a dipole magnet and scintillator screen (or other counter) downstream of the laser focus. We estimate that the interaction volume will be 10^{-13} m^3 , with about 10^9 inner shell electrons available for acceleration. Collecting within a cone angle of 10 milliradians keeps about 0.6% of the electrons. The spectrum of these electrons is shown in Fig. 29. Of these about half go into a 250 MeV population, and the other half are found in a 1.5 GeV population. In the experiment, one would expect to collect a total of 10^7 electrons per shot within the given cone angle.

The setup displayed in Fig. 29 is a refinement where the LIPA angle is observed along the axis out of the page while energy is resolved along the scintillator axis in the plane of the page. This should work if the dipole magnet can be designed to image in the horizontal plane while leaving the vertical unaffected. In this way, the energy-angle correlation can be observed in a single shot. The fast-gated CCD camera is used to improve signal-to-noise ratio of the scintillator image.

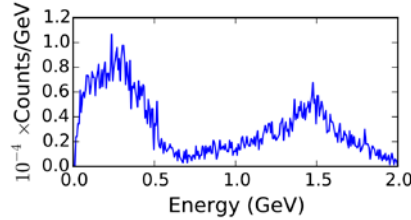


Fig. 28 – Ionized K-shell electron energy distribution after angular selection within a 0.01 radian cone. The total number of macroparticle counts was 10^6 . There are about 6400 counts collected within the cone angle (0.64%). The number of electrons collected in an experiment is estimated at approximately 10^7 .

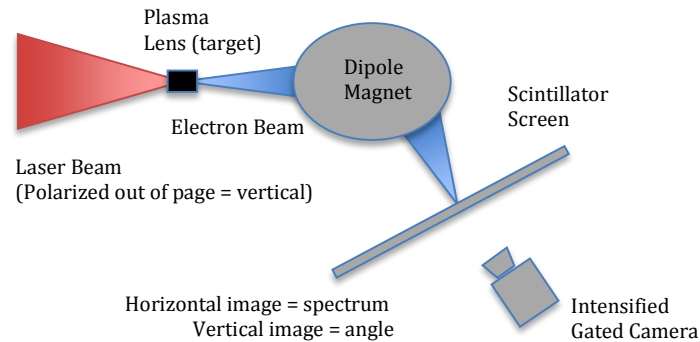


Fig. 29 – Suggested electron diagnostic allowing single-shot measurement of the LIPA energy-angle correlation.

2.5 Preliminary Commissioning runs using CETAL 1 PW Laser System

2.5.1 Compton scattering and quantum radiation reaction

Nonlinear quantum electrodynamics (NL-QED) represents one of the greatest successes of modern theoretical physics combining special relativity and quantum dynamics in an elegant and efficient manner. Albeit this theory predicts many fascinating phenomena, the energies required to stimulate them have hitherto forbidden detailed experimental validation. However, the newly built CETAL laser at the National Institute for Laser, Plasma and Radiation Physics (INFLPR), Bucharest, Romania offers the unique opportunity of pursuing this outstanding experimental goal. CETAL delivers a 28 fs-long laser pulse with a peak power exceeding 1 PW, providing the ideal experimental condition, once the beam is aptly split, of counter-propagating interaction of a GeV electron beam with the high-

intensity (larger than 10^{21} Wcm⁻²) focus of a laser beam. In this experimental configuration, an electron in such an intense electromagnetic field is expected to convert a significant part of its kinetic energy into radiation, entering a regime in which quantum signatures of radiation reaction can be detected, an absolute novelty in experimental physics. We thus propose an experimental run devoted to studying ultra-high field electron dynamics, in a regime whereby non-linear quantum signatures can be detected. The main experimental objectives of this program can be thus summarized as:

1. Laser-driven generation of high-quality, narrow-band, and stable GeV electron beams.
2. Detection of quantum effects in radiation reaction during the propagation of an electron beam through an ultra-intense electromagnetic field.
3. Generation of ultra-high energy (up to hundreds of MeV), high flux, and high-quality γ -ray beams.
4. Generation of electron-positron pairs following photon-photon collisions.

These objectives are not only at the forefront of ultra-intense laser research but their achievement would also enormously advance our understanding of fundamental physics since they will provide a first glance of quantum electrodynamics in a non-linear regime.

The research group at the Queen's University of Belfast has extensive experience in ultra-high intensity laser-matter interaction and has already experimentally demonstrated non-linear effects in counter-propagating electron beam - laser collisions. Preliminary experimental results obtained by the group at the HERCULES laser facility (Center for Ultrafast Optical Science (CUOS), Ann Arbor, Michigan US) [61, 75] and at the Astra-Gemini laser facility (Rutherford Appleton Laboratory, UK) [55, 72, 73] fully demonstrate the feasibility of performing this kind of experiments with existing laser technology.

The proposed experimental setup is sketched in Fig.31. In order to maximize the performance of the CETAL beam, we plan to split the beam using an apodized holed mirror. A serrated aperture can also be introduced in the laser amplification chain, ideally before the last amplifier. The central part of the beam will be focused by a long-focal length parabola onto the edge of a gas-cell. In the following a quick summary of how to achieve the experimental objectives will be given.

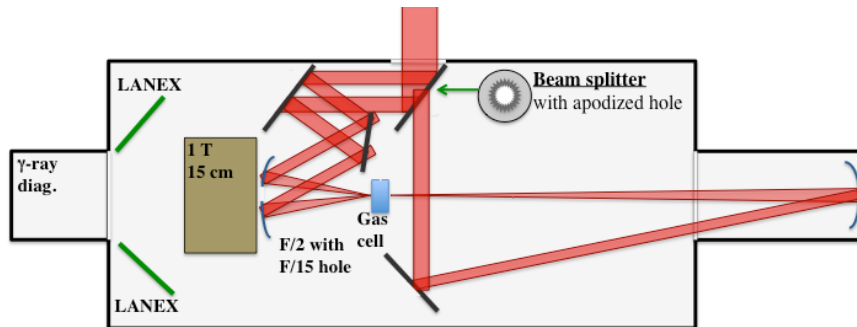


Fig. 30 – Sketch of the top-view of the experimental setup for counter-propagating electron beam – laser collision. The laser beam is split, using an apodized holed mirror into two beamlets. The central beamlet is focused by a long-focal length parabola at the edge of a gas-cell target to generate an ultra-relativistic electron beam. The rest of the annular beam is instead focused by a holed fast-focusing parabola onto the axis of the electron beam. A strong magnet after the parabola provides a spectrally resolved measurement of the scattered electron beam, whereas the Compton-generated γ -ray beam is detected at the bottom of the chamber.

1. Laser-driven generation of high-quality, narrow-band, and stable GeV electron beams. The first part of the experimental campaign will not make use of the rest of the beam, but it will only concentrate on generating high-quality and high-energy electron beams from the laser-gas interaction. Apodizing the beam has the two-fold advantage of improving the spatial quality of the laser focal spot and providing an effectively longer f -number of the parabola ($f/20$ for the full CETAL beam, $f/40$ or $f/60$ for the apodized beam), which is essential for ensuring that the laser is guided over distances greatly exceeding the laser Rayleigh range. We plan to characterize the electron beam generation in detail, in particular by studying the effect that the main laser parameters (such as energy, duration, phase-front and spectral phase, and f -number) have on the electron beam (especially on its peak energy, spectral shape, divergence, charge, and shot-to-shot pointing fluctuation).

2. Quantum effects in radiation reaction. Once this preliminary experimental campaign has been concluded, we will focus the remaining annular part of the beam with a holed fast-focusing parabola onto the electron beam axis, to provide the experimental conditions for quantum radiation reaction to occur. The hole in the parabola has the two-fold advantage of both excluding the risk of laser back-reflections and allowing for an unperturbed propagation of the scattered electron beam and the generated gamma-ray beam. For conservative laser and electron beam parameters (such as electron Lorentz factor of $\gamma_e \sim 2000$ and intensity of 10^{21} Wcm^{-2}) we expect the ratio between the laser electric field (E_L) and the

Schwinger field (E_{cr}) in the rest reference frame of the electron to be: $\chi \sim \gamma_e E_L/E_{cr} \sim 0.2$, clearly showing how quantum effects are expected to play a significant role in the interaction. These effects will be detected by both looking at the spectrum of the scattered electrons and the Compton-generated gamma-ray beam. As an example, we plot in Fig. 31 the calculated spectrum of an electron beam of initial energy of 800 MeV ($\gamma_e \sim 1600$) after interaction with a laser beam with intensity of 2×10^{20} or 10^{21} Wcm⁻². The slowed-down tail of electrons is clearly visible in the graph, providing an excellent experimental measurable for the onset of radiation reaction.

3. High-energy γ -ray beams. Quantum radiation reaction effects are expected to be detectable also in the spectrum of the Compton-generated gamma-ray beam [59]. In order to precisely detect the spectrum of ultra-high energy high-flux γ -ray beams, we will use a hydrogen-based spectrometer, which is a refinement of a Li-based detector that we have already successfully used in a previous experimental campaign [55, 72]. In its basic configuration, the spectrometer converts, via Compton scattering in the material, the γ -rays into electrons of very similar energy, whose spectrum will be recorded using a conventional magnetic spectrometer. The tight resemblance of the spectrum of the secondary electron beam with the spectrum of the initial γ -ray beam, allows the latter to be easily reconstructed (see Fig. 31).

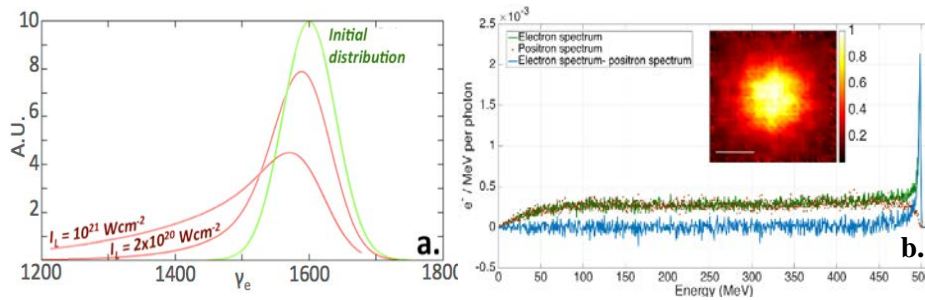


Fig. 31 – Simulated spectrum of electrons (green line) and positrons (brown dots) at the exit of a hydrogen pipe hit by a monoenergetic 500 MeV γ -ray beam. The inset shows the simulated spatial distribution of the electrons.

4. Generation of electron-positron pairs following photon-photon collisions. After the electron-laser collision experiments have been performed, we aim at studying the interaction of a bright and high-energy γ -ray beam, as resulting from the bremsstrahlung of the laser-driven electron beam propagating through a high-Z solid target with the tight focus of a laser beam. The experimental setup is practically identical to the one depicted in Fig.31 with the only differences that a tantalum solid target will be inserted soon after the gas-cell, followed by a strong magnetic field. In this case, numerical calculations indicate the generation of ultra-bright and ultra-energetic (100s of MeV per photon) γ -ray beam. In terms of

diagnostics/laboratory equipment the group will provide any equipment necessary, which include: apodized beam-splitter, $f/2$ parabola with a $f/15$ hole in the middle, gas-cell targets, γ -ray and electron beam diagnostics, optical kit for beam overlap and synchronization, scintillator (LANEX) screens and single-particle detectors.

3. TECHNICAL PROPOSAL

The requirements established by the user community are presented in the beginning of the section: the pump-probe experiments with two 10 PW laser beams and the detectors required. Next, solutions are presented: focusing configurations geometries of the two 10 PW laser beams, the interaction chamber E6 and the key diagnostics, and the multi-GeV electron spectrometer.

3.1 Requirements provided by the User Community

The user community provided the requirements for High Field Physics and QED experiment from the very start of the formal TDR process. The section presents these requirements.

3.1.1 Laser beam control and characterization: requirements

The highest possible intensity 10^{22} - 10^{23} Wcm^{-2} is needed. This requires tight focusing with short focal length $f/3$ (or shorter) off-axis parabolas. Off-axis parabolas should be mounted (for example with the incident beam onto the parabola coming from outside the horizontal plane) to provide greatest possible access around the target for diagnostics. The initial available intensity is expected to be approximately 4×10^{22} Wcm^{-2} . Initially the $f/3$ focusing mirrors will be installed.

The two synchronized 10 PW laser beams will be focused on the same target in E6 and working as pump laser beam and probe laser beam. It would provide full control of the electron acceleration by the pump-beam and also full control of the probe electro-magnetic field provided by the probe beam. This capability will make ELI-NP unique in the world. No other planned 10 PW facility, worldwide, will have two synchronized 10 PW laser beams.

The polarization control is required and should include the ability to switch between linear and circular polarization.

Ultra-high intensity contrast is needed, *e.g.* above 10^{13} at ns level and more than 10^{12} at ps level. This is required for solid targets and thin foil experiments. Plasma mirror may be required to achieve this, which in turn requires research and development effort. Temporal shaping and control of rising edge of the laser pulse would be highly beneficial.

Spatial shaping and control of focal spot distribution would be highly beneficial with the possibility to use of adaptive optics to maximize the encircled energy within the focal spot. The two 10 PW Laser beams will be transported to the appropriate target in E1, E6 and E7 interaction areas.

Debris mitigation is a potential issue due to short focal length of the focusing optics and the fact that there will potentially be up to 1,500 laser shots per week available. One example solution is suitable pellicles with minimum wave front distortion. Interchangeable optics are required in case of damage to minimize downtime (due to the long lead time for engineering a delivery of large focusing optics).

Laser diagnostics requirements: Measurements of the laser intensity and temporal contrast are required, especially on the rising edge of the laser pulse in order to avoid pre-pulses and therefore pre-plasmas. The measurement can be obtained for example with frequency resolved optical gating (FROG) diagnostic. The measurement of the laser focal spot energy distribution and the phase front is required for establishing the focused laser intensity in Wcm^{-2} . The measurement of the degree of temporal overlap (via autocorrelation) and spatial overlap of the two 10 PW foci in the target plane is required for experiments in which one 10 PW laser accelerates electrons in a solid or gas target and the second 10 PW laser subjects the electrons to powerful EM field hence generating QED effects like gamma radiation and electron-positron pairs. The synchronized optical probe laser is required to characterize the density gradients at the target front surface of the target. The near- and far-field monitoring of the laser beams is required to establish the shot-to-shot stability of the laser focus. The measurement of the laser pulse energy and spectrum is required to obtain the focused intensity and laser pulse duration at the target.

Electron beam diagnostics requirements: In order to fully characterize the laser accelerated electron bunch we require a set of standard electron diagnostics: energy spectrometer, beam profile, charge-Faraday cup, ICT and calibrated image plates, emittance measuring system-series of screens and focusing element, beam transport system, coherent transition radiation electron bunch duration measuring system.

Long focal length diagnostics requirements: Frequency-resolved optical gating (FROG), spectrometers, power meters, laser beam near-field and far-field diagnostics and alignment targets.

Plasma diagnostics for beam-beam experiments requirements: In order to fully characterize the plasma in which the electrons are accelerated we require: Thomson scattering/imaging and interferometer for plasma density measurements.

3.1.2 Target fabrication and manipulation requirements

Plasma targets for Laser Wake Field Acceleration (LWFA) source: A gas-cell or preformed plasma capillary waveguide are required for accelerating electrons by the LWFA process by the 10 PW laser focused with the long-focal length mirror. Additionally an injector gas jet will be required for counter propagating electron-laser beams. The gas cells and capillary waveguide require x - y - z - θ - ϕ adjustment to match the focus and direction of the laser beam.

Solid target fabrication requirements: Thin foils/solids and foam targets are required for efficient electron acceleration in solids. The required target fabrication techniques are well established. Cryogenic targets are potentially also suitable and possibly produce less debris, but require research and development effort to develop and implement. Fabrication on-site is required due to the delicate nature of many of the ultra-thin foils and foams. Standardized mounting of targets is required to facilitate ease of changeover between target types.

Required target handling systems: Manipulation drive systems are required, both in-chamber and outside for alignment. Accuracy positioning of 0.25 μm in x , y and z -axes and 1 mrad in angular rotation is will ensure the optimal positioning of the solid target in the focus of the 10 PW laser. The laser is focused on target with a short-focus ($f/3$) mirror. High resolution microscope optics are required in-situ within the chamber for accurate positioning of targets in the laser focus. A target alignment station with high resolution microscope optics for off-line positioning in x , y , z and θ is also required in order to position the target with respect to the target-holder device.

A target insertion and extraction device may be required, possibly involving robotics. This may be important for the handling of activated (post shot) target holders. It would also be important for reducing the down time resulting from opening the interaction chamber to air.

The target mount should be designed with debris mitigation / minimization in mind in order to minimize damage to expensive optics and diagnostics located in close proximity to the target.

The target mount should be designed to keep as much line of sight for diagnostics as possible. The target mount design must therefore take the chamber geometry (and thus positioning of bolt-on diagnostics) into consideration.

Target characterization requirements: A quality control procedure must be established for checking prior to insertion of the target to ensure that it meets the specification for the experiment and for checking the target in-situ inside the target chamber immediately prior to the laser shot. Thin foil and foam targets degrade quickly.

3.1.3 Diagnostics, detectors and data acquisition requirements

Specifications of the required diagnostics for γ -ray, electron and ion beam spectral and spatial measurements: High resolution dispersion spectrometers required for multi-GeV electrons and ions (spectral changes expected due to the onset of high-field QED processes). The high resolution is required to measure the spectral changes expected due to the onset of high-field QED processes. The energetic gamma-ray (hundreds of MeV) production by QED process will require high energy spectral measurements, and high energy spatially/angularly-resolved measurement. Low background detectors are required for measurement of positron production.

Required diagnostics of the laser-plasma interaction: Optical probing using a small portion of the main beam split off, frequency doubled and directed along the target surface will be used to characterize density gradients – this diagnostic is also listed above in the section of Laser-diagnostics. Measurement of the backscatter and absorbed laser pulse energy will provide the laser energy absorbed in the plasma. (Optical isolation is required to prevent back reflection causing damaging of laser components upstream). Nuclear activation measurement will characterize the plasma temperature.

Required detectors: The electron, ion and gamma-ray spectrometers require active detectors placed in their dispersion plane. For example high dynamic range CCD cameras to image scintillator or phosphor radiation. The active detector will reduce the downtime required for opening the interaction chamber to retrieve and measure passive detector media. All detection systems employed must be characterized for their EMP sensitivity in a high energy laser-plasma environment. Passive detectors based on dosimetry film, track detectors, imaging plate, etc. will be used in single-shot operation mode to cross reference results obtained using the active detectors.

Data acquisition systems: On-line analysis of data is required to guide decisions on the next laser shots to be taken. Data upload via a central data management system is required to enable quick extraction of data over a range of laser, plasma and beam diagnostics.

3.1.4 Lab Space and target chamber requirements

It is envisaged that area E6 will be used for dual 10 PW experiments on this topic. Target chamber must be big enough to accommodate two off-axis focusing parabolas in several defined geometries (*e.g.* orthogonal beams, two beams onto different sides of the target and two beams onto the same side – overlapped foci). The target chamber should be lined with aluminum to reduce activation. A minimum distance around the chamber of 5-6 meters is required for diagnostics, including optical table to accommodate optical probe beam and detectors. Although not an essential requirement, the experiment would benefit from also measuring the spectrum of neutrons produced via time of flight, for which a long flight path is required. The chamber should have as many window ports as possible for diagnostics, which bolt on angle flanges to enable maximum viewing direction to the target interaction point.

3.1.5 Radiation production and safety requirements

The primary activation physics occurs in the laser-irradiated target. Secondary activated samples will be used to diagnose the plasma and emitted radiation beam parameters. Shot-to-shot monitoring will be required, including monitoring of accumulated dose at given positions. Clean-up of activated debris (removable panels for minimum activation) and standing orders for activated sample handling / best practice development are needed.

3.2 Experimental Area and Interaction Chamber E6: configuration and focusing

Starting with this Section the technical descriptions of the proposed ELI-NP Experimental Area E6, Chamber, targets, detectors, and radioprotection are provided.

3.2.1 E6 Target area and Interaction Chamber

The planned High Power Laser Interaction Areas of ELI-NP are shown schematically in Fig. 32 and the Interaction Area E6 is shown in more detail in Fig. 33. The Interaction Areas in Fig. 32 are: E1 with two 10 PW lasers for Nuclear Physics with Lasers, E6 with two 10 PW lasers for High Field Physics and QED, E7 with two 10 PW lasers for Combined High Power Laser and Brilliant-Gamma-Beam experiments, E4 with two 1 PW (at 1 Hz) and E5 with two 0.1 PW lasers (at 10 Hz) for applications of secondary laser radiation in science and technology. E1 and E6

interaction areas share the same bunker with 2 m thick walls and with a length of 50 m and width of 20 m. The two 10 PW laser beams propagate from the Laser-Area in the North toward the E7 Interaction Area in the South.

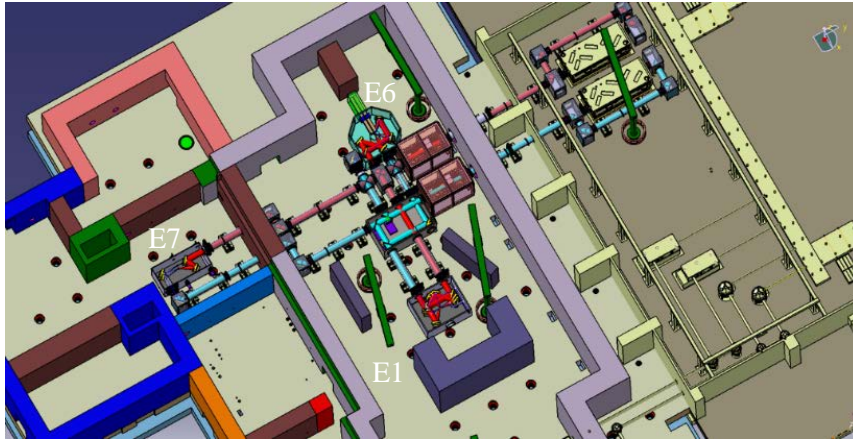


Fig. 32 – E6 Experimental Area and Interaction chamber. E6 and E1 interaction chambers share the same bunker, 50 m long and 20 m wide. E1, E6 and E7 Interaction Chambers are designed for dual 10 PW laser beam experiments. The 10 PW laser beams come through the North wall of the bunker (right side of the figure). The E6 beam-dump is on the east wall.

The Laser Beam Transport System (LBTS) also conditions initially one of the laser beams with: polarization control to change the polarization angle or provide circular polarization; adaptive optics for optimal focusing to the highest intensity; plasma mirror inside the interaction chamber in case the laser beam needs additional cleaning of the temporal prepulses, as described in ELI-NP TDR on Laser Beam Delivery [96]. The beams go through a switch-yard placed between the E1 and E6 Interaction Areas. This allows the switching of the two 10 PW laser beams between the three interaction chambers. The two 10 PW laser beams are synchronized because they are amplified starting from the same laser-oscillator. A variable delay between the two beams will be available for pump-probe experiments. The 10 PW laser pulses will have energy of 200 J/pulse, pulse duration of 20 fs and a beam diameter of 550 mm. The beam diameter is taken as 500 mm for the purpose of defining the focal length and f-number of the parabolic mirrors.

The E6 interaction chamber is almost octagonal, with the laser-plasma interaction point in the center of the chamber. The coordinates of the laser Interaction Point in E6 chamber are: 8.9 m from the West Wall and 6.2 m from North Wall of the Bunker. The Interaction Point is in the center of the chamber. The octagonal shape is similar to the Titan target chamber (TC) adopted also by Apollon/Cilex and by Vulcan-10 PW. We show as an example the proposed Vulcan-10 PW TC in Fig 35. The octagon allows diagnostics to point naturally to the plasma in the target chamber center (TCC). The inner diameter and the height of the chamber are 4.4 m

and 2.2 m respectively in order to accommodate the two-beam pump-probe focusing geometry and the large turning mirrors and toroidal focusing mirrors. The laser beams propagate in a horizontal plane at a height of 1.5 m above the floor (Fig. 35). The floor is supported on spring-loaded pillars and the scroll vacuum-pumps are in the cellar in order to reduce vibrations.

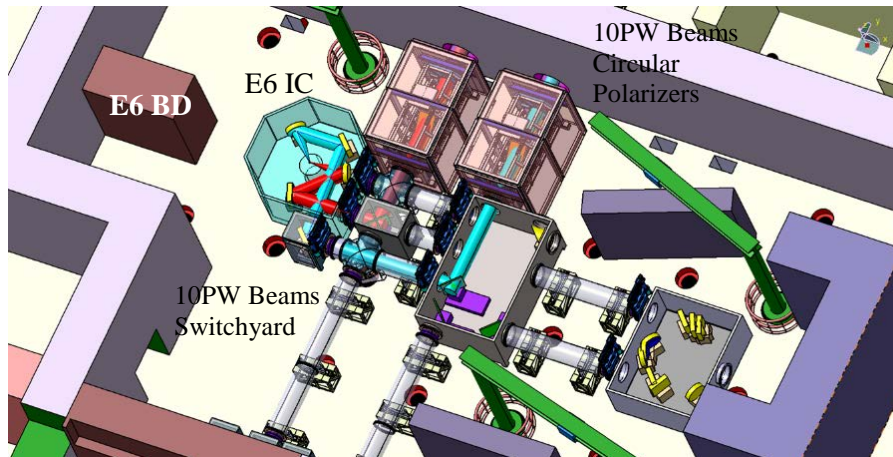


Fig. 33 – E6 Experimental Area and Interaction chamber. In this figure two 10 PW laser beams are focused with short focal length mirrors on a solid target. E6 BD is the Beam-Dump designed initially for electrons. 10 PW Laser Beams Circular Polarizers are the vacuum vessels for the circular-polarization system. 10 PW Beams Switchyard is the vacuum vessels containing the switchyard of the two 10 PW beams for different focusing configurations and different interaction chambers.

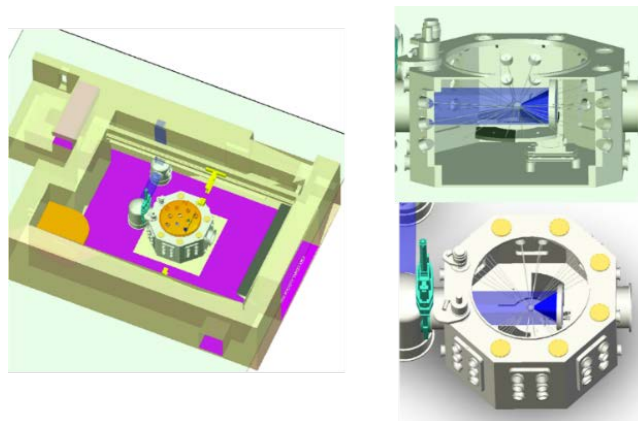


Fig. 34 – High Power Laser Interaction Chamber Example: the Vulcan 10 PW Laser Conceptual Interaction chamber: one 10 PW, 3 m diameter and 2.2 m height. Courtesy of Central Laser Facility, STFC Rutherford Appleton Laboratory, UK. The chamber is octagonal with doors and ports pointing to the center of the chamber which is also the Laser Focus and Interaction Point.

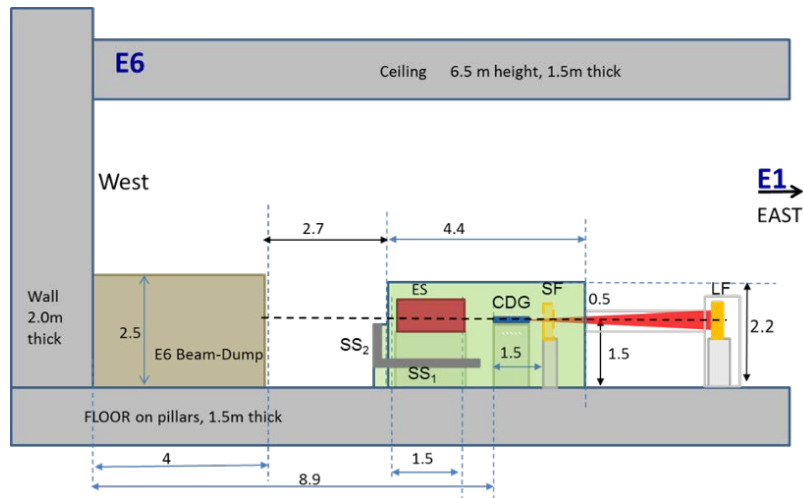


Fig. 35 – Vertical cross section through the E6 Interaction Chamber (ICE6), the E6 Beam Dump, the West wall, floor and ceiling of E6 experimental area. The exit of the Capillary Discharge Guide (CDG) is at the center of IC E6 located at 8.9 m from the West wall and 6.2 m from the North wall. The scintillating plates SS1 and SS2 are located below and respectively parallel with the exit face of the Electron Spectrometer (ES). The pump laser beam is focused on CDG by the long-focal ($f/20$) parabolic mirror (LF). The probe Laser beam (not shown) is focused by the short-focal ($f/3$) parabolic mirror (SF) and interacts with the electron beam just after its exit from the CDG. All dimensions are in meters.

Main functional requirements for the E6 Interaction Chamber are:

1. Working vacuum level 10^{-5} - 10^{-6} mbar.
2. Pump down time to 5×10^{-6} mbar in maximum 45 minutes.
3. Target position is always in the center of the octagon.
4. Coupling of the two 10 PW laser beam lines on the South-East corner of the chamber with DN800 flanges. It is envisaged that the chamber geometry deviates from an octagon in order to allow the input of the two laser beams, as shown in Fig. 36.
5. For access inside IC: several door-flanges will be installed, as shown in the Vulcan – 10 PW example in Fig. 34. However, the large E1 and E6 area is not a clean room (actually due to radioprotection restriction this area will be in under-pressure compared to adjacent corridors or experimental area). Therefore E1 has adopted a local soft-wall clean room attached to one of the doors of the IC, such that only this door will be used including for large off-axis parabolic mirrors (OAP), see Fig. 36. It is proposed that a similar soft-wall clean room could be implemented around the SE corner of the E6 chamber or around the North wall of the E6 chamber.

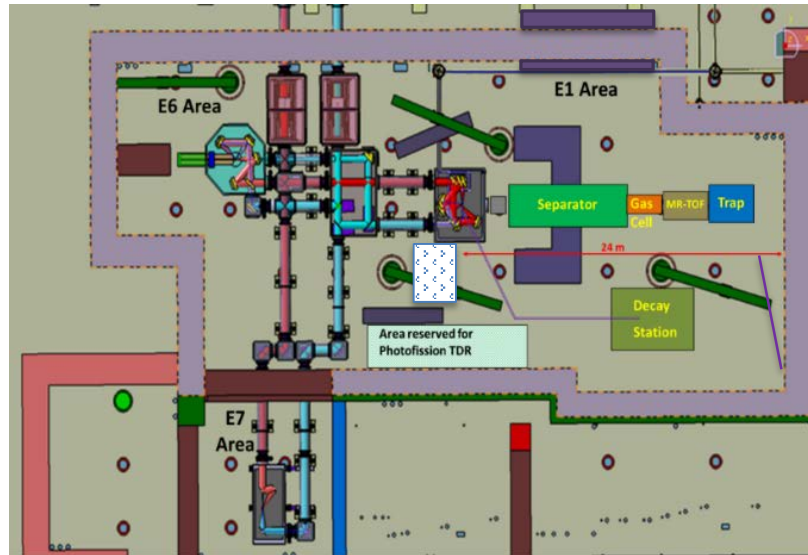


Fig. 36 – Layout of experimental areas where the two 10 PW beams are distributed. Main equipment in E1 area is drawn schematically. Especially we can see the white rectangle showing the soft wall clean-room for E1 chamber. Figure from TDR1 [97].

6. Modularity: the IC will be equipped with large rectangular flanges on the sides of the chamber each having up to 6 intermediary dimension flanges holding a number of standard dimension ports having inclinations such that to point toward target center. When other configuration of ports will be needed, only some of these rectangular flanges will be changed. The possibility to exchange these intermediary dimension flanges with other ICs will be foreseen.
7. When using the large, multi-GeV electron-spectrometer an adaptor flange will be installed center on the acceleration direction (west side of the chamber) that could be replace by an extension box of about allowing placement in vacuum of up to 4 m long magnet. Initially a 2 m long electromagnet is planned external to the chamber in forward direction.
8. Access on top of the IC should be provided because the exchange systems (manipulators) for targets and diagnostics will have a load-locked box located above primary target (and/or above secondary target in direction of acceleration)
9. As an example in E1 interaction chamber the optical table supporting the mirrors, targets and some of diagnostics will be decoupled from chamber. The distance between optical table and chamber wall should be about 100 mm. Expected height of the optical table is 800 mm while the laser beam axis is 1500 mm.
10. As an example in E1 interaction chamber connection with primary vacuum system could be done on the bottom side or back side of the chamber. The high

vacuum pumps (turbo molecular and cryopumps) should be placed under the chamber (as first option) or on top of the chamber (second option) taking into the need to access the load-locked box for target exchange.

Materials and design should consider activation minimization. Basic choice is Aluminum. EMP containment inside IC has to be taken into account thoroughly in design. Compatibility of flanges and ports with other laser ICs has to be assured.

As an example, the proposed design of the E1 IC is shown in TDR1 [97]. The lid is intended for removal only for the installation of the optical table inside the chamber. The intended vacuum seal for all large openings is dual O-ring differentially pumped. The chamber, lid, and removable walls construction are of aluminum alloy, ribbed to be lighter with high rigidity. The lid provides ports for the high vacuum pumping and safe access for Targets handling.

The beam-dump in E6 Area is on the west wall. Initially the 4 m beam-dump was designed for multi-GeV electrons only. This is shown in Fig. 36. We now have a new design for the beam-dump with the dual purpose of stopping both multi-GeV electrons and multi-100 MeV protons – see the section on radioprotection. The new beam-dump would allow experiments with both gas and solid targets in E6 chamber. For illustration Fig. 37 shows an artist's view of E6 interaction area with the new, larger beam-dump.

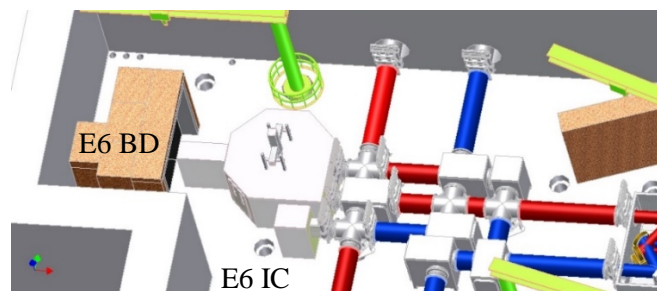


Fig. 37 – Artist's view of E6 interaction area with the new, larger beam-dump for both multi-GeV electrons and multi-100MeV protons. The larger beam-dump will allow both experiments with gas-targets and solid-targets for High Field Physics and QED.

3.2.2 Focusing geometries of two 10 PW laser beams in E6 interaction chamber

This chapter presents ray-tracing and engineering drawings of the E6 interaction chamber with two 10 PW laser beams focused in the following pump-probe geometries:

Gas targets. Two focusing geometries for the pump and probe 10 PW laser beams are envisioned:

1. (Pump) long focal length mirror ($f/20$) to accelerate the relativistic-electron-beam with the 10 PW pump laser beam focused on the gas.
2. (Probe) short focal length ($f/3$) mirror for the probe 10 PW laser beam which submits the electron-beam to the High Field Electromagnetic radiation.
3. The two mirrors are arranged to focus the laser beams either at small angle or at large angle between them. The large angle is also referred in the literature as counter-propagating beams.

Solid targets. Two main focusing geometries for the pump and probe 10 PW laser beams with additional geometries involving plasma mirror on the pump beam are proposed:

1. (Pump) short focal length mirror ($f/3$) to accelerate the relativistic-electron-beam with the 10 PW pump laser beam focused on the solid target.
2. (Probe) short focal length ($f/3$) mirror for the probe 10 PW laser beam which submits the accelerated electrons to the High Field electromagnetic radiation.
3. The two mirrors are arranged to focus the laser beams either at ‘small angle’ or at large angle between them.
4. Therefore there are 2 main focusing configurations for solid targets when the laser beams are focused directly on the target.
5. There are an additional 2 configurations when the pump laser beam is focused on target through a plasma mirror.
6. Again the angle between the focused lasers beams are: small angle and large angle.
7. The plasma mirror is designed to further enhance the contrast of the ultra-fast, 20 fs, main pulse with respect to pre-pulses or temporal pedestals.
8. The pump laser beam needs always be directed along the axis and towards the beam-dump on the West wall of the bunker. The reason is to ensure that the energetic electrons and protons are generated in the direction of the beam-dump. This requirement is valid both in the Plasma Mirror and normal focusing mode of the pump laser beam.
9. The proton production from the solid targets will be restricted to TNSA and RPA generation processes. The electron- and proton-beams generated by these processes will be strongly attenuated by the E6 beam-dump. There are reservations regarding the Breakout Afterburner (BOA) acceleration process for proton acceleration which could diverge in a cone. See also the Radioprotection Section.
10. While the experiments in E6 are not designed to accelerate protons, the beams of energetic protons are a by-product of the acceleration of electrons in solid targets.

As a matter of logistics/efficiency in scheduling experiments in E6, we could consider possible first experiments with gas and solid targets coupled/following one another: Configuration in Fig. 38 (a) for gas-target counter-propagating beams following configuration of Fig. 42 (a) solid target counter-propagating beams. In this case the top mirrors stay the same but use blue beam. Use Red beam for short focal distance mirror. Below we present the ray-tracing and engineering drawings for the focusing configurations:

3.2.2.1 Focusing Configurations for Gas Targets

The beam-beam for same direction and counter-propagating focusing beam geometry for a gas target is shown in Fig. 38 and 40 respectively. The 10 PW East-‘blue’ laser beam is directed to the E6 Interaction Station in the Switchyard. A long focal length mirror $f/20$ focuses the pump beam on the gas jet or gas cell inside the station generating the pulse of relativistic electrons. The 10 PW ‘red’ laser beam is directed to the E6 station and focused with a short focal length $f/3$ parabolic mirror on the electron pulse in the interaction point. The probe beam provides the strong EM field to generate the strong field effects we want to study. The energy spectrum of the multi-GeV electron pulse, perturbed by the probe-beam is measured with the electron spectrometer in order to resolve the changes in the electron energy spectrum due to the electron interaction with the strong EM field. The spectrometer needs to be close to the Interaction Point because the Radiation-Reaction can change the direction of propagation of the electron pulse. The spectrometer concept is discussed in the next section.

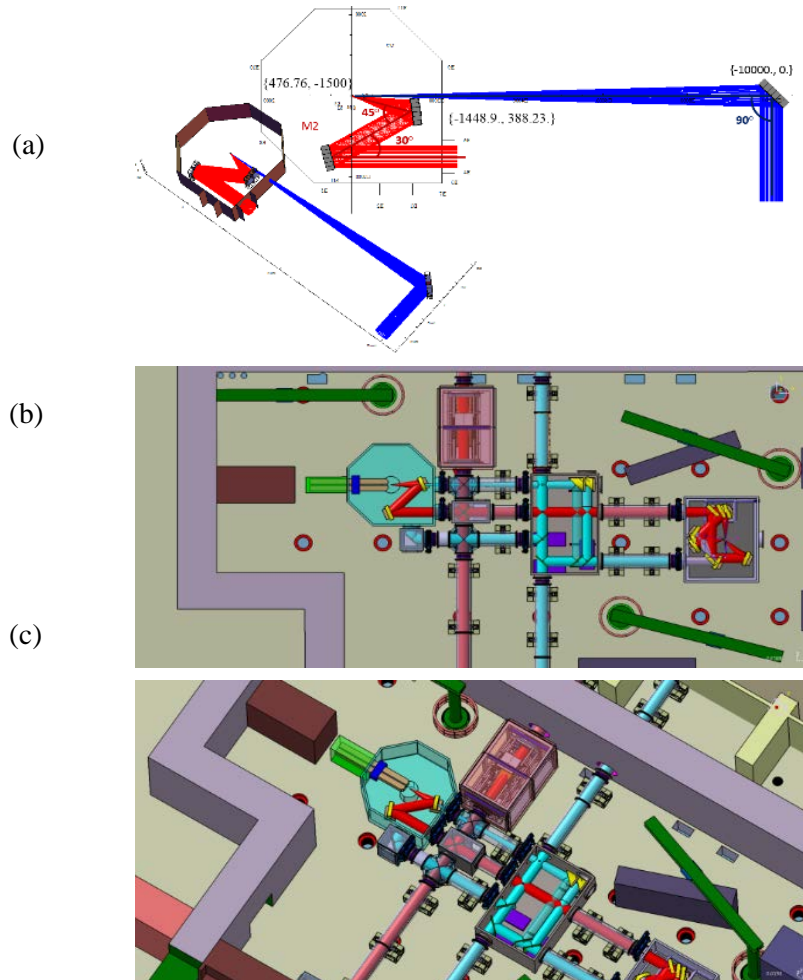


Fig. 38 – Long focus, $f/20$ mirror for e-beam acceleration by the pump laser and short focus, $f/3$ mirror for probe beam. Pump and probe beam propagate at small angle between them (quasi-same direction). 'Blue' is the pump beam and 'red' is the probe beam. The M2 mirror can be moved along red axis to ensure the chamber input direction. (a) ray-tracing (b), (c) engineering top view and Iso view. (a) Pump-beam passes close to the edge of the mirror of the probe beam. (b) Pump-beam passes through a hole in the mirror of the probe beam. The preferred option is the one in ray-tracing (above) where pump-beam passes close to the edge of the mirror of the probe beam instead. Mirrors with holes are expensive and distort slightly the reflected beam.

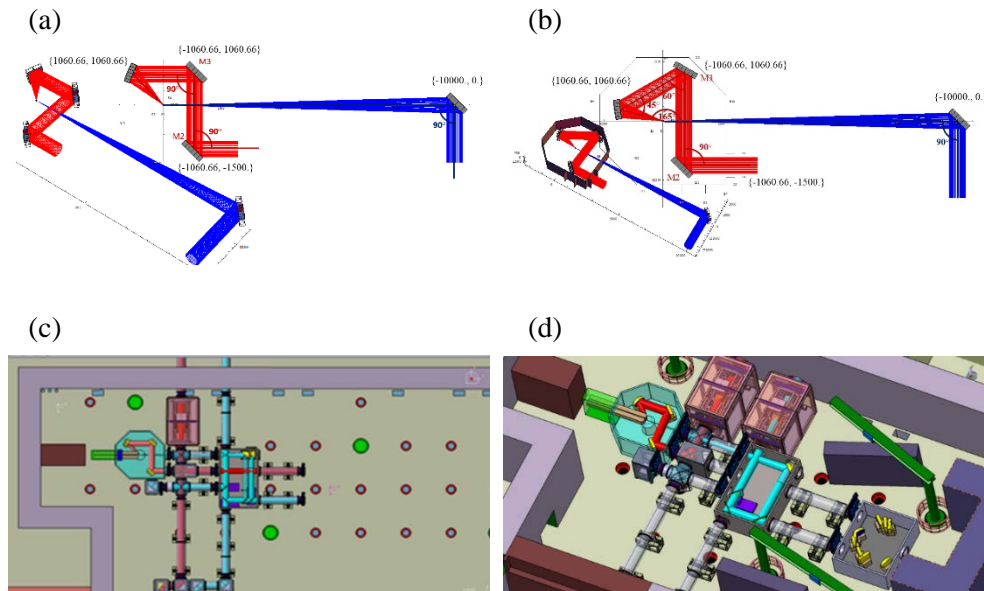


Fig. 39 – Long focus mirror for electron acceleration and short focus mirror for probe beam. Pump and probe beam propagate at large angle between them. The M2 mirror can be moved along red axis to ensure the chamber input direction and the incident angle can be adjusted by rotating and translating mirror M3. (a) ray-tracing, (b) 165 degrees angle, (c) - (d) engineering top view and Izo view.

3.2.2.2 Focusing Configurations for Solid Targets

The same-direction and counter-propagating focusing laser beam geometry for solid foil targets is shown in Figs. 41 and 42 respectively. The 10 PW West-‘Blue’ laser beam (the pump beam) and the 10 PW East-‘Red’ laser beam (the probe-beam) are tightly focused in the E6 station with short focal length $f/3$ parabolic mirrors on the solid target at the interaction point. The probe beam provides the strong EM field to generate the strong field effects we want to study. A number of diagnostics will be available for measuring: gamma-rays, electrons, positrons, ions, scattered laser light, etc. Since large energy protons/ions could be generated in the solid target by mechanisms other than Target Normal Sheath Acceleration (TNSA), the proton/ion beam direction will always be along the axis of the Beam Dump.

Considerations regarding implementation of Plasma Mirror in E6: We plan to install of single-plasma-mirror-reflection inside the interaction chamber, with the plasma mirror placed between the focusing parabola and target.

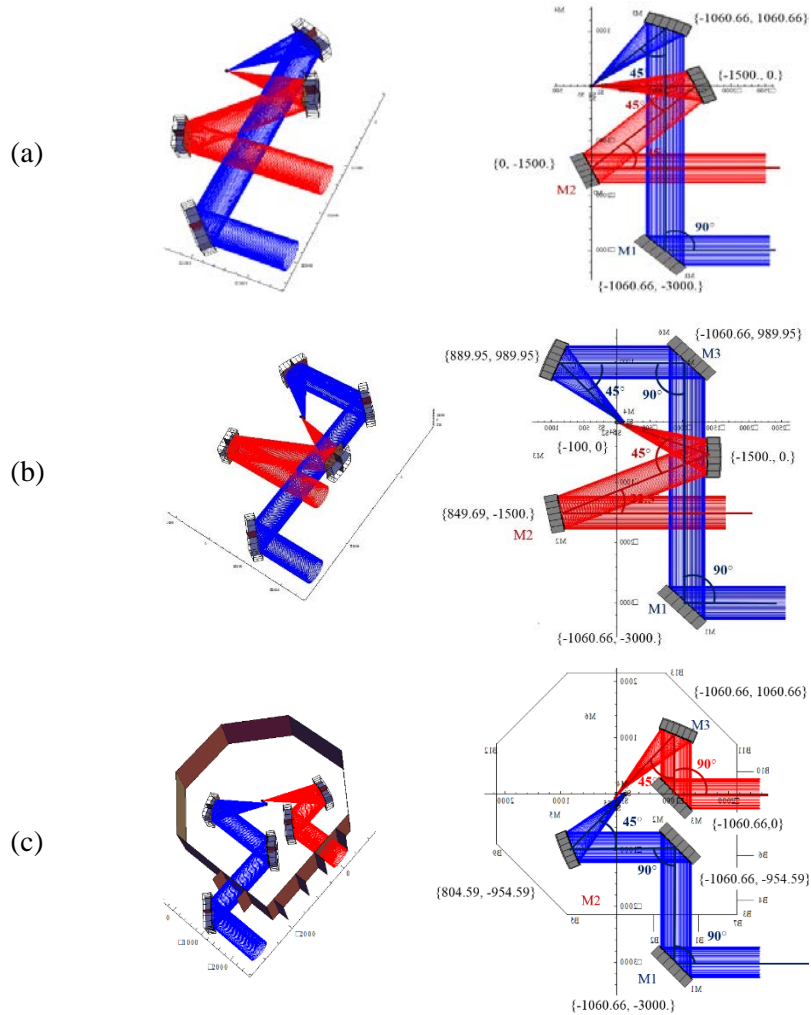


Fig 40 – Quasi same propagation direction beams. Short focus mirror for pump laser and short focus, mirror for probe beam. Pump and probe beam propagate at small angle between them (quasi-same-direction- propagating beams). ‘Blue’ is the pump beam and ‘red’ is the probe beam. (a) Ray-tracing without plasma mirror. The M1 and M2 mirrors can be moved along blue and respectively red axis to ensure the chamber input direction. (b) Ray-tracing with plasma mirror (PM). The input beam can be adjusted ± 100 mm from the nominal value, allowing for the M2 mirror to be adjusted to the configuration needs. (c) Ray-tracing showing the mirrors inside the interaction chamber E6. Both (b) and (c) are for PM and small angle.

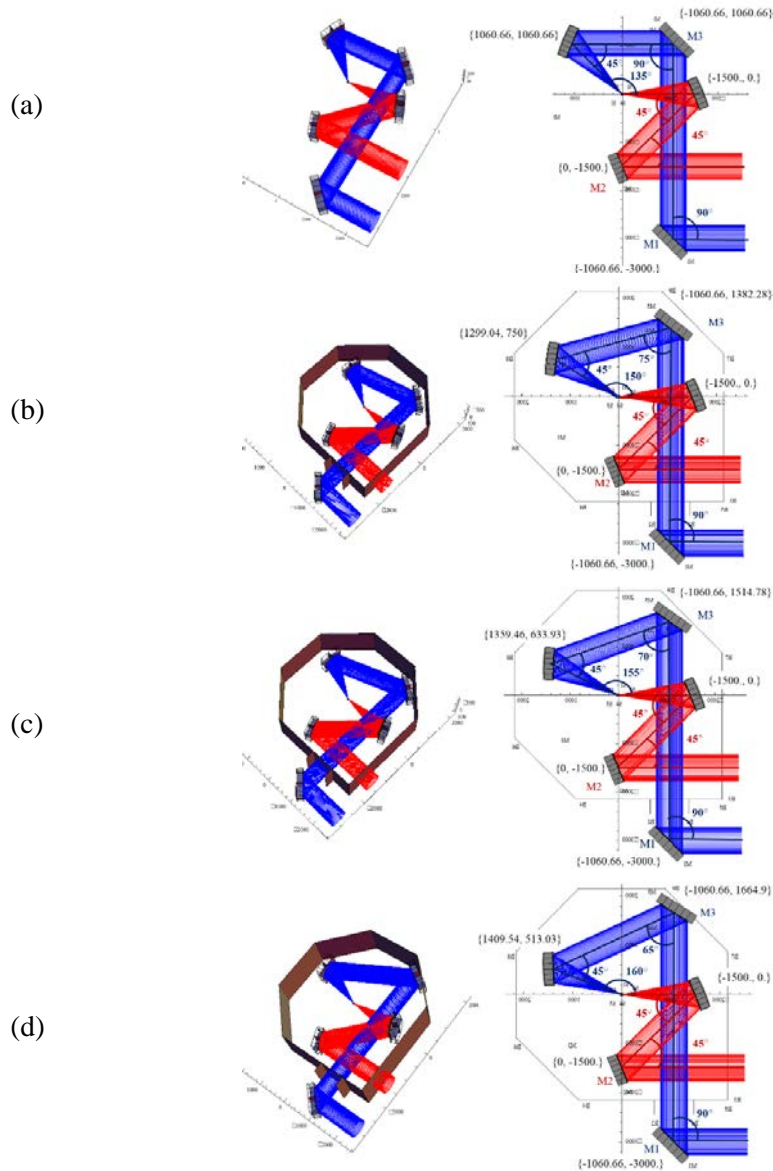


Fig. 41 – Quasi counter-propagating laser beams with short focus mirrors for both laser beams. Pump and probe beam propagate at large angle between them without plasma mirror: (a), (b), (c) and (d) depict ray-tracing of large angle configurations: 135 degrees and options for 150, 155 and 160 degrees. The M1 and M2 mirrors can be moved along blue and respectively red axis to ensure the chamber input direction. By rotating and translating M3 the incident angle can be adjusted.

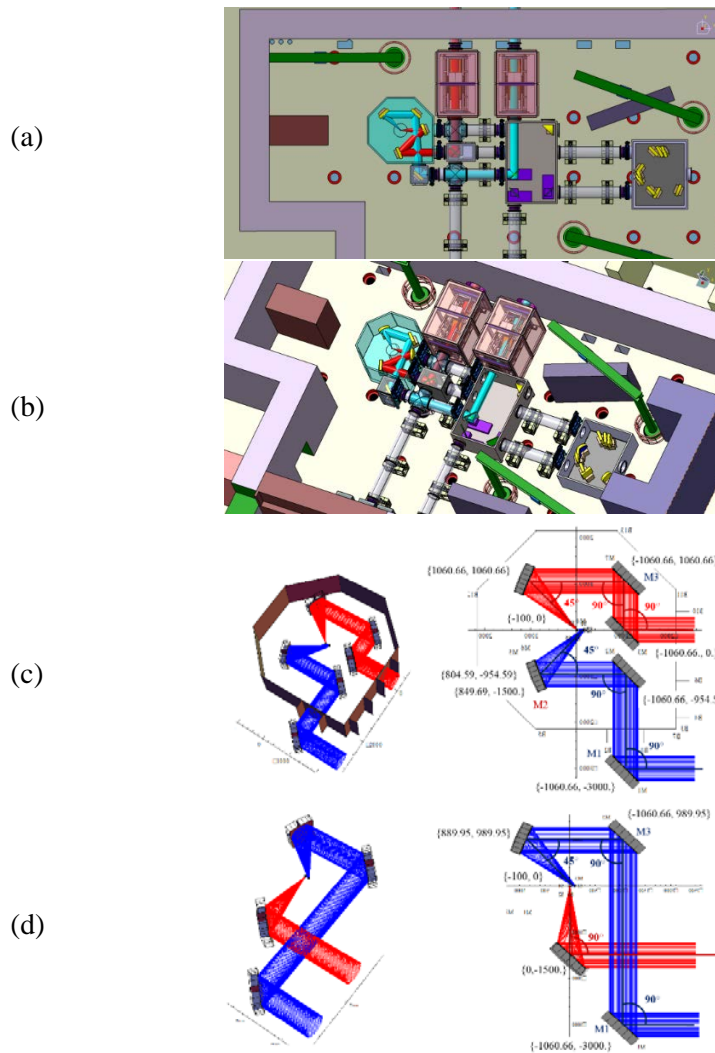


Fig 42 – (a) and (b) present engineering views of configuration of Fig. 41. (c) ray-tracing for 135 degrees with plasma mirror. The input beam can be adjusted ± 100 mm from the nominal value, allowing for the M2 mirror to be adjusted to the configuration needs. (d) 90 degrees angle ray-tracing with plasma mirror.

3.3 Targets and target systems

Thin and ultra-thin solid targets are requested by most of the experiments. Some experiments may ask for structured solid target (such as cylinders, cones) to control acceleration and optimize yields. Secondary solid targets are also requested to produce the desired nuclear reactions or nuclear states.

Gas targets for electron-beam acceleration will cover a wide range of densities. The gas targets are insertion system is either a nozzle or a capillary tube. The absence of target debris are important advantages of gas targets.

3.3.1 ELI-NP Target Laboratory

ELI-NP will have a dedicated Targets Laboratory: see TDR on ELI-NP Laboratories and Workshops. Here the mission of the Target Lab is explained as well as the types of targets to be manufactured in-house and the capabilities of the laboratory:

Mission of the Targets Laboratory: Dedicated facility that should provide the necessary tools and expertise for in-house manufacturing and characterization of a broad range of solid targets, required for experiments in physics, materials science and biology with high power lasers and γ -ray beams.

Presently, the envisaged targets type considered for in-house manufacturing are thin (nm range)/thick (few μm) films and foils of metals and oxides for high power lasers and γ -rays applications, pressed powders (pellets) for γ -rays applications and micro-targets for lasers and γ -rays applications.

The foreseen capabilities of the Target Laboratory are:

- Thin and thick films coating by e-beam deposition and sputtering.
- Structuring by optical lithography.
- Micro-machining/mechanical processing/cold rolling.
- Characterization of the targets (as well as of the samples prior- and/or post-experiments) by scanning electron microscopy with energy-dispersive spectroscopy (SEM+EDS), x-ray diffraction (XRD), atomic force microscopy (AFM), optical microscopy, interferometry;
- Acquiring the necessary expertise for fabrication of complex targets, with novel designs, and anticipation of future target developments.

The targets will need to meet the requirements of the user community. Proton removal from target foil is essential for reduction of activation levels. It has to be done in-situ, before laser shot (*e.g.* by heating or by irradiation with a 1 W laser) according to a procedure to be defined.

The number of needed targets will be approximately 300 per day for experiments in E1 and E6 and more than 10^3 per day in E5. A raster target with

dimensions up to $150 \times 150 \text{ mm}^2$ mounted on a 5-axis micro-positioning system with automatic alignment should be considered as standard choice for most of the experiments. More than 10^3 multi-targets (with $\mu\text{m-nm}$ thickness) can be accommodated.

3.3.2 Robotic Solid Target Loading with Air-Lock

In order to provide uninterrupted target irradiation for long interval of time at high laser repetition rates ELI-NP will implement in all interaction chambers a robotic target loading system with air-lock. This design for E5 Interaction Chamber is shown in Fig 43. The air-lock means that the target can be inserted quickly in the chamber, in vacuum, without opening the chamber to air. This minimizes the down-time needed for opening the chamber and realigning everything that moves during this process. The robotic arm passes the target to an automatic alignment system with 5-axis shown in Fig. 44. The targets themselves are composed of a wafer with multiple targets on a raster as shown in Fig. 45. This allows many laser shots to be delivered by automatic moving the wafer to the next target/window.

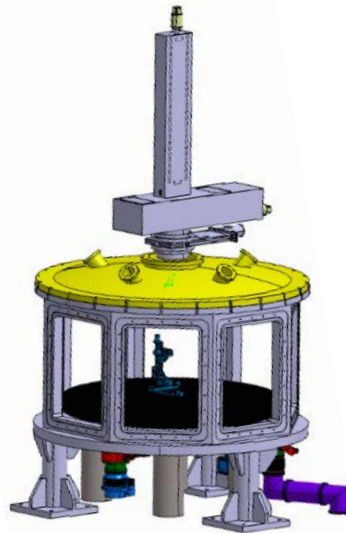


Fig. 43 – The proposed Interaction Chamber E5 shall accommodate an automated target manipulation system like the one presented in this figure. Note target air-lock for target insertion without opening the vacuum chamber [98].

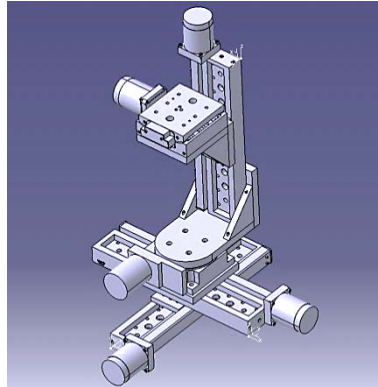


Fig. 44 – 5-axis micro-positioning system considered at ELI-NP for aligning the wafer with targets to the focus of the high-power laser beam [100].



Fig. 45 – Si wafer with approximately 1000 ultra-thin SiN windows to be manufactured in the ELI-NP Target Fabrication Laboratory.

3.3.3 Other targets under consideration

Tape target solution has to be considered as cost effective and satisfactory for experiments requiring above micrometer thick target (commercial solutions are available). The liquid crystal target produced in-situ [99] seems to be another adequate solution for high repetition rate lasers. Especially since these targets could be extremely thin.

Example of cryogenic targets (H and D) can be found in the proposal by Jean-Paul PERRIN (CEA) in the LoI submitted to ELI-NP. Work on cryogenic targets is also being pursued by GSI.

The target exchange system should allow the change of a primary or secondary target, or even some diagnostics such as RCF stacks, without opening the large volume E1 IC. This will be achieved by a load-lock vacuum chamber placed on top of IC and equipped with a motorized vertical motion linear stage. A prototype is under design, to be followed by its realization and delivery for test at CETAL facility (see Fig. 2 in Annex I of HPLS TDR 1 [98]).

3.4 Diagnostics and detectors

A range of diagnostic equipment and detectors will be required to be installed inside the laser-target interaction chamber and more widely within the experimental target area or hall. Bespoke gamma-ray detectors are required for in-chamber measurement and characterization of the γ -ray yield, energy spectrum and distribution produced within the target. These detectors must be insensitive to the EMP produced in a high power laser-target interaction environment. Additional γ -ray detectors based on more conventional techniques, such as scintillator crystals coupled to photomultiplier tubes and silicon-based detectors can be used outside of the interaction chamber, at some distance from the target. These should be positioned at a variety of angles with respect to the laser beam direction.

Charged particle spectrometers will be required to separate the electrons, positrons and ions. It is likely that relatively compact low resolution magnetic spectrometers will be required for inside the interaction chamber and that larger, higher resolution instruments will be positioned outside the chamber. A range of passive (film or track detector) and active (*e.g.* micro-channel plate or scintillator-based) detectors will be required, depending on proximity to the interaction environment and the effects of EMP.

A range of laser beam and optical probe diagnostics are required to probe the plasma expansion and the dynamics of the interactions (*e.g.* radiation pressure effects).

Several types of detectors which are planned to be implemented in ELI-NP high-power laser experiments. Gamma and particle detectors for the radiation generated by the laser-matter interaction. Plasma diagnostics which help us control the optimum plasma conditions in order to obtain the desired radiation: gamma or high energy particles. Laser detectors and diagnostics for the control of the optimum focusing conditions on target and for plasma diagnostics from the reflected and transmitted beams. Many detection strategies will be shared between different interaction areas. A detailed description of neutron detectors, several proposed diagnostics for electromagnetic fields and passive diagnostics can be found in HPLS TDR 1 [97].

Fig. 46 illustrates the concept of using electron, ion and gamma spectrometers

to measure the spectral changes in the relativistic electron beam when it is subjected to high electromagnetic fields in the focus of the probe beam.

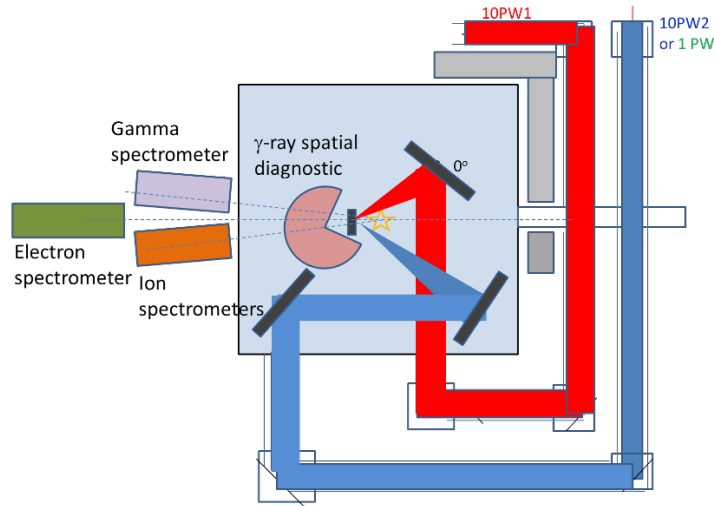


Fig. 46 – Conceptual diagram illustrating typical detectors used in an experiment with solid targets. Electron, ion and gamma diagnostics are shown. Note the chamber and laser beam transport and focusing configuration is different from the accepted focusing configurations. This figure is for illustration purposes of typical detectors.

3.4.1 Active detectors and fast diagnostics. EMP damage mitigation

Due to high repetition, active detectors/diagnostics are of high priority for laser driven experiments at ELI-NP. Similar with other interaction chambers [97], in this category we include: Thomson parabolas, CsI and liquid or plastic scintillators for gamma ray detection, respective, neutron spectroscopy, Lanex scintillators read by CCD camera and imaging systems for electron and positron spectroscopy.

Plasma diagnostic is essential to characterize the temperature and density of plasma. X-ray diagnostic (imaging and spectroscopy), Interferometry, VUV imaging and spectroscopy are needed. Low energy probe beam is also considered for plasma diagnostics.

Because these detectors are active during laser pulse, they and their associated (analogue and digital) electronics are subject to damages produced by EMP. Some of them are placed in vacuum where EMP can be very high. Since EMP amplitude at ELI-NP cannot be estimated a priori it was proposed to implement strong filtering and shielding for building because here it will difficult to add something at later stages, while at level of experiments to choose only reasonable solution and to

reinforce them only if it will appear necessary during first experiments. We will learn also from first experiments at CETAL in 2015 and at Apollon/CILEX in 2015/2016. Enclosing the detectors in metal cases, use double shielding coaxial cables for signal transmission and filters that cut frequencies higher than those used by detectors, along with installation of electronics in EMP shielded racks, are the main solution to be applied when optical transmission is not possible, as depicted in the Fig. 47.

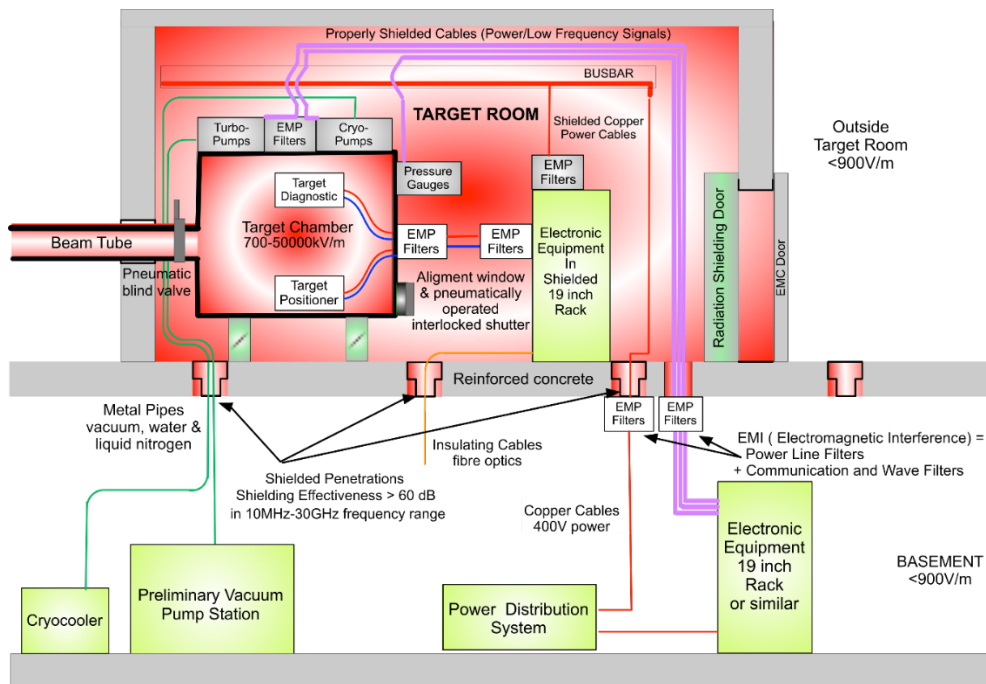


Fig. 47 – EMP shielding strategy for a typical interaction chamber. The values cited correspond to EMP estimation based on scaling with laser power.

3.4.2 Electron Spectrometer for multi-GeV electrons in High Field Physics and QED experiments with gas-targets

Fig. 48 and 49, illustrates the concept of using a powerful electron spectrometer to measure the spectral changes in the relativistic electron beam when it is subjected to high electromagnetic fields in the focus of the probe beam. The first 10 PW laser beam (pump-laser, red) is focused into a 1 m long gas capillary where the electrons are accelerated by the wake-field produced in the plasma. Say the electron energy exceeds 10 GeV. The record electron energies are around 2-3 GeV with the present lasers. The second 10 PW laser (probe-laser, also red) is focused on the accelerated electron bunch perturbing its motion due the intense electromagnetic field in the focus. The electron bunch (blue) is dispersed in energy by the magnetic field (above

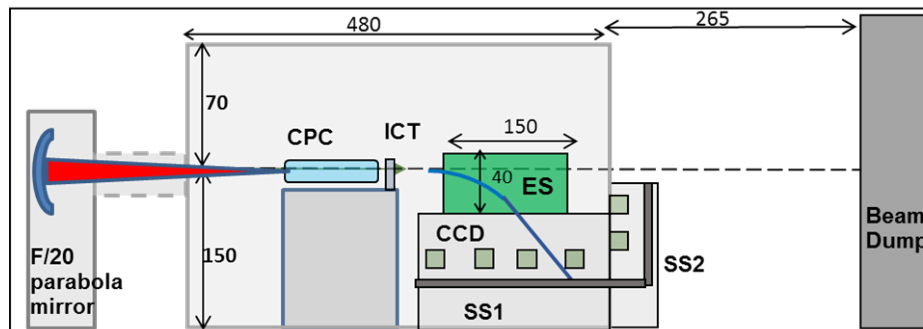


Fig. 50 – A projected view in the vertical plane through the center of the E6 interaction chamber, the $f/20$ parabola mirror to focus the 10 PW pulsed laser beam on the capillary discharge guide (CDG), electron spectrometer ES (150 cm long), six CCD cameras and the two scintillating screens (SS1, SS2). All dimensions are in centimeters.

An energy resolution $\Delta E/E$ better than 5% is expected which should be sufficient to resolve the fine changes in the electron-energy spectrum due to radiation reaction and other strong fields effects.

The electrons with high enough energy exit through the vertical face of the permanent magnet, enter in the gap of a 1.5 m long electromagnet and interacts with the Scintillating Screens (SS1, SS2) located outside the E6-IC. The light emitted from the electron spot on the SS1 and SS2 is detected by two CCD cameras located on the lateral walls of the E6-IC.

3.4.3 Gamma detectors

An example of an active, gamma ray detector is given by McKenna *et al.* in this TDR2. The group is developing an angular array of scintillators to make gamma-ray measurements. A continuous wrap-around imaging plate detector pack, with a magnetic field to remove electrons, will be employed to measure detailed changes to the angular distribution of the γ -ray emission. Noise from bremsstrahlung emission from the target will be minimized by using low- Z targets.

3.4.4 Lanex plate for electrons and positrons

Scintillator phosphor plate for electron/positron detection. The phosphorescence is imaged on a CCD cameras which connected to the Data Acquisition System. This is the case of the multi-GeV electron spectrometer. The electron spectrum will be computed and displayed without having to open the interaction chamber. A requirement on the DAQ system is to process the data on-

line between laser shots. The laser shots may not necessarily be 1min apart which is the max repetition rate of the laser.

3.5 Control system

The ELI-NP E6 area dedicated to the High Field QED experiments will have the experiment monitoring and control systems architecture similar to the HPLS and LBTS control systems [100]. The architecture is based on TANGO that will permit local distributed control of the equipment and additional clients to remotely supervise/control the experiment.

This solution will allow a standardization of the control systems inside ELI-NP, while providing easy maintenance, better security, better logging and interfacing methods between the experimental areas, HPLS and LBTS.

A dedicated User Room will be used to remotely control from outside the E6 area the equipment as the experiment is running and a TANGO framework will be developed to link the experimental area to the User Room using a dedicated client – server architecture.

A data storage server will be available for short term experimental data saving and this shall benefit in general from dedicated data busses, separated from the client – server TANGO architecture that controls and monitors the equipment itself, in order to achieve the highest data throughput.

Dedicated TANGO servers and clients are envisaged to interface the equipment necessary in the experiment such as: focal spot monitoring, gas target alignment system, gas target manipulation, delay generators, monitoring CCDs and vacuum system for the E6 interaction chamber.

For the equipment where the API is not provided and which already have Human Machine Interfaces developed, the link between User Room and experimental area will be made using remote desktop or other similar solution.

The experimental equipment will have a Human Machine Interface able to locally (from inside the interaction area) or remotely (from the User Room) monitor and control the parameters needed to run the equipment and the experiment.

The User Room will also provide through the TANGO architecture information to the user regarding the HPLS parameters and LBTS configuration. The HPLS and LBTS parameters will be controlled from the HPLS control room by the operators from personnel and machine safety reasons.

3.6 Radiation Sources and safety requirements

The radiological protection assessments for all the ELI-NP experimental areas were performed by Nuclear Technologies from UK and are presented in a series of reports [101,102]. These references include the most recent Reports regarding the

Interaction Area E6 dedicated to High Field Physics and QED experiments with two 10 PW laser beams. Fig.51 shows the distribution of source terms in all the ELI-NP experimental areas.

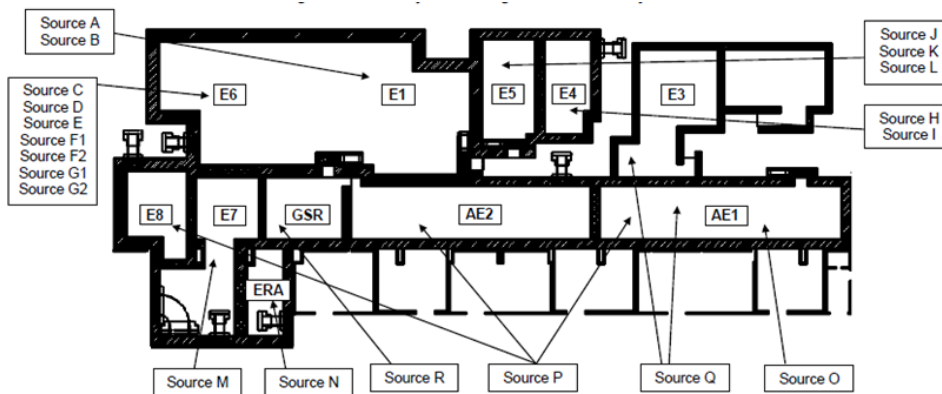


Fig.51 – Distribution of source terms in ELI-NP experimental areas. From Nuclear Technology Report [101].

Experiments on High Field Physics and QED in E6 interaction chamber will generate intense radiation from multi-GeV electrons, multi-100 MeV protons and energetic gamma rays.

In the E6 experiments will be produced 6 source terms which are shown in Table 1. The source terms were estimated by the user community and provided to Nuclear Technologies in order to calculate the necessary beam-dump and the expected radiation doses. The source terms were estimated from simulations and extrapolation of present measurements with PW-class lasers. There is no experimental data from the interaction of 10 PW laser beams with matter: ELI-NP is likely to be one of the first such systems in the world. Note that number of days/year for each source term is 90 days/year and not 250 days/year. This is because the laser beams are shared between several types of experiments and interaction areas.

Table 1 – Source terms in ELI-NP, E6 interaction area dedicated to High Field Physics and QED [101, 103]

	Particle	Mean Energy (GeV)	Particles/ Pulse	Frequency (Hz)	Divergence (Degrees)	Distribution	FWHM (GeV)	Particles/ Second
C	Electron	38	8.61E+10	0.017	± 0.5	Gaussian	0.001	1.44E+09
D	Photon	n/a	3.14E+14	0.017	± 20	Thermal	n/a	5.23E+12
E	Electron	0.145	5.00E+12	0.017	± 25	Maxwell	n/a	8.33E+10
F1	Photon (bremsstrahlung from target)	n/a	n/a	0.017	Depends upon the electron reflux within the target. If there is no reflux, assume 50-60 degrees. If refluxing, then assume 360 degrees.	Maxwell	n/a	n/a
F2	Photon (synchrotron)	0.01 MeV - 30 MeV, with an average energy of 10 MeV.	1.00E+14	0.017	Total divergence of 80° in both forwards and backwards directions (see comments)	Rectangular	0.01	1.67E+12
G1	Proton	~40 MeV for a thermal TNSA spectrum, with a maximum energy of 250 MeV.	6.00E+12	0.017	50° for TNSA, directed along the normal to the target foil. The normal to the target foil can be 12°-30° from the direction of the pump laser and therefore 12°-30° from the axis of the beam dump.	Boltzmann	n/a	1.00E+11
G2	Proton (via RPA or BOA type processes)	0.5	1.00E+12	0.017	+/- 2.5	Quasi-mono energetic	0.05	1.67E+10

The Beam-dump requirements from the earlier NT Reports (2012) have been extended to cover 500 MeV protons as well as up to about 38 GeV electrons. Initially the beam dump was calculated only for electron-beam accelerated up to 38 GeV. This would have been sufficient for gas-targets only. But solid-targets experiments are the other major area of research in High Field Physics and QED. When solid targets are irradiated with high power lasers, the electrons are accelerated (which is what we want to study) but as they exit the target, protons are also accelerated. The energy and angular distribution of the protons depends on the mechanism of production. For example protons of up to 500 MeV energy are expected if they are accelerated by the RPA mechanism. Because the RPA produced protons are directional, the decision was taken that the 10 PW laser pump beam will be always directed towards the beam dump and along the axis of the BD. This is the geometry used in the focusing configurations for E6. As a result, Nuclear Technologies has redesigned the E6 beam-dump which is presented in Fig. 52 (reproduced from their report) and the materials comprising the BD are presented in Table 2 [102]. The mass per unit area of the BD inside the E6 area is 16.7 tones/m². The total mass of the BD including the Muon shield (7 m long Iron cylinder with radius of 0.4 m) located outside the E6 area, is now 278 tons as compared to 152 tons in May 2014. A recent NT Report suggests that the Muon-shield may not be needed, certainly in the initial experiments.

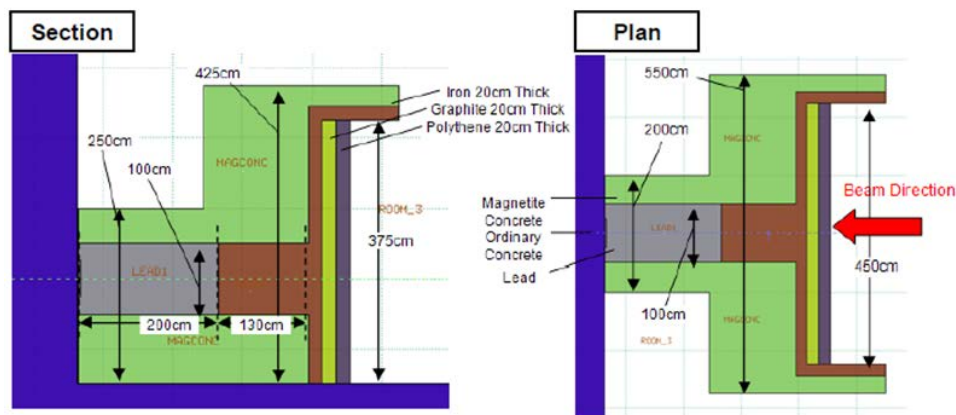


Figure 3: Illustration of Assumed Beam Dump Geometry

Fig. 52 – The E6 beam-dump dimension and composition assumed by NT in radioprotection calculations. The dual purpose beam-dump stops both multi-GeV electrons as well as multi-100s MeV protons. From Nuclear Technology Report [101].

First report [101] presents the radiation dose assessments in the E1 and E6 experimental areas assuming no wall penetrations. The summary of the report reads:

“The aim of this assessment is to review the bulk shielding of E6 within the ELI-NP facility, with respect to revised E6 source terms.”

Dose rates in corridors and neighboring areas from source terms E, F1 and F2 have been demonstrated to be significantly below the design criteria.

Table 2 – Summary of Densities and Material Compositions [101].

Element	Mass Fractions								
	Magnetite Concrete	Ordinary Concrete	6061 Aluminium	718 Inconel	Air	Polythene	Graphite	Iron	Lead
Al	0.02349	0.01995	0.97200	0.00500					
Ar					0.01283				
B10				9.985E-06					
B11				4.009E-05					
C		0.00248		0.00073	0.00012	0.85628	1.0000		
Ca	0.07102	0.04295							
Co				0.00910					
Cr	0.00170		0.00020	0.19000					
Cu			0.00275	0.00273					
Fe	0.47425	0.00644	0.00409	0.17000				1.0000	
H	0.00311	0.02210				0.14372			
K		0.01005							
Mg	0.00934	0.00127	0.01000						
Mn	0.00198		0.00088	0.00318					
Mo				0.03050					
N					0.75527				
Na		0.01521							
Nb				0.05125					
Ni				0.52500					
O	0.33050	0.57493			0.23178				
P				0.00014					
Pb									1.0000
S	0.00142			0.00014					
Si	0.02575	0.30463	0.00600	0.00318					
Ti	0.05433		0.00088	0.00900					
V	0.00311								
Zn			0.00146						
Density (gcm ⁻³):	3.53	2.30	2.70	8.19	0.001205	0.93	1.70	7.874	11.35

Source terms G1 and G2 produced dose rates that exceeded the design criteria. However, the addition of a window within the aluminum interaction chamber can reduce primary particle interactions within materials upstream of the beam dump and this has been demonstrated to reduce cold-side dose rates within the adjacent corridors and neighboring areas.

It is therefore recommended that these calculations be revisited once a specification for the interaction chamber and any window has been finalized. However, the results presented within this report do give a high degree of confidence that dose rates can be demonstrated to be acceptable (given the current shielding arrangement and source parameters) if sufficient optimization of the beam dump and/or interaction chamber is undertaken. Note that window should be sufficient to encompass large divergent beams.

Table 3 summarizes these results. Fig. 53 illustrates the radiation calculations results for E6 area for the RPA produced 0.5 GeV protons.

Table 3 – Summary of Calculated Dose Rates ($\mu\text{Sv/hr}$) for E6 area geometry. From Nuclear Technology Report [101].

Dose Points (Figure A2.6)	Location	Distance (cm)	Total Dose Rate ($\mu\text{Sv/hr}$)						
			Source E	Source F1	Source F2	Source G1		Source G2	
			Without Window	Without Window	Without Window	Without Window	With Window	Without Window	With Window
1	South Wall	Hot-side	n/a	n/a	n/a	n/a	n/a	4.21E+03	9.23E+02
2	South Wall	1	n/a	n/a	n/a	2.73E+00	1.75E+00	9.83E+00	1.66E+00
3	South Wall	100	n/a	n/a	n/a	1.21E+00	1.11E+00	4.42E+00	6.55E-01
4	Roof	Hot-side	1.33E+04	9.20E+03	5.27E+04	8.05E+03	5.77E+03	9.87E+03	2.58E+03
5	Roof	1	2.63E-01	4.06E-01	1.28E+00	1.93E+01	1.32E+01	5.13E+01	7.47E+00
6	Roof	100	9.95E-02	2.69E-01	6.00E-01	9.56E+00	6.25E+00	2.53E+01	4.63E+00

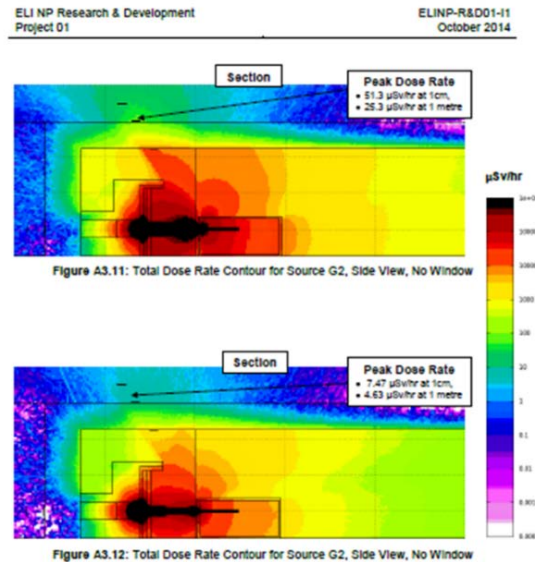


Fig. 53 – Radiation calculations results for E6 area for the RPA produced 0.5 GeV protons. From Nuclear Technology Report [101].

The second report [102] calculates the radiation doses in the basement of the building, underneath E6 chamber. E6 area geometry for NT radiation calculations is shown in Fig. 55 and Fig. 56. Again no penetrations in the floor were assumed. The calculations also includes the energetic electrons deflected by the electron-spectrometer for multi-GeV electrons. The conclusion is the deflected electrons towards the basement are not the main concern: the highest radiation dose comes from the scattered protons. Fig. 57 shows the radiation calculations for the E6

basement for the situations when the multi-GeV electron beam is deviated towards the basement by the magnetic field of the electron-spectrometer.

We also present an experimental time allocation schedule according to each or groups of source terms.

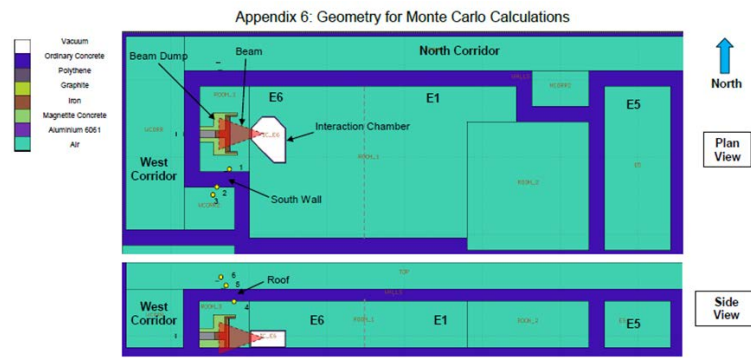


Figure A2.6: Geometry for Monte Carlo Calculations

Fig. 55 – E6 area geometry for radiation calculations. From Nuclear Technology Report [101].

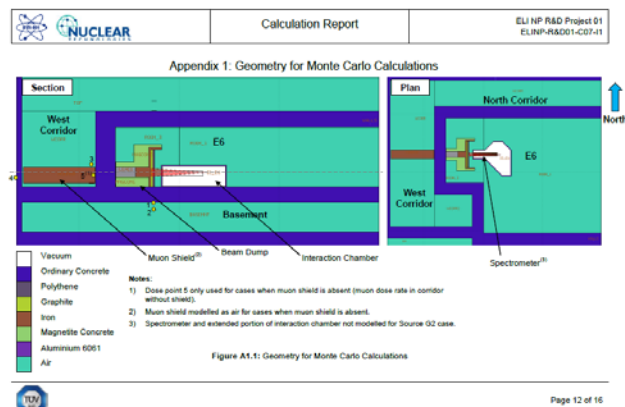


Figure A1.1: Geometry for Monte Carlo Calculations

Fig. 56 – E6 area geometry for NT radiation calculations for the situations when the multi-GeV electron beam is deviated towards the basement by the magnetic field of the electron-spectrometer. From Nuclear Technology Report [102].

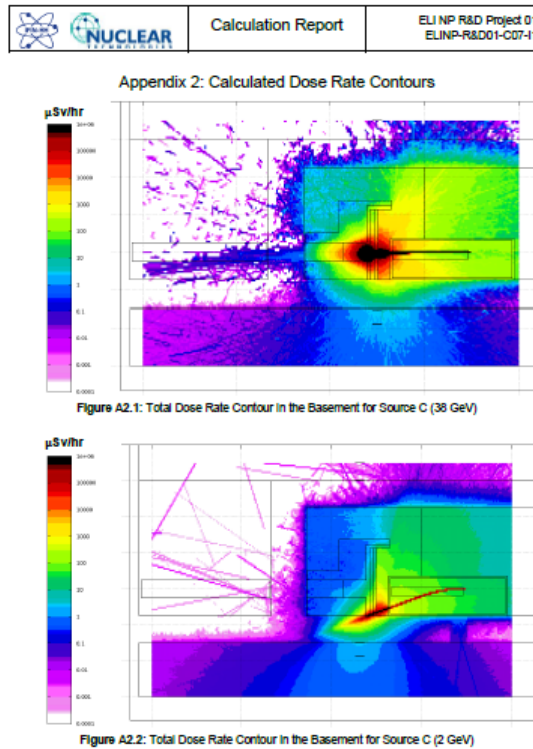


Fig. 57– Radiation calculations for E6 basement for the situations when the multi-GeV electron beam is deviated towards the basement by the magnetic field of the electron-spectrometer. From Nuclear Technology Report [102].

Doses calculated for the cold side of the roof impose that it will be inaccessible when beam is present in E1 (a condition that will be imposed actually for all laser experiments).

For the activation calculations the expected running time of each source term was requested in input. An analysis of operation modes of ELI-NP facility proposed that the experiments in E1 and E6 experimental area will run, in average, 90 days per year at 300 pulses per day (excluding the days for setting-up/dismounting the experiments). The E1 and E6 areas will not run 10 PW experiments at the same time. It is also proposed that we distribute 45 days to gas target experiments (no energetic protons) and 45 days to solid-target experiments. We distributed therefore 15 days for source term A and 75 day for source term B.

The monitoring with active detectors the doses produced on-line by high-power lasers is not possible with commercially available detectors, only outside the experimental area (see Radiation Protection and Safety TDR [103]). Some active

gamma dosimeters will be installed inside and outside experiment hall for activation monitoring. But those inside will be switched-off during laser shots sequences (runs) while those outside will just record one more pulse for each laser shot. A special system based on several plastic scintillators operated at low gain (in order to avoid signal saturation) is proposed, operated in pulse integration mode with a trigger signal generated by laser system. After its calibration against passive dosimeters, they can provide relevant information for laser and experimental arrangement optimization. For neutron measurement, plastic scintillator loaded with ^{10}B can be used and detectors embedded in paraffin/polyethylene neutrons moderators. The development and construction of such detectors are included in the Dosimetry TDR [103].

4. CONCLUSIONS

The ELI-NP facility will provide focused laser intensities above 10^{21} Wcm^{-2} and reaching 10^{22} - 10^{23} Wcm^{-2} to be achieved for the first time. We proposed to use this capability to investigate new physical phenomena at the interfaces of plasma, nuclear and particle physics at ELI-NP. This document, TDR2, proposes a comprehensive experimental area (E6) at ELI-NP for investigating High Field Physics and Quantum Electrodynamics and the resulting production of electron-positron-pairs and of energetic gamma-rays.

This work presented the commissioning runs proposed by the scientific community to be performed within the E6 Experimental Area for High Field Physics and QED: 12 proposals for E6 interaction chamber with two 10 PW laser beams and 1 proposal for the CETAL interaction chamber with 1 PW laser beam, in preparation for the ELI-NP experiments. The runs are classified according to the science area investigated into: Radiation Reaction Physics: Classical and Quantum (2 proposals for solid targets and 4 gas targets at ELI-NP and one at CETAL); Compton and Thomson Scattering Physics: Linear and Non-Linear Regimes (2 proposals with solid targets); QED in Vacuum (2 proposals and potentially proposals submitted to E7 interaction area); Atoms in Extreme Fields (1 proposal with gas target).

TDR2 presents the quasi-octagonal 4.5 m diameter E6 interaction chamber with two pump-probe colliding 10 PW laser beams. Experiments are designed for: (a) gas targets in which the pump laser-beam is focused by a long focal length ($f/20$ or $f/80$) mirror and drives a wakefield in which the electron bunch is accelerated to multi-GeV energies and then exposed to the EM field of the probe laser which is tightly focused ($f/3$); (b) solid targets in which both the pump and probe laser beams are focused on the solid target. There are also Vacuum QED experiments which require no target but use the similar interaction geometries and diagnostics to the ones above.

We designed four focusing configurations for the pump and probe laser beams, two for each type of target: (a) counter-propagating 10 PW focused laser beams and (b) the two 10 PW laser beams focused in the same direction. For solid targets we ray-traced an additional configuration with plasma-mirror on the pump laser beam: the plasma mirror placed between the focusing mirror and target. We proposed that the 10 PW laser beams will have polarization control and focus control by means of adaptive optics. Initially only one 10 PW may have polarization control and adaptive optics.

Solid targets will be inserted by a robotic system such that the target renewal time is minimized for long time operation of the interaction chamber E6 with minimum downtime for opening the chamber to air. This will take advantage of the high repetition rate of the 10 PW laser system. Solid targets will be manufactured in the ELI-NP Target Laboratory or purchased.

A large electron-spectrometer, up to 4m long, is proposed for multi-GeV electrons. Other diagnostics will measure: gamma-rays, electrons and positrons, protons and ions, plasma characterization, transmitted and reflected laser beam. Diagnostics will benefit from the Electronics Laboratory and the Optics Laboratory. The E6 experiments will have access to the ELI-NP Workshops.

The Control system is described in the specific TDR on Monitoring and Control, summarized here.

Radiation Source-Terms are provided for the proposed experiments. Radiation calculation is provided by the Nuclear Technology Reports for ELI-NP and specifically for E6 experimental area. Radiation-protection is provided by a 4m long beam-dump for both multi-GeV electrons and multi-100 MeV protons. E6 and E1 interaction area is placed in the bunker with 2 m thick concrete walls. The bunker is 20 m wide and 50 m long.

E6 Experiments will use the extensive ELI-NP infrastructure (workshops, laboratories, utilities, data acquisition and control systems) which is designed to take into account the TDR2 needs.

Acknowledgements. The work was supported by the Project Extreme Light Infrastructure - Nuclear Physics (ELI-NP) - Phase I, a project co-financed by the Romanian Government and European Union through the European Regional Development Fund.

REFERENCES

1. P.A.M. Dirac, Proc. R. Soc. Lond. A **167**, 148 (1938).
2. L.D. Landau and E.M. Lifshitz, *The Classical Theory of Fields*. 4, Butterworth – Heinemann, New York (1987).
3. G.W. Ford, R.F. O'Connell, Phys. Lett. **157**, 217 (1991).
4. A. Di Piazza, K. Z. Hatsagortsyan, and C. H. Keitel, Phys. Rev. Lett. **102**, 254802 (2009).

5. C. Harvey *et al.*, Phys. Rev. Lett. **109**, 100402 (2012).
6. N. Neitz and A. Di Piazza, Phys. Rev. Lett. **111**, 054802 (2013).
7. S. Cipiccia *et al.*, Nature Phys. **7**, 867 (2011).
8. S. Corde *et al.*, Rev. Mod. Phys. **85**, 1 (2013).
9. D.L. Burke *et al.*, Phys. Rev. Lett. **79**, 1626 (1997).
10. H. Hu, C. Müller, and C. H. Keitel, Phys. Rev. Lett. **105**, 080401 (2010).
11. S.-Y. Chen, A. Maksimchuk, and D. Umstadter, Nature **396**, 653 (1998).
12. D. Umstadter, J. Phys. D: Appl. Phys. **36**, 151 (2003).
13. S.-Y. Zhou, Optik **123**, 1707 (2011).
14. M. Tamburini, *et al.*, Nucl. Instr. Meth. Phys. Res. A **653**, 181 (2011).
15. J.G. Kirk, A.R. Bell, and I. Arka, Plasma Phys. Control. Fusion **7**, 085008 (2009).
16. C.P. Ridgers *et al.*, J. Comput. Phys. **260**, 273 (2014).
17. B. Cros *et al.*, Nucl. Instr. Meth. Phys. Res. A **10**, 1 (2013).
18. S.V. Bulanov, Nucl. Instr. Meth. Phys. Res. A **660**, 31 (2011).
19. J. Schwinger, Phys. Rev. **82**, 664 (1951).
20. C. P. Ridgers *et al.*, Phys. Rev. Lett. **108**, 165006 (2012).
21. C. S. Brady *et al.*, Phys. Rev. Lett. **109**, 245006 (2012).
22. C. S. Brady *et al.*, Phys. Plasmas **21**, 033108 (2014).
23. T. Nakamura *et al.*, Phys. Rev. Lett. **108**, 195001 (2012).
24. T. Esirkepov *et al.*, Phys. Rev. Lett. **92**, 175003 (2004).
25. Di Piazza, K. Z. Hatsagortsyan, and C. H. Keitel, Phys. Rev. Lett. **102**, 254802 (2009).
26. ELI project: <http://www.extreme-light-infrastructure.eu/>
27. H. Daido *et al.*, Rep. Prog. Phys. **75**, 056401 (2012); A. Macchi *et al.*, Rev. Mod. Phys. **85**, 751 (2013) and references therein.
28. Zhidkov, J. Koga, A. Sasaki, and M. Uesaka, Phys. Rev. Lett. **88**, 185002 (2002).
29. J. Koga, T. Zh. Esirkepov, and S. V. Bulanov, Phys. Plasmas **12**, 093106 (2005).
30. M. Tamburini *et al.*, New J. Phys. **12**, 123005 (2010).
31. N. Naumova *et al.*, Phys. Rev. Lett. **102**, 025002 (2009).
32. M. Tamburini, Nucl. Instrum. Meth. A **653**, 181 (2011).
33. M. Chen, A. Pukhov, T. P. Yu, and Z. M. Sheng, Plasma Phys. Control. Fusion **53**, 014004 (2011).
34. R. Capdessus, E. d'Humières, and V.T. Tikhonchuk, Phys. Rev. E **86**, 036401 (2012).
35. R. Capdessus, E. d'Humières, and V.T. Tikhonchuk, Phys. Rev. Lett. **110**, 215003 (2013).
36. M. Vranic *et al.*, Phys. Rev. Lett. **113**, 134801 (2014).
37. G. R. Thomas *et al.*, Phys. Rev. X **2**, 041004 (2012).
38. R. Capdessus *et al.*, Phys. Plasmas **21**, 123120 (2014).
39. R. Gray, Ph.D. Thesis, University of Strathclyde, UK (2013).
40. P. Norreys *et al.*, Phys. Rev. Lett. **76**, 1832 (1996).
41. B. Dromey *et al.*, Phys. Rev. Lett. **99**, 085001 (2007).
42. B. Dromey *et al.*, Nature Phys. **2**, 456 (2006). B. Dromey *et al.*, Nature Phys. **5**, 146 (2009).
43. C. Thaury and F. Quere, J. Phys. B: At. Mol. Opt. Phys. **43**, 213001 (2010).
44. S. Gordienko *et al.*, Phys. Rev. Lett. **93**, 115002 (2004).
45. S. Gordienko *et al.*, Phys. Rev. Lett. **94**, 103903 (2004).
46. K. Hagiwara *et al.*, Phys. Rev. D **66**, 010001 (2002).
47. S. Segre, *Nuclei and Particles*, 2nd edition, WA Benjamin, RA, London (1977); ELI-NP White Book <http://www.eli-np.ro/documents/ELI-NP-WhiteBook.pdf>.
48. S. Ichimaru, *Basic Principles of Plasma Physics: A Statistical Approach*, Benjamin, Reading, (1973).
49. A. Pukhov and J. Meyer-ter-Vehn, Appl. Phys. B **74**, 355 (2002).
50. H.-C. Wu *et al.*, arXiv 0909.1530v1 (2002).
51. P. Goldreich, and W.H. Julian, ApJ. **157**, 869 (1969) ; A.N. Timokhin, MNRAS, **408**, 2092 (2010).
52. F. Sauter, Z. Phys. **69**, 742 (1931); W. Heisenberg and H.Euler, Z. Phys. **98**, 714 (1936); J. Schwinger, Phys. Rev. **82**, 664 (1951).

53. D.L. Burke *et al.*, Phys. Rev. Lett. **79**, 1626 (1997).
54. K. TaPhouc *et al.*, Nature Photon. **6**, 308 (2012); N. Powers *et al.*, Nature Photon. **8**, 28 (2014).
55. G. Sarri *et al.*, Phys. Rev. Lett. **113**, 224801 (2014).
56. C.D. Murphy *et al.*, in preparation for Phys. Plasmas.
57. A. Ilderton and G. Torgrimsson, Phys. Lett. B **725**, 481 (2013).
58. Tong-Pu Yu *et al.*, Phys. Rev. Lett. **110**, 045001 (2013).
59. T.G. Blackburn *et al.*, Phys. Rev. Lett. **112**, 015001 (2014).
60. T. Erber, Rev. Mod. Phys. **38**, 626 (1966).
61. G. Sarri *et al.*, Phys. Rev. Lett. **110**, 255002 (2013).
62. H. A. Lorentz, *The Theory of Electrons and its Applications to the Phenomena of Light and Radiant Heat*, Stechert, New York (1916).
63. M. Abraham, *The Classical Theory of Electricity and Magnetism*, Blackie, London (1932).
64. A. Burton and A. Noble, Contemp. Phys. **55**, 110 (2014).
65. S.R. Yoffe *et al.*, New J. Phys. **17**, 053025 (2015).
66. N. Neitz and A. Di Piazza, Phys. Rev. Lett. **111**, 054802 (2013).
67. N. Harvey *et al.*, Phys. Rev. Lett. **109**, 100402 (2012).
68. S. Cipiccia *et al.*, Nature Phys. **7**, 867 (2011).
69. S. Corde *et al.*, Rev. Mod. Phys. **85**, 1 (2013).
70. W.P. Leemans *et al.*, Phys. Rev. Lett. **113**, 245002 (2014).
71. M. Abraham, *Theorie der Elektrizität*, Teubner, Leipzig, 1905, Vol. II; H. A. Lorentz, *The Theory of Electrons*, Teubner, Leipzig, 1909; P. A. M. Dirac, Proc. R. Soc. A **167**, 148 (1938).
72. D. Corvan *et al.*, Rev. Sci. Instr. **85**, 065119 (2014).
73. D.J. Corvan *et al.*, ArXiv. 14094243 (2014).
74. D.G. Green and C.N. Harvey, Phys. Rev. Lett. **112**, 164801 (2014).
75. W. Schumaker *et al.*, Phys. Plasmas **21**, 056704 (2014).
76. V.I. Ritus, J. Sov. Laser Res. **6**, 497 (1985), 561, Eqs. (60).
77. H. Euler and B. Kockel, Naturwiss. **23**, 246 (1935), J. S. Toll, Ph.D. thesis, Princeton Univ., 1952 (unpublished), R. Baier and P. Breitenlohner, Act. Phys. Austriaca **25**, 212 (1967); S. L. Adler, Annals Phys. **67**, 599 (1971).
78. H. Gies *et al.*, New J. Phys. **15**, 083002 (2013); H. Gies, F. Karbstein and R. Shaisultanov, Phys. Rev. D **90**, 033007 (2014).
79. E. Lundstrom *et al.*, Phys. Rev. Lett. **96**, 083602 (2006).
80. V. Yanovsky *et al.*, Opt. Exp. **16**, 2109 (2008).
81. D.F. Gordon *et al.*, J. Comp. Phys. **267**, 50 (2014).
82. D.F. Gordon *et al.*, NRL Memorandum Report **6791-15-9634** (2015).
83. D. Gordon *et al.*, Phys. Rev. Lett. **80**, 2133 (1998); E.L. Clark *et al.*, Phys. Rev. Lett. **85**, 1654 (2000); A. Pukhov and J. Meyer-ter-Vehn, Appl. Phys. B **74**, 355 (2002); W. Lu *et al.*, Phys. Plasmas **13**, 056709; S.P.D. Mangles *et al.*, Nature **431**, 535 (2004); B. Dromey *et al.*, Nature Phys. **2**, 456 (2006); D.F. Gordon *et al.*, Phys. Rev. Lett. **101**, 045004 (2008); M.H. Helle *et al.*, Phys. Rev. Lett. **105**, 105001 (2010).
84. W.P. Leemans *et al.*, Nature Phys. **2**, 696 (2006).
85. B.M. Hegelich *et al.*, Nucl. Fusion **51**, 083011 (2011).
86. Javanainen *et al.*, Phys. Rev. A **38**, 3430 (1988).
87. P. Corkum *et al.*, Phys. Rev. Lett. **62**, 1259(1989).
88. C.I. Moore *et al.*, Phys. Rev. Lett. **82**, 1688 (1999).
89. A. Ting *et al.*, Phys. Plasmas **12**, 010701 (2005).
90. R.F. Hubbard *et al.*, Phys. Plasmas **9**, 1431 (2002).
91. Y. Katzir *et al.*, Appl. Phys. Lett. **95**, 031101 (2009).
92. Y. Katzir *et al.*, Opt. Express **21**, 5077 (2013).
93. H. Milchberg *et al.*, Phys. Plasmas **3**, 2149 (1996).
94. B. Hafizi *et al.*, Phys. Plasmas **10**, 1483 (2003).
95. D.F. Gordon and B. Hafizi, NRL Memorandum Report 6790-12-9398 (2012).

96. D. Ursescu *et al.*, Rom. Rep. Phys. **68**, S11 (2016).
97. F. Negoita *et al.*, Rom. Rep. Phys. **68**, S37 (2016).
98. T. Asavei *et al.*, Rom. Rep. Phys. **68**, S275 (2016).
99. P. L. Poole *et al.*, Phys. Plasmas **21**, 063109 (2014).
100. M. O. Cernaianu *et al.*, Rom. Rep. Phys. **68**, S349 (2016).
101. Cork and M. Smith, Nuclear Technology Report, *ELI-NP- 01-C03-II*, Issue I1, Addendum 3: *Bulk shielding analysis for E6 sources* (2014).
102. L. C. MacFarlane, S. Wilson, Nuclear Technology Report *ELI-NP- 01-C07-II*, *E6 Source C Dose Rate Contours* (2014).
103. I.-O. Mitu *et al.*, Rom. Rep. Phys. **68**, S885 (2016).